



Politecnico di Milano

Department of Chemistry, Materials and Chemical  
Engineering  
"Giulio Natta"

PhD thesis in Materials Engineering, Cycle XXVII°

---

# Polymeric Materials for Advanced Human Health Applications

Author:

**Caterina Credi**

Supervisor:

**Prof. Stefano Turri**

Tutor:

**Prof.ssa Marinella Levi**



>>

**Abstract**

The research work of this thesis can be divided in two main parts both related to the development and functionalization of polymeric materials for advanced human health applications. One deals with stem cells based therapies for tissue engineering applications whereas the other deals with the development of patterned functional biomaterial surfaces for rare cells capture and isolation. The goal of tissue engineering is to replace or to repair a damaged tissue or organ with artificial tissue made by seeding living autologous “organ specific” cells on a biomaterial acting as an extra-cellular matrix (ECM) and culturing them giving proper cues until maturation in a functional tissue ready to be transplanted. One promising strategy consists in addressing stem cells fate by fine-regulating their interaction within artificial microenvironments, “synthetic niches” engineered to mimic individual biochemical (e.g. delivery of soluble factors) and biophysical factors (e.g. substrate stiffness). To this end, the first part/objective of this PhD project aimed to independently investigate the specific role that niches physic-mechanical properties, in terms of scaffold geometry and surface stiffness, have on SCs response and to study the possibility to fine tune cell/material interactions. 3D freestanding niches with suitable geometry/features were fabricated by two-photon polymerization (2PP). Different immobilization strategy were explored to further functionalized 2PP niches with thin layers of biomimetic hyaluronan- and gelatin-based hydrogels, which were developed to have tailored stiffness encompassing the range of physiological values. Hydrogels mechanical properties were evaluated validating a reliable methodology based on three independent experimental techniques. Rheological results obtained on macroscopic samples were successively benchmarked with swelling experiments following Flory-Rehner theory and by Atomic Force Microscopy (AFM) nanoindentation, more suitable techniques for the characterization of small-scale hydrogel samples as those grafted onto niches. Finally, biological validation tests assessed the biocompatibility of all the coatings with enhanced cell proliferation with respect to uncoated niches. However, commitment towards the osteochondral lineage together with a stronger metabolic activity was observed just for gelatin-coated niches compared to hyaluronan-coated ones.

The second objective of the research was the design and realization of target baits arrays for physically isolate rare cells from a heterogeneous population. The main advantage is the selective analysis of individual cellular processes instead of analyzing the behavior of a whole cell population, as for conventional cell-based assays. A fundamental issue was the selection of the substrate material that deeply affects the final performance of the array. Best performing materials should avoid non-specific cells binding, thus perfluoropolyethers (PFPEs) were considered due to their wide range of properties including very low surface tension, which enhances PFPEs anti-fouling/fouling release properties. Different photocurable PFPEs were compared and deeply characterized in terms of crosslinking kinetics, surface properties, transition temperatures and anti-fouling/fouling release characteristics to understand the relationship between structure and properties. A blend consisting of two PFPE-dimethacrylates (PFPE-DMAs, 1:1) with different molecular weights was selected as the most valuable candidate for the discussed application. Derivatives of hyaluronic acid (HA) and heparin were immobilized as target baits for capture cancer cells and malaria-infected red blood cells respectively. To this end, photo-lithography and soft-lithography were developed and optimized as technologies to selectively functionalize PFPEs surfaces following different strategies/chemistries. Particularly, free radical polymerization was exploited for glycidyl methacrylate modified HA grafting onto partially cross-linked PFPE surfaces by photo-lithography. Finally, biomolecular recognition and strong specificity between avidin and other biotin-binding proteins was used for biotinylated-derivatives. A photo-activable biotin was preprinted by  $\mu$ -contact printing and UV-grafted onto partially cured PFPE substrate, then the two derivatives were immobilized using avidin as intermediate linker. Cellular tests were performed with cancer cells and malaria-infected red blood cells to assess the capability of patterned PFPEs surfaces in capturing individual population cells.



>>

## **Table of contents**

<b>1. Regenerative medicine</b>	<b>1</b>
1.1 General introduction	2
1.2 Stem-cells based therapies	5
1.3 Materials for 3D niches engineering	10
1.4 References	20
<b>2. Biomolecular patterning technologies for living-cells arrays</b>	<b>27</b>
2.1 General introduction	28
2.2 Patterning technologies	38
2.3 Anti-fouling/fouling-release properties	44
2.4 References	47
<b>3. Aim of the work</b>	<b>55</b>
<b>4. Hydrogels synthesis and fine tuning of mechanical properties</b>	<b>59</b>
4.1 Introduction	60
4.2 Experimental section	63
4.2.1 Materials	63
4.2.2 Hydrogels synthesis and functionalization	63
4.2.3 Physical characterization	66
4.3 Results and discussion	73
4.3.1 Hydrogels chemical and photochemical cross-linking	73
4.3.2 HA:DVS biocompatibility	75
4.3.3 Hydrogel characterization	76
4.4 Conclusions	85
4.5 References	87

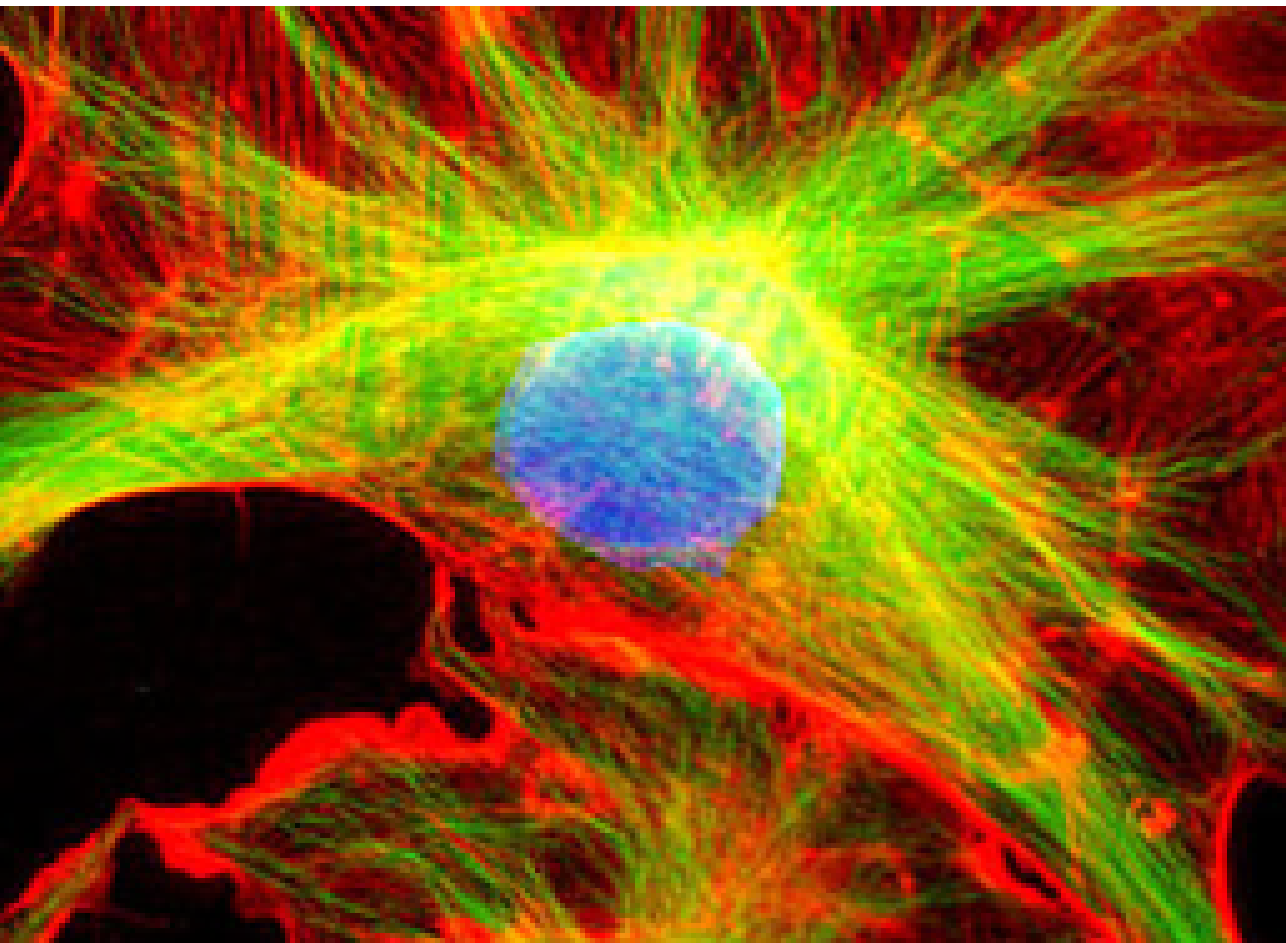
<b>5. Mimicking stem-cell niches through hydrogel functionalization of 2PP scaffolds</b>	<b>91</b>
5.1 Introduction	92
5.2 Experimental section	94
5.2.1 2PP scaffold fabrication	94
5.2.2 Design of hydrogels coating	97
5.2.3 Microfluidic channel fabrication	101
5.2.4 Scaffold surfaces functionalization	104
5.2.5 Hydrogels coating characterization	107
5.2.6 Cellular tests	111
5.3 Results and discussion	116
5.3.1 2PP Scaffold fabrication	116
5.3.2 Hydrogel coating	118
5.3.3 Cellular tests	125
5.4 Conclusions and future perspectives	140
5.5 References	142
<b>6. Protein antifouling and fouling-release in perfluoropolyether surfaces</b>	<b>147</b>
6.1 Introduction	148
6.2 Experimental section	150
6.2.1 Perfluoropolyether materials	150
6.2.2 Fourier Transform Infrared spectroscopy (FTIR) analysis	151
6.2.3 Surface characterization	152
6.2.4 Dynamic mechanical analysis	153
6.2.5 Anti-fouling and fouling release properties evaluation	153

6.3	Results and discussion	159
6.3.1	Photocurable PFPEs	159
6.3.2	Surface characterization: contact angle	161
6.3.3	Dynamic mechanical analysis	164
6.3.4	Anti-fouling and fouling-release properties	165
6.3.5	The role of surface and mechanical properties on fouling release properties	172
6.4	Conclusions and future perspectives	174
6.5	References	175
<b>7.</b>	<b>Photo-lithographic and soft-lithographic technologies for biomolecular patterning onto anti-fouling surfaces</b>	<b>179</b>
7.1	Introduction	180
7.2	Preliminary results	182
7.3	Experimental section	185
7.3.1	Perfluoropolyether materials	185
7.3.2	Photopolymerization kinetics	185
7.3.3	Polymer characterization	186
7.3.4	Surface characterization of Blend films	187
7.3.5	Biomolecular patterning	187
7.3.6	Cellular validation tests	193
7.4	Results and discussion	197
7.4.1	Perfluoropolyether materials	197
7.4.2	Photopolymerization kinetics	197
7.4.3	Polymer characterization	199
7.4.4	Surface characterization of Blend films	200
7.4.5	Biomolecular patterning	202

7.4.6 Cellular tests	208
7.5 Conclusions and future perspectives	214
7.6 References	216
<b>8. Conclusions</b>	<b>219</b>
<b>Appendix 1 – Glossary</b>	<b>223</b>
<b>Appendix 2</b>	<b>227</b>



# 1. Regenerative medicine



## 1.1 General introduction

In the last decades the field of regenerative medicine has developed different strategies trying to satisfy the need for organs and tissues deriving from injuries, lesions or ageing which represent one of the most costly problems of human health care. It is estimated that almost one third of the tissue graft procedures performed worldwide involves bone cartilage and osteo-chondral tissue. The current gold standard for osteo-chondral tissue graft is autologous graft, or autograft, where tissue functionality is restored using biological material from a healthy site to the diseased site in the injured patients. However, this is responsible for donor-site irreversible damage together with longer patient's hospital stay. Moreover there could be limited supply of tissue to be transplanted. As alternative, lots of patients choose the transplant of an organ or tissue from one individual of the same species known as allogenic graft or allograft. There is no a second surgical site to be healed, but the real risk for disease transmission and immune rejection make it necessary of life-long immunosuppression therapies. Moreover, there is an ever-growing supply and demand mismatch of organs and tissues and the number of patients registered on deceased donor transplants waiting lists. This because transplantation is restricted by the donor shortage, as data report fewer than 11,000 donors (cadaveric and living) available annually for more than 70,000 patients awaiting organ transplantation<sup>1-3</sup>. Donor shortages increase every year, and many patients die while waiting for needed organs. The mismatch could be filled exploiting animals as donor graft, as in the case of xenograft, or exploiting artificial organs such as joint prosthesis or dialysis machine. However, immunologic hurdles limit xenograft organs<sup>4,5</sup>, which are derived from porcine sources, whereas artificial organs and mechanical devices cannot perform all of the functions of a single organ and therefore provide only temporary benefit. Major complications using non-biological materials include infection, lack of biocompatibility and limited material durability. In this scenario, a significant worldwide effort involving new strategies and research area is being currently directed towards the growth in

vitro of replacement autologous tissue readily available for transplantation in regenerative medicine.

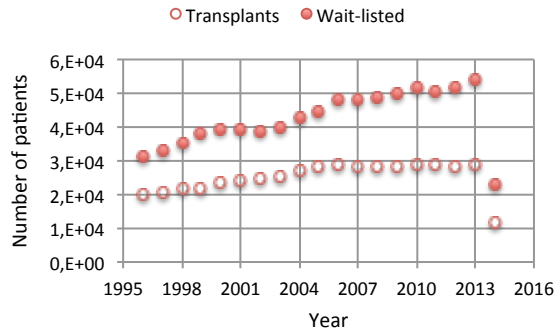


Figure 1. UNOS organ transplant statistics for January 1995 to May 2014 documenting the wait-listed patients and transplants.

As a matter of fact, 4 billions of euro have been invested worldwide in research and development pertaining the interdisciplinary field of tissue engineering, an area of scientific and technological progress applying the principles and methods of engineering and life science<sup>6</sup> to revolutionize methods of treatment and to increase the pool of available tissues and organs for transplantation thus drastically improving the quality of life of millions of patients throughout the world.

The goal of tissue engineering is to fabricate living replacement part of the body with an artificial organ or tissue, made by seeding living autologous “organ specific” cells on a scaffold, a biocompatible synthetic or natural degradable three-dimensional matrix. These scaffolds are porous structures where cells are seeded and spatially arranged into a three-dimensional architecture.

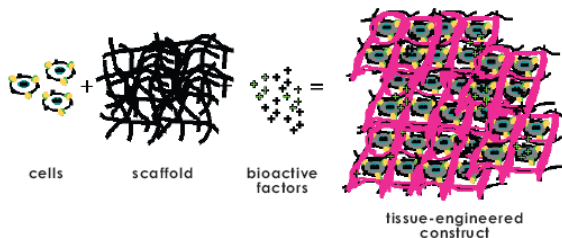


Figure 2. Graphic illustration of scaffold-based tissue engineering. Living cells are seeded onto a 3D synthetic matrix which is engineered to present specific physicochemical properties.

In tissue engineering, these 3D-structures initially perform the function of the

extracellular matrix (ECM) and hence are engineered to provide a bioactive microenvironment that guides tissue development and that promote stem cells differentiation into mature cells tissue through their physicochemical properties. The scaffold should provide temporary structural support, followed by possible degradation, during the deposition of ECM by cells. Finally, cells are arranged in vitro into a three-dimensional architecture and the construct is cultured until maturation into a functional tissue, designed and fabricated to meet the individual defects, and ready to be transplanted into the patient. These laboratory-engineered tissues, as an alternative to autologous transplant, allograft, xenograft and prosthesis, will provide a perspective of transplant of functional tissue without risk of immune rejection as the biological material transplanted is of autologous origin.

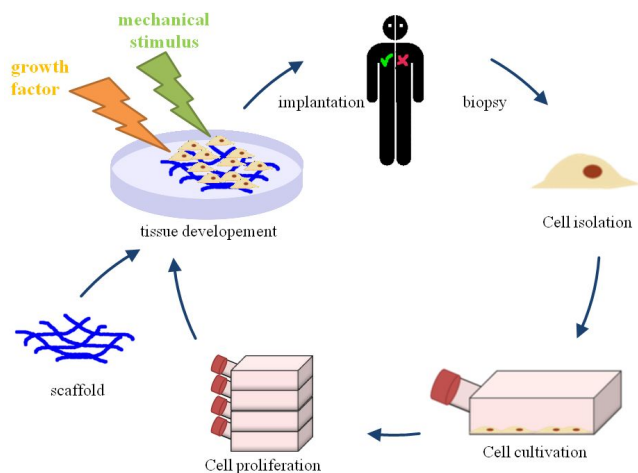


Figure 3. Basic principle of Tissue Engineering. Autologous cells from biopsy are expanded in vitro in 2D culture and subsequently seeded onto an engineered scaffold proper stimuli. The construct is cultured until maturation into a functional tissue ready to be transplanted into the patient.

## 1.2 Stem cells-based therapies

### 1.2.1 Cell source

Stem cells are of great interest as autologous source for cell therapies and tissue engineering applications<sup>7</sup> due to their dual ability to self-renew reproducing themselves leading to at least one daughter cell equivalent to the mother (self-renewal), and to differentiate into variety of different lineages, thus ensuring support and regeneration of tissues. Depending on the site they are isolated from, SCs may be embryonic (ESCs), fetal (FSCs), and adult<sup>8,9</sup>. ESCs are generally isolated from the inner cell masses of blastocysts, which consist of pluripotent cell populations and are able to generate one of the three germ layers, endoderm, ectoderm and mesoderm, thus potentially providing the biomedical community with a continuous source of all cell types<sup>10,11</sup>. However, several studies revealed the effort requested when working with large number of ESCs and particularly when developing a reliable methodology to direct them to differentiate into specific cell types<sup>12</sup>. Moreover, if ESCs are injected in vivo when still undifferentiated, they might give rise to teratocarcinoma, a type of tumor composed of cells derived from the three germ-like structures<sup>13,14</sup>.

To avoid tumor formation in vivo, multipotent fetal stem cells (FSCs) derived from the umbilical cord blood, could be exploited. They still have high plasticity but are generally less pluripotent than ESCs giving rise to a limited number of progenitor types<sup>15-17</sup>. Finally, recent studies revealed that most adult tissues<sup>18-22</sup> localized adult stem cells, which are still multipotent but their differentiation potential is restricted to the tissues they are derived from<sup>8,9</sup>. While ESCs are essential during the embryological development for the generation of diverse tissues, adult SCs play an active role throughout life for tissue homeostasis by replenishing the cells that repopulate the tissues/organs and regenerating damaged tissues during injuries<sup>23</sup>. SCs can retain this unique function only when residing within specific anatomic locations, known as stem cells niches, which have a deep impact on balancing SCs functions and addressing their fate<sup>24,25</sup>. SCs

niches are composed by supporting cells, three dimensional extra-cellular matrix (ECM) and cascades of molecular and physical signals such as hormones, growth factors cytokines and secreted proteins from neighboring cells and tissues. Thus, three different types of interactions could be identified within a niche: cell-cell, cell-ECM and cell-biochemical factors. Cell-cell interactions occur between SCs and supporting cells through adhesive cadherin protein junctions<sup>26</sup>. These adhesive interactions help anchoring the SCs to their niche and localizing their position in close proximity to self-renewal signals. Adhesion proteins, such as integrins, are involved even in the intimate contact between the SCs and the ECM<sup>27,28</sup>, a protein- and sugar-rich cross-linked network mainly composed of structural (i.e. collagen, fibronectin and laminin) and specialized (small matricellular proteins, growth factors) proteins as well as glycosaminoglycans and proteoglycans. In response to protein chemical signals and biochemical factors transmitted by ECM, SCs constantly reshape and remodel the ECM by degrading and reassembling it. This remodeling phenomenon has a dual purpose: maintaining the tissue homeostasis, and repairing the tissue in response to infectious agents and in case of injury or loss of tissue<sup>29</sup>. Finally, the interplay of this complex ensemble of interactions is the main force driving the SCs behavior and understanding the role of each chemical, mechanical and physical cue is the starting point for manipulating SCs and tackling their differentiation for in vitro and clinical applications.

For instance, successful formulation of regenerative medicine strategies would have a great impact in the field of osteo-chondral/bone tissue engineering, constituting about one third of the tissue graft procedures performed worldwide. Bone-forming cells (osteoblasts) could not be employed as autologous cell source because of their inability to proliferate *in vitro*. Therefore alternative autologous sources are needed and adult bone marrow-derived mesenchymal stem cells (MSCs) are the cell source deeply investigated for the regeneration of musculo-skeletal tissue. MSCs are multipotent progenitor cells noted for their potential to differentiate into a variety of anchorage-dependent cell types, including skeletal connective tissues osteoblasts, chondrocytes, bone marrow adipocytes and

hematopoiesis- supportive stromal cells<sup>30,31</sup>.

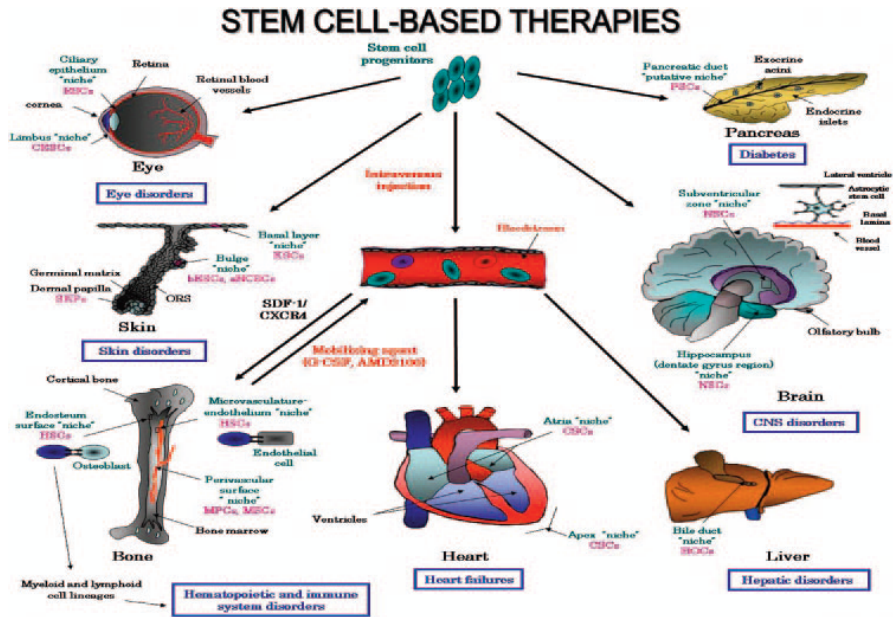


Figure 4. Scheme showing the tissues/organs constituting the potent targets for tissue regeneration by stem cell-based therapies.

### 1.2.2 3D niches/ECM engineering

To date, existing knowledge on SCs behavior derives from two-dimensional (2D) cell-cultures performed on flat surfaces. Moreover, traditional therapies mostly involve SCs manipulation and control of differentiation employing cocktails of various growth factors<sup>8,32</sup>. Although 2D platforms enable a simplified approach to deconstructing the niche and identifying and assessing the effects of individual niche components on SCs fate, these culture conditions are really far from the 3D physiological conditions experienced by the majority of the cells in the body<sup>24,33</sup>. Many researchers have demonstrated that the properties of the cells and of their ECM in a 2D culture differ substantially from those of cells grown in a 3D microenvironment<sup>34</sup>, thus inspiring the recent transition from 2D to 3D cell-culture techniques aiming to recapitulate *in vivo* biology. In tissue engineering

the function of the ECM is initially performed by the scaffold that should provide temporary structural support, followed by possible degradation, during the deposition of ECM by cells<sup>35</sup>. Moreover, the scaffolds should be designed to incorporate the physiological cues of the SCs niches in order to direct and enhance cell function and differentiation through proper interactions<sup>10,36</sup>.

There is an increasing awareness of the importance of the biophysical and mechanical properties of the synthetic microenvironments that cells “sense”, especially for anchorage-dependent cells whose adhesive integrins bind to specific motifs within ECM proteins thus triggering intracellular signaling pathways involved in determining cell fate<sup>30</sup>.

First, the biophysical characteristics of the scaffold should be considered in terms of architectural properties and spatial arrangement. Because 3D *in vitro* models are not connected to the blood stream, scaffolds with suitable microgeometries and with interconnected porosity of appropriate scale are necessary for cellular migration within the construct and for their oxygenation, nutrition and waste removal by diffusion. Generally, matrix porosity should range in the scale of cellular processes (100  $\mu\text{m}$   $\div$  50  $\mu\text{m}$ ). Pores exceeding these sizes would lead cells to feel mechano-transduction mechanisms similar to those of planar substrates due to the fact that cells will present a flat morphology by attaching only its basal surface to the material<sup>37-40</sup>. On the other hand, varying within this range, microporosity affect cell cytoskeletal organization thus cell adhesion morphology that vary from a highly tensed, spread cell when in higher pores to a low-tension, more rounded cell that contacts the material in all dimensions. These alterations in the cell configuration might promote or inhibit changes in the nuclear morphology, nuclear physical and mechanical properties, DNA packing and gene activation<sup>41,42</sup> and hence, it might affect differentiation<sup>43</sup>.

The mechano-transduction signaling deriving from integrin engagement to the ECM and cytoskeleton contractions is related not only to the microgeometry of the matrix but also to its surface mechanical properties in terms of surface elasticity<sup>31,44,45</sup>. In fact, the resistance that a cell feels when adhering and deforming the ECM is transduced into morphological changes and lineage

specification as revealed by 2D-platform studies where cells showed a preference to grow on substrate with mechanical properties approximating those of their natural SCs niches<sup>46-48</sup>. It was reported that MSCs address to neurogenic lineage when cultured on soft brain-like substrates (<1 kPa), to myogenic lineage when cultured on stiffer muscle-like substrates (8 ÷ 15 kPa), and to osteogenic lineage when cultured on relatively higher modulus substrates (25 ÷ 40 kPa)<sup>46</sup>.

### 1.3 Materials for 3D niches engineering

The first step towards successful SCs-based therapies relies not only upon cell source type but also upon the parallel advances in developing biomaterials suitable to design synthetic niches mimicking individual aspects<sup>44,49</sup>.

Adequate scaffold material selection depends on several variables related to the specific applications, but generally an ideal material should:

- Be biocompatible, biodegradable or bioresorbable with non-citotoxic degradation products;
- Possess appropriate mechanical properties to match the intended site of implantation and handling;
- Be mechanically stable to guarantee structural support to cell till they have built their own matrix;
- Allow facile surface and bulk functionalization to induce specific cell signal transduction;
- Be easily processable exploiting scaffold fabrication technologies necessary to fabricate suitable shapes and sizes;
- Allow to independently varying all the parameters enabling to disentangle the role of each property on SCs behavior.

Biomimetic scaffolding materials have been developed starting from both natural and synthetic materials and tailoring their properties through physical or chemical modifications.

Natural biomaterials include those derived from the main components of the ECM (e.g. collagen, hyaluronic acid, glycosaminoglycans (GAGs), fibrinogen) and those derived from plants, insects or animal components (e.g. cellulose, chitosan, silk fibroin). They have the advantages of being bioactive, biocompatible and show biomimetic properties similar to the tissues they are derived from. Nowadays, even if several natural materials are commercially available, well characterized with reproducible, controlled properties (Matrigel<sup>TM50</sup>, Hyaff<sup>51</sup>), they still have limitations including low control over physico-chemical properties and difficult to modify their degradation rate. Moreover, difficulties in

sterilization and purification may limit their clinical application due to the risk of immunogenicity and disease transfer.

Synthetic materials, mainly comprising polymers, enable easier modulation of both the structural and mechanical properties of the scaffolds. They could be processed by several standard methods (e.g., solvent casting, sintering, particulate leaching and electrospinning). However, recent studies revealed the possibility to process polymers by microfabrication technologies like 3D laser non linear lithography<sup>52,53</sup>, thus enabling to fine control pore geometry, size and interconnectivity of the final construct, avoiding random pore distributions typical of standard methods. On the other hand, the mechanical properties and the degradation rate of the 3D synthetic scaffolds can be tailored by controlling the concentrations and molecular weight of the polymer, or the type or density of cross-linking between the polymer chains. In general, the disadvantages for choosing such materials include poor inherent bioactivity (e.g. Poly(ethylene glycol) (PEG)), acidic by products (e.g. Polyglycolic acid (PGA) or Polylactic acid (PLA)). Thus, chemical modifications of their surfaces with biological or chemical entities are required to achieve appropriate cellular response.

Come to evidence that it is hard to satisfy simultaneously the various demands with single-component scaffolds. Therefore recent studies suggest using combinations of several types of materials for different purposes; for example fabricating a base scaffold providing 3D microenvironment whose inner pore surfaces could be coated by different material to tailor cell-surface interactions<sup>54-56</sup>.

### 1.3.1 Photosensitive polymeric material for two-photon polymerization (2PP) technology

Micron-sized topography and porosity of the synthetic niches have been shown to play an essential role in affecting cellular functions. Most traditional scaffolds do not offer truly 3D culture for a dual reason. First, standard fabrication processes such as gas foaming, solvent casting, and electrospinning, produce structures with random pore distribution that do not allow to have a

reproducible and controlled method of micro- nanostructuring. Secondly, size pores usually vary in the order of 100  $\mu\text{m}$  in diameter, almost tenfold the physiological size of cells that consequently behave as they were adhering on a 2D surface as revealed by their flat morphology. In order to overcome these problems and downsizing features of synthetic niches, a class of manufacturing technologies known as solid free-form fabrication (SFF) or rapid prototyping have been successfully used to fabricate tailored complex structures directly from computer data via computer aided design/computer aided manufacturing (CAD/CAM)<sup>57-59</sup>. process wherein an electron first transits from a low energy level to a higher energy level by the simultaneous absorption of two photons.

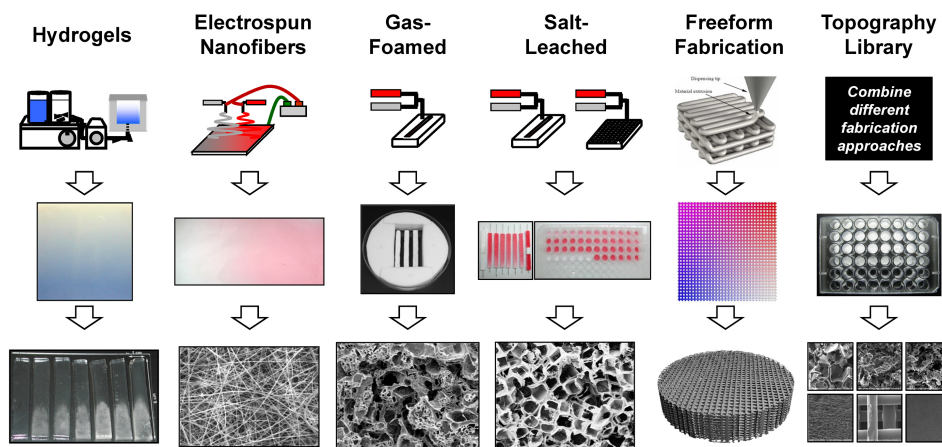


Figure 5. Scheme illustrating various technologies that have been developed for 3D synthetic matrix fabrication. SEM images highlight the differences in size pores distribution obtained. Just exploiting freeform fabrication is possible to create 3D matrices with controlled geometries<sup>60</sup>. <http://www.nist.gov/mml/bbd/biomaterials/3dtissuescaffolds.cfm>

Some of these technologies have already been implemented and commercialized and include stereolithography, selective laser sintering, fused deposition modeling and inkjet fabrication<sup>61,62</sup>. However, their low resolution doesn't enable to obtain structures with biophysical characteristics mimicking those of native cell environment. Nowadays, the most advanced technology for fabricating ultra-precise structures controlled at the cell-scale is femtosecond laser two-photon polymerization (2PP)<sup>63,64</sup>. 2PP is a rapid, single-step versatile technology allowing the fabrication of polymeric 3D structures of arbitrary architecture with

sub-micrometer spatial resolution ( $<100$  nm).

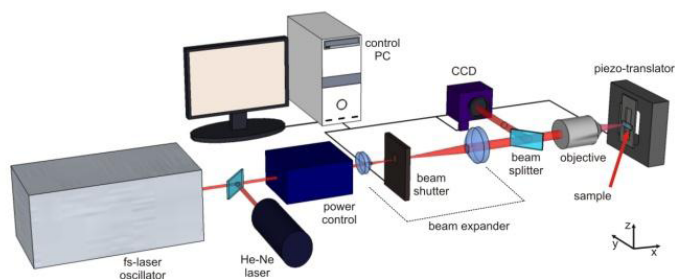


Figure 6. Scheme of the 2PP fabrication set-up. The femtosecond laser source generally consists of a Ti:Sapphire oscillator but also Yb-based laser are suitable for 2PP polymerization. The writing beam is directed through a power control setup consisting of a half waveplate followed by a linear polarizer. The beam then passes through an optional second harmonic crystal for frequency doubling. A beam expander telescope may be used to fill the entire clear aperture of the microscope objective for best possible focusing. The beam is then focused inside the photoresist using a lens or microscope objective and the sample is translated relative to the beam using three-axis computer-controlled translation stages.

During 2PP, 3D scaffold are directly laser-written tightly focusing the beam of an ultrafast infrared laser into the volume of a photosensitive material (photoresist). The latter usually include a prepolymer (monomer) resin containing a photoinitiator. Within the focal region, focused ultra-short laser pulses absorption occurs by means of multiple photons absorption phenomenon as two-photon absorption (TPA) and the photoinitiator is excited. TPA is a non-linear photochemical. Briefly, an electron transits to a virtual intermediate stage by the absorption of the first photon; if the absorption of the second photon occur during the lifetime of within  $10^{-4} \div 10^{-9}$  s, the electrons populating the intermediate stage complete their transition and transit to the higher level. Finally, the tight focusing and the non-linear interaction of femtosecond pulses with the photoresist, confine TPA to the focal volume without causing absorption at the surface, enabling the 3D patterning advantage of 2PP<sup>65</sup>. General criteria for choosing a photopolymer suitable for 2PP scaffold fabrication include thermal and mechanical stability of the cross-linked structure, time required for processing, biocompatibility and biofunctionality, and ease of tuning mechanical properties through changes of chemical composition or coating. If the cellular construct is designed to degrade immediately after implantation in vivo,

biodegradability is also required. For the latter, biopolymers including bovine serum albumin (BSA), ECM-derivatives and polymer-protein hybrids based on caprolactone and on polylactic acid have been implemented<sup>61,66,67</sup>. However, these materials often lack the necessary mechanical stability. On the other hand, the non-biodegradable commercially available materials include different types of vinyls<sup>68</sup>, epoxies<sup>69</sup>, acrylates<sup>70</sup>, and hybrid inorganic-organic materials<sup>71</sup>. Acrylate-based resins are characterized by higher speed processability with respect to other materials. Since free-radical polymerization is exploited to induce their chemical reactions, acrylates also show higher TPA efficiency<sup>72</sup>. Conversely, cationic polymerization occurs for the photopolymerization of epoxies as for SU-8 resin, which is already widely used in conventional photolithography processes but requires several processing step prior to UV-exposure. Finally, photosensitive organic-inorganic materials have gained particular attention since they have been demonstrated to be easily photo-structurable and have shown sufficient biocompatibility based on comparison of cell growth rates with standard substrates. In particular, organically modified silicates, referred to as ORMOSILs or ORMOCERs, have been synthesized by sol-gel processing<sup>71</sup>. Starting from a liquid precursors 3D networks are formed during irradiation via the crosslinking of inorganic and organic moieties thus ORMOCERs combine the properties of organic polymers (low-temperature processing and functionality) with those of inorganic glasses (hardness, thermal and chemical stability, and optical transparency). The ratio between the organic and inorganic moieties is the key parameter that allows tuning mechanical, optical, chemical and surface properties of the final polymer. One limitation of ORMOCERs is that as the liquid turns into a solid during 2PP, a severe shrinkage occurs, resulting in a final structure that deviates from the intended design. However, in recent years several studies reported the 2PP fabrication of scaffolds exploiting a new promising hybrid organic-inorganic class of photoresists, which are mainly composed of a silicon alkoxide and zirconium alkoxide and whose molar ratio has been optimized to increase their photosensitivity and avoid structural deformation caused by shrinkage phenomena<sup>71,73,74</sup>.

### 1.3.2 Hydrogels as materials for surface niche engineering

The surface properties of tissue engineering scaffolds play a key role in manipulating stem cells behavior. The interactions of cells with the artificial substrates trigger transmembrane signals that are the driving forces to many essential cellular functions. Particularly, the mechanical properties in terms of substrates stiffness influence the forces exerted by cells on their substrates affecting their adhesion morphology and hence, their fate. In fact, alterations in the cytoskeletal organization might affect nuclear morphology and consequently DNA packing and gene activation. Finally, tailoring surface and bulk properties of scaffolds is important in modulating the cellular response to the scaffolds.

Due to their high water content, biocompatibility and mechanical properties that resemble many biological tissues, hydrogels represent an attractive class of biomimetic materials for tissue engineering applications such as space filling agents, delivery vehicles for bioactive molecules, and biomimetic scaffolds<sup>75,76</sup>. Depending on the specific applications, hydrogels should meet different requirements in terms of physical properties, mass transport properties, and biological properties. Currently, hydrogels scaffolds have been exploited to engineer a wide range of tissues, including cartilage, bone, muscle, fat, liver, and neurons. They are structurally similar to the natural ECM with a three-dimensional networks made of cross-linked hydrophilic polymer chains that are able to retain a large amount of water but are prevented from dissolving due to their chemically or physically cross-links. The high equilibrium swelling promotes nutrient diffusion and cellular waste removal, while their insolubility provides the structural integrity necessary for tissue growth.

Their swollen behavior could be described by combining thermodynamic equilibrium-swelling theory and elasticity theory. In fact, as Flory first described<sup>77</sup>, when a cross-linked polymer gel is immersed in a proper solvent, an equilibrium swelling value is reached as a compromise between two opposing forces: the thermodynamic force of mixing of the fluid molecules with the polymer chains and the retractive force that the polymer chains exert through the cross-linked network. Thus, the structural integrity of the hydrogels is maintained by crosslinks formed between polymer chains and modifying the degree of cross-linking deeply affects the degree of swelling, which is strictly correlated to the hydrogels mechanical strength. Hydrogels usually show poor mechanical properties and rapid degradation, which make them unsuitable for higher stiffness tissue engineering as in the case of connective tissue. To face these problems, improving their mechanical properties and controlling the degradation rate, hydrogels can be chemically modified under mild, biocompatible conditions to provide desired elasticity and biodegradability. Particularly, several studies assess the possibility to tailor the mechanical properties and degradation rate of cross-linked hydrogels by controlling the cross-linking density and molecular weight of the cross-linking molecules, by altering the comonomer composition and by changing the conditions under which the polymer is formed<sup>78-80</sup>. Hydrogels for tissue engineering can be characterized based on their derivation and composition as synthetic, natural and hybrid.

Synthetic hydrogels can be generated using various chemical methods starting from derivatives of poly(hydroxyethyl methacrylate) (PHEMA), poly(ethylene glycol) (PEG), and poly(vinyl alcohol) (PVA). Chemical functionalization and cross-linking of the hydrophilic chains, including photo- and thermal-initiated polymerization, were deeply studied and

optimized to provide 3D microenvironments with controlled and reproducible tunable features. In fact, this polymer networks can be designed and reproducibly synthesized with molecular-scale control over structure, such as cross-linking density and with tailored mechanical properties, such as biodegradation, mechanical strength, and chemical and biological response to stimuli. PEG hydrogels are one of the most widely used materials for biomedical applications and the US Food and Drug Administration (FDA) currently approves it for various clinical uses. Hydrophilic PEG chains can be photocross-linked exploiting acrylate-terminated PEG monomers. Furthermore, they represent a versatile platform for many other subsequent conjugations, thus allowing forming varying covalently cross-linked hydrogels and adding specific properties to the PEG gels. For example, peptide sequences can be incorporated in the PEG gels structure to modify their passive behavior towards most biological molecules, thus their interactions with cells. In fact, the poor inherent bioactivity of synthetic gels, together with possible acidic by-products, represent the main disadvantage for choosing this class of hydrogels. From this combination of biological entities with synthetic hydrogels, a new class of biohybrid hydrogels was created. These novel systems synergistically combine biological mechanism, such as high affinity and specificity of binding, with tailorable hydrogel properties<sup>81</sup>. Growth factors, enzymes, peptides and amino-acid sequences are the mostly used biologically active molecules that could be chemically or physically entrapped into polymer networks to produce conjugated biomaterials.

Hydrogels from natural sources generally are either components of or have macromolecular properties similar to the natural ECM. The formers mainly include mammalian-derived protein-based polymers and

glycosaminoglycans (GAGs), whereas linear polysaccharides such as alginate and chitosan are those structurally similar to the ECM. Collagen is the most abundant protein of the mammalian tissue and the main component of the ECM<sup>82</sup>. It is generally composed of polypeptide chains held together by both hydrogen and covalent bonds, thus forming natural gels, which represent an effective matrix for cellular growth due to the presence of many cell-signaling domains present in the *in vivo* ECM. However, collagen and collagen-derived gels could be synthesized with enhanced mechanical properties by exploiting chemical crosslinking, crosslinking with physical treatments (UV or temperature), or blending with other polymeric agents. Among collagen derivatives, gelatin has been extensively used in tissue engineering not only for its biocompatibility but also for its potentiality to induce stem cells differentiation, which is directly linked to intracellular signaling pathways by cellular integrin receptors<sup>83</sup>. Hyaluronic acid (HA) is the GAG prevalently used for cartilage tissue reconstruction and its great potential is due to the presence of various surface receptors (e.g. CD44), which are involved in cell signaling through sophisticated signaling pathways. This linear polysaccharide is present as a gel-like substance with poor mechanical properties in nearly every mammalian tissue and fluid, especially in the synovial fluid of the joint. However, stiffer HA hydrogels can be formed by covalent cross-linking, as for collagen, through multiple chemical conjugations. Finally, alginate and chitosan have been investigated for a variety of tissue engineering applications, because they are structurally similar to naturally occurring GAGs. They are linear polysaccharides derived from brown seaweed and crustacean shells respectively. Alginate gels are mainly formed upon formation of ionic bridges between different polymer chains, whereas chitosan can be cross-linked by increasing pH,

by dissolving in a nonsolvent or by photocross-linking. Due to the gentle gelling conditions, slow degradation and low toxicity alginate and chitosan gels are widely used for cell encapsulation and drug delivery<sup>8,75,76</sup>.

All natural derived hydrogels are physiologically degraded by cells through the release of specific enzymes and proteins. By manipulating the cross-linking conditions it is possible to partially control their kinetics of degradation to address a specific application.

## 1.4 References

1. Niklason, L. E. & Langer, R. Prospects for organ and tissue replacement. *J. Am. Med. Assoc.* **285**, 573–576 (2001).
2. www.unos.org. No Title. (2012).
3. Health Resources and Health Administrations, U. S. D. of H. & H. S. No Title. <http://optn.transplant.hrsa.gov/latestData/rptData> (2014).
4. Goddard, M. J. Xenotransplantation--2000. *J. Clin. Pathol.* **53**, 44–48 (2000).
5. Hancock, W. W. Xenotransplantation is this the future? *Semin. Nephrol.* **20**, 217–229 (2000).
6. Lalan Sonal, B. A., Pomerantseva Irina, M. D. & Vacanti Joseph P., M. D. Tissue Engineering and Its Potential Impact on Surgery. *World J. Surg.* **25**, 1458–1466 (2001).
7. Bianco, P., Robey, P. G. & Simmons, P. J. Mesenchymal stem cells: revisiting history, concepts, and assays. *Cell Stem Cell* **2**, 313–9 (2008).
8. Dawson, E., Mapili, G., Erickson, K., Taqvi, S. & Roy, K. Biomaterials for stem cell differentiation. *Adv. Drug Deliv. Rev.* **60**, 215–28 (2008).
9. Mimeault, M. & Batra, S. K. Concise review: recent advances on the significance of stem cells in tissue regeneration and cancer therapies. *Stem Cells* **24**, 2319–45 (2006).
10. Evans, N. D., Gentleman, E. & Polak, J. M. Scaffolds for stem cells. *Mater. Today* **9**, 26–33 (2006).
11. Mitjavila-Garcia, M. T., Simonin, C. & Peschanski, M. Embryonic stem cells: meeting the needs for cell therapy. *Adv. Drug Deliv. Rev.* **57**, 1935–43 (2005).
12. Li, Y., Kniss, D., Lasky, L. & Yang, S.-T. Culturing and differentiation of murine embryonic stem cells in a three-dimensional fibrous matrix. *Cytotechnology* **41**, 23–35 (2003).
13. Chambers, I. & Smith, A. Self-renewal of teratocarcinoma and embryonic stem cells. *Oncogene* **23**, 7150–60 (2004).
14. Andrews, P. W. *et al.* Embryonic stem (ES) cells and embryonal carcinoma (EC) cells: opposite sides of the same coin. *Biochem. Soc. Trans.* **33**, 1526–30 (2005).

15. Rollini, P., Kaiser, S., Faes-van't Hull, E., Kapp, U. & Leyvraz, S. Long-term expansion of transplantable human fetal liver hematopoietic stem cells. *Blood* **103**, 1166–70 (2004).
16. Suen, P. M. & Leung, P. S. Pancreatic stem cells: A glimmer of hope for diabetes? *J. Pancreas* **6**, 422–424 (2005).
17. Tarasenko, Y. I., Yu, Y., Jordan, P. M., Bottenstein, J. & Wu, P. Effect of growth factors on proliferation and phenotypic differentiation of human fetal neural stem cells. *J. Neurosci. Res.* **78**, 625–36 (2004).
18. Forbes, S., Vig, P., Poulson, R., Thomas, H. & Alison, M. Hepatic stem cells. *J. Pathol.* **197**, 510–8 (2002).
19. Modlin, I. M., Kidd, M., Lye, K. D. & Wright, N. A. Gastric stem cells: An update. in *Keio Journal of Medicine* **52**, 134–137 (2003).
20. Tumber, T. *et al.* Defining the epithelial stem cell niche in skin. *Science* **303**, 359–63 (2004).
21. Woodward, W. A., Chen, M. S., Behbod, F. & Rosen, J. M. On mammary stem cells. *J. Cell Sci.* **118**, 3585–94 (2005).
22. Leri, A., Kajstura, J. & Anversa, P. Cardiac stem cells and mechanisms of myocardial regeneration. *Physiol. Rev.* **85**, 1373–416 (2005).
23. Lutolf, M. P. & Blau, H. M. Artificial stem cell niches. *Adv. Mater.* **21**, 3255–68 (2009).
24. Lutolf, M. P., Gilbert, P. M. & Blau, H. M. Designing materials to direct stem-cell fate. *Nature* **462**, 433–41 (2009).
25. Scadden, D. T. The stem-cell niche as an entity of action. *Nature* **441**, 1075–1079 (2006).
26. Halbleib, J. M. & Nelson, W. J. Cadherins in development: cell adhesion, sorting, and tissue morphogenesis. *Genes Dev.* **20**, 3199–214 (2006).
27. Scott, L. M., Priestley, G. V. & Papayannopoulou, T. Deletion of 4 Integrins from Adult Hematopoietic Cells Reveals Roles in Homeostasis, Regeneration, and Homing. *Mol. Cell. Biol.* **23**, 9349–9360 (2003).
28. Whetton, A. D. & Graham, G. J. Homing and mobilization in the stem cell niche. *Trends Cell Biol.* **9**, 233–238 (1999).
29. Daley, W. P., Peters, S. B. & Larsen, M. Extracellular matrix dynamics in development and regenerative medicine. *J. Cell Sci.* **121**, 255–264 (2008).

30. Lanniel, M. *et al.* Substrate induced differentiation of human mesenchymal stem cells on hydrogels with modified surface chemistry and controlled modulus. *Soft Matter* **7**, 6501 (2011).
31. Pek, Y. S., Wan, A. C. A. & Ying, J. Y. The effect of matrix stiffness on mesenchymal stem cell differentiation in a 3D thixotropic gel. *Biomaterials* **31**, 385–391 (2010).
32. Reilly, G. C. & Engler, A. J. Intrinsic extracellular matrix properties regulate stem cell differentiation. *J. Biomech.* **43**, 55–62 (2010).
33. Kraehenbuehl, T. P., Langer, R. & Ferreira, L. S. Three-dimensional biomaterials for the study of human pluripotent stem cells. *Nat. Methods* **8**, 731–736 (2011).
34. Cukierman, E., Pankov, R., Stevens, D. R. & Yamada, K. M. Taking Cell-Matrix Adhesions to the Third Dimension. *Sci.* **294**, 1708–1712 (2001).
35. Lutolf, M. P. & Hubbell, J. A. Synthetic biomaterials as instructive extracellular microenvironments for morphogenesis in tissue engineering. *Nat. Biotechnol.* **23**, 47–55 (2005).
36. Mendonça, G. *et al.* The effects of implant surface nanoscale features on osteoblast-specific gene expression. *Biomaterials* **30**, 4053–62 (2009).
37. Stevens, M. M. & George, J. H. Exploring and engineering the cell surface interface. *Science* **310**, 1135–1138 (2005).
38. O'Brien, F. J., Harley, B. A., Yannas, I. V. & Gibson, L. J. The effect of pore size on cell adhesion in collagen-GAG scaffolds. *Biomaterials* **26**, 433–441 (2005).
39. Yannas, I. V. *Tissue and organ regeneration in adults.* (Springer, 2001).
40. Silva, G. A. *et al.* Selective Differentiation of Neural Progenitor Cells by High - Epitope Density Nanofibers. *Science (80- )*. **303**, 1352–1355 (2004).
41. Iyer, K. V., Pulford, S., Mogilner, A. & Shivashankar, G. V. Mechanical activation of cells induces chromatin remodeling preceding MKL nuclear transport. *Biophys. J.* **103**, 1416–28 (2012).
42. Nava, M. M., Raimondi, M. T. & Pietrabissa, R. Controlling self-renewal and differentiation of stem cells via mechanical cues. *J. Biomed. Biotechnol.* **2012**, 797410 (2012).
43. McBeath, R., Pirone, D. M., Nelson, C. M., Bhadriraju, K. & Chen, C. S. Cell shape, cytoskeletal tension, and RhoA regulate stem cell lineage commitment. *Dev. Cell* **6**, 483–495 (2004).

44. Parekh, S. H. *et al.* Modulus-driven differentiation of marrow stromal cells in 3D scaffolds that is independent of myosin-based cytoskeletal tension. *Biomaterials* **32**, 2256–64 (2011).
45. Evans, N. D. *et al.* Substrate stiffness affects early differentiation events in embryonic stem cells. *Eur. Cells Mater.* **18**, 1–13 (2009).
46. Engler, A. J., Sen, S., Sweeney, H. L. & Discher, D. E. Matrix elasticity directs stem cell lineage specification. *Cell* **126**, 677–89 (2006).
47. Discher, D. E., Janmey, P. & Wang, Y. Tissue Cells Feel and Respond to the Stiffness of Their Substrate. *Sci* **310**, 1139–1143 (2005).
48. Rowlands, A. S., George, P. A. & Cooper-White, J. J. Directing osteogenic and myogenic differentiation of MSCs: interplay of stiffness and adhesive ligand presentation. *Am. J. Physiol. Cell Physiol.* **295**, C1037–C1044 (2008).
49. Dawson, J. I. *et al.* Development of specific collagen scaffolds to support the osteogenic and chondrogenic differentiation of human bone marrow stromal cells. *Biomaterials* **29**, 3105–16 (2008).
50. Bissell, D. M., Arenson, D. M., Maher, J. J. & Roll, F. J. Support of cultured hepatocytes by a laminin-rich gel. Evidence for a functionally significant subendothelial matrix in normal rat liver. *J. Clin. Invest.* **79**, 801–812 (1987).
51. Brun, P. *et al.* Chondrocyte aggregation and reorganization into three-dimensional scaffolds. *J. Biomed. Mater. Res.* **46**, 337–346 (1999).
52. Khademhosseini, A. & Bong, G. C. Microscale technologies for tissue engineering. in *2009 IEEE/NIH Life Science Systems and Applications Workshop, LiSSA 2009* 56–57 (2009). doi:10.1109/LISSA.2009.4906708
53. Maruo, S., Nakamura, O. & Kawata, S. Three-dimensional microfabrication with two-photon-absorbed photopolymerization. *Opt. Lett.* **22**, 132–134 (1997).
54. Arnal-Pastor, M., Vallés-Lluch, A., Keicher, M. & Pradas, M. M. Coating typologies and constrained swelling of hyaluronic acid gels within scaffold pores. *J. Colloid Interface Sci.* **361**, 361–369 (2011).
55. Blan, N. R. & Birla, R. K. Design and fabrication of heart muscle using scaffold-based tissue engineering. *J. Biomed. Mater. Res. - Part A* **86**, 195–208 (2008).
56. Croll, T. I., O'Connor, A. J., Stevens, G. W. & Cooper-White, J. J. A blank slate? Layer-by-layer deposition of hyaluronic acid and chitosan onto various surfaces. *Biomacromolecules* **7**, 1610–1622 (2006).

57. Hollister, S. J. Porous scaffold design for tissue engineering. *Nat. Mater.* **4**, 518–524 (2005).
58. Yeong, W.-Y., Chua, C.-K., Leong, K.-F. & Chandrasekaran, M. Rapid prototyping in tissue engineering: challenges and potential. *Trends Biotechnol.* **22**, 643–652 (2004).
59. Hutmacher, D. W., Sittering, M. & Risbud, M. V. Scaffold-based tissue engineering: Rationale for computer-aided design and solid free-form fabrication systems. *Trends in Biotechnology* **22**, 354–362 (2004).
60. National Institute of Standard Technology, NIST.
61. Claeysens, F. *et al.* Three-dimensional biodegradable structures fabricated by two-photon polymerization. *Langmuir* **25**, 3219–3223 (2009).
62. Ovsianikov, A. *et al.* Laser fabrication of three-dimensional CAD scaffolds from photosensitive gelatin for applications in tissue engineering. *Biomacromolecules* **12**, 851–858 (2011).
63. Park, S. H., Yang, D. Y. & Lee, K. S. Two-photon stereolithography for realizing ultraprecise three-dimensional nano/microdevices. *Laser Photonics Rev.* **3**, 1–11 (2009).
64. Gattass, R. R. & Mazur, E. Femtosecond laser micromachining in transparent materials. *Nature Photonics* **2**, 219–225 (2008).
65. Glezer, E. N. *et al.* Three-dimensional optical storage inside transparent materials. *Opt. Lett.* **21**, 2023–2025 (1996).
66. Engelhardt, S. *et al.* Fabrication of 2D protein microstructures and 3D polymer-protein hybrid microstructures by two-photon polymerization. *Biofabrication* **3**, 025003 (2011).
67. Melissinaki, V. *et al.* Direct laser writing of 3D scaffolds for neural tissue engineering applications. *Biofabrication* **3**, 045005 (2011).
68. Heller, C. *et al.* Vinylcarbonates and vinylcarbmates: Biocompatible monomers for radical photopolymerization. *J. Polym. Sci. Part A Polym. Chem.* **49**, 650–661 (2011).
69. Le Harzic, R. *et al.* Sub-100 nm nanostructuring of silicon by ultrashort laser pulses. *Opt. Express* **13**, 6651–6656 (2005).
70. Tayalia, P., Mendonca, C. R., Baldacchini, T., Mooney, D. J. & Mazur, E. 3D cell-migration studies using two-photon engineered polymer scaffolds. *Adv. Mater.* **20**, 4494–4498 (2008).

71. Ovsianikov, A. *et al.* Ultra-low shrinkage hybrid photosensitive material for two-photon polymerization microfabrication. *ACS Nano* **2**, 2257–62 (2008).
72. Joddar, B. & Ito, Y. Artificial niche substrates for embryonic and induced pluripotent stem cell cultures. *J. Biotechnol.* **168**, 218–28 (2013).
73. Stankevičiūsa, E., Malinauskas, M. & Račiukaitis, G. Fabrication of scaffolds and micro-lenses array in a negative photopolymer SZ2080 by multi-photon polymerization and four-femtosecond-beam interference. in *Physics Procedia* **12**, 82–88 (2011).
74. Raimondi, M. *et al.* Optimization of Femtosecond Laser Polymerized Structural Niches to Control Mesenchymal Stromal Cell Fate in Culture. *Micromachines* **5**, 341–358 (2014).
75. Peppas, N. A., Hilt, J. Z., Khademhosseini, A. & Langer, R. Hydrogels in Biology and Medicine: From Molecular Principles to Bionanotechnology. *Adv. Mater.* **18**, 1345–1360 (2006).
76. Drury, J. L. & Mooney, D. J. Hydrogels for tissue engineering: Scaffold design variables and applications. *Biomaterials* **24**, 4337–4351 (2003).
77. Flory, P. J. *Principles\_of\_Polymer\_Chemistry*. 672 (1953).
78. Li, Q. *et al.* Biodegradable and photocrosslinkable polyphosphoester hydrogel. *Biomaterials* **27**, 1027–1034 (2006).
79. Jeon, O. *et al.* Mechanical properties and degradation behaviors of hyaluronic acid hydrogels cross-linked at various cross-linking densities. *Carbohydr. Polym.* **70**, 251–257 (2007).
80. Baier Leach, J., Bivens, K. A., Patrick Jr., C. W. & Schmidt, C. E. Photocrosslinked hyaluronic acid hydrogels: Natural, biodegradable tissue engineering scaffolds. *Biotechnol. Bioeng.* **82**, 578–589 (2003).
81. Gil, E. S. & Hudson, S. M. Stimuli-responsive polymers and their bioconjugates. *Progress in Polymer Science (Oxford)* **29**, 1173–1222 (2004).
82. Lee, C. H., Singla, A. & Lee, Y. Biomedical applications of collagen. *Int. J. Pharm.* **221**, 1–22 (2001).
83. Angele, P. *et al.* Characterization of esterified hyaluronan-gelatin polymer composites suitable for chondrogenic differentiation of mesenchymal stem cells. *J. Biomed. Mater. Res. A* **91**, 416–27 (2009).



## 2. Biomolecular patterning technologies for living cell arrays



## 2.1 General introduction

The selective and spatially resolved chemical patterning of biomaterials has gained increasingly attention due to its promising biomedical applications including biosensing, tissue engineering, fundamental biological studies *etc*<sup>1-3</sup>. Particularly, it has been recognized as one of the key technologies for rare cells sorting and capturing and for the analysis of individual cellular processes. In vitro traditional cell cultures study the average behavior within a heterogeneous population of cells in response to external stimuli, but cell behavior can vary significantly from cell to cell. Conversely, by controlling the spatial localization of biochemical cues that affect cells adherence, it is possible to indirectly pattern and physically isolate large numbers of individual cells. Depending on whether the printed biomolecules are more adhesive or less adhesive than the surrounding substrate, the cells will preferentially localize onto or avoid the stamped regions, respectively. These living-cells microarrays represent experimental platforms for delivering environmental stimuli (e.g. soluble factors, extracellular matrix, chemical drugs, *etc.*) and measuring the resulting response of a single cell or of colonies of specific cells population, instead of averaging the response of a whole population<sup>4</sup>. Moreover, living-cells assays provide new insights into the molecular mechanisms enabling to identify genetic determinant of diseases<sup>5</sup>, to discover modulators of cellular functions, and to study the complex interactions of cells with their environment<sup>6</sup>. Actually, cell microarrays can be created not only by the formation of biological ligands arrays to which cells specifically attach, but also by the direct printing of cells on a substrate. As an example, ink-jet printers have been adapted to print cells<sup>8</sup>, or dielectrophoretic techniques that exploit cells different dielectric properties to separate cells using an array of electrodes<sup>9</sup>. However, direct cell-arraying remains particularly challenging because process conditions can have a deleterious effect on cell physiology and viability. Instead, printing baits with high specificity for cell adhesion seems the most promising technique. Moreover,

cell arrays can give more information when typical cell in vivo interactions are reproduced.

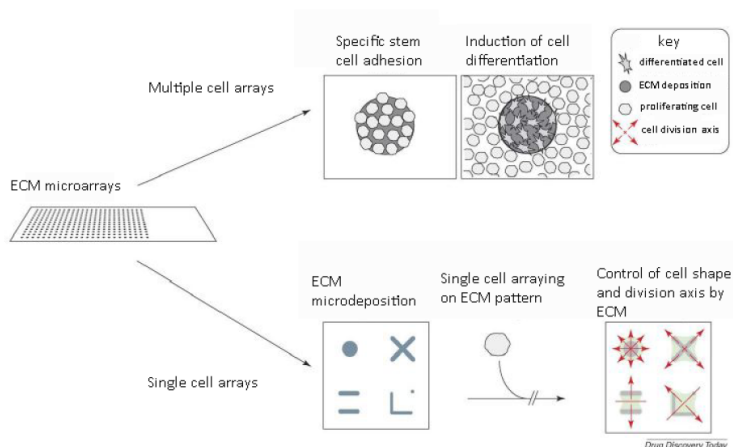


Figure 1. Example of living-cells microarrays application. Extracellular matrix (ECM) compounds can be selectively micro-printed for several scopes: arraying multiple cells on ECM patterns to study ECM role in adhesion and differentiation mechanisms; arraying single cells to control cell shape while adhering and the consequent orientation of the division axis<sup>5,7</sup>.

Therefore, this microarray technology relies on fidelity of affinity interactions between a surface-bound bait and its cell target<sup>10</sup>. Different kind of chemicals can be exploited as baits including peptides<sup>11</sup>, antibodies<sup>12</sup>, ECM components such as ECM proteins and proteoglycans<sup>13</sup>. The way in which baits are immobilized depends on the physicochemical and chemical properties of both surface and baits and deeply affects the cell-capture efficiency of the microarray. In fact, especially when working with peptides or proteins, immobilization may lead to partial or complete loss of baits activity, due to random orientation and structural deformation. Physisorption, chemisorption and bioaffinity immobilization are the three main mechanisms, which have been investigated in the past years for developing several immobilization strategies<sup>14–16</sup>. Biomolecules physical adsorption results from mutual attractive forces including electrostatic, ionic, hydrophobic or hydrophilic. Due to the fact that this phenomenon is entropically driven, each molecule form contacts in different orientations as many as are necessary for minimizing repulsive interactions with the substrate thus resulting in a heterogeneous and randomly oriented baits layer<sup>17</sup>. Moreover,

the weak protein attachment can cause biomolecules to be removed by buffers or detergents. In order to overcome these problems, biomolecules baits are often irreversibly chemically linked to the surface through strong covalent bonds formation between the side-chain exposed functional groups of the baits and suitably modified surfaces. Carboxylic acid, aldehyde, epoxy and maleimide are the most common functional/reactive groups. Finally, bioaffinity immobilization exploits high-affinity ligand pairs to immobilize biomolecules with controlled orientation, providing stable immobilization similar to covalent coupling<sup>14,18</sup>. One of the most widely used is the biotin-avidin system<sup>19</sup>, in which the highly specific interaction and extraordinary affinity of biotin and for avidin family proteins results in strong and stable non covalent bonds<sup>20</sup>. Avidin is a glycosylated and positively charged protein present in the egg-white of birds, reptiles and amphibian. It is a highly stable tetrameric protein able to bind up to four molecules of biotin. Their association rate constant is  $7 \times 10^7 \text{ M}^{-1}\text{s}^{-1}$  at  $\text{pH} = 5$  and  $T = 25^\circ\text{C}$  and its dissociation constant is  $10^{-15}\text{M}$ . Streptavidin and neutravidin are closely related tetrameric protein, with similar affinity to biotin, but differing in other aspects, such as molecular weight, amino acid composition, and isoelectrical point (Ip). Biotin is a naturally occurring vitamin found in all living cells. The bicyclic ring is involved in the interaction with avidin, while the carboxyl group on the opposite side chain can be exploited for biotin-conjugation to the surfaces or with other molecules.

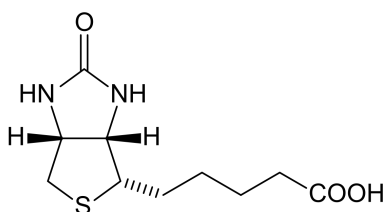


Figure 2. Chemical structure of biotin.

In fact, the general approach involves biotin direct immobilization via adsorption or covalent coupling with the surfaces. The biotin layer promotes an ordered avidin overstructure with two biotin-binding sites facing the surface and the other two facing outward. Finally, depending on the specific interaction or

molecular mechanism to investigate, the avidin layer constitutes a versatile platform where specific biotinylated baits can be self-assembled to capture its cell target. Thus, printing baits with high specificity for cell adhesion emerges as the most promising techniques, while the possibility to reproduce typical cell interactions explain why cell arrays are emerging as important tools for drug discovery, toxicology, functional genomics and investigation of cellular microenvironments.

### 2.1.1 Example of application: Hyaluronic acid and its role in tumor growth and metastasis.

Hyaluronic acid (HA) is a glycosaminoglycan (GAG) whose structure is composed of alternating units of N-acetyl-d-glucosamine and D-glucuronic acid linked together by alternating  $\beta$ -1,4 and  $\beta$ -1,3 glycosidic bonds. Physiologically, it is located in the extracellular matrix (ECM) of many soft connective tissues where it plays important roles: the maintenance of viscoelasticity of liquid connective tissues such as the vitreous humor, cartilage and vocal folds; control of tissue hydration and water transport and supramolecular assembly of proteoglycans in the ECM<sup>21</sup>.

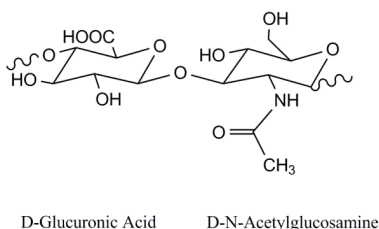


Figure 3. Molecular structure of HA.

Moreover, HA interacts with its cell surface receptors hyaladherins (CD44 or RHAMM) to activate various signalling pathways. These signalling control numerous receptor-mediated activities such as cell detachment, mitosis, migration, and angiogenesis but are also involved in tumor development and metastasis. In particular, several studies have demonstrated a close correlation between tumor growth and HA-rich ECM<sup>22,23</sup> as a consequence of the interactions

of surface adhesion molecule CD44 in cancer cells with CD44-receptor overexpressed by HA. CD44 is an adhesion molecule implicated in cell-cell and cell-matrix adhesion and represents the major cell surface receptor for HA, whose interaction with could be better understood through the 3D model of CD44 obtained by X-ray crystallography<sup>24</sup>.

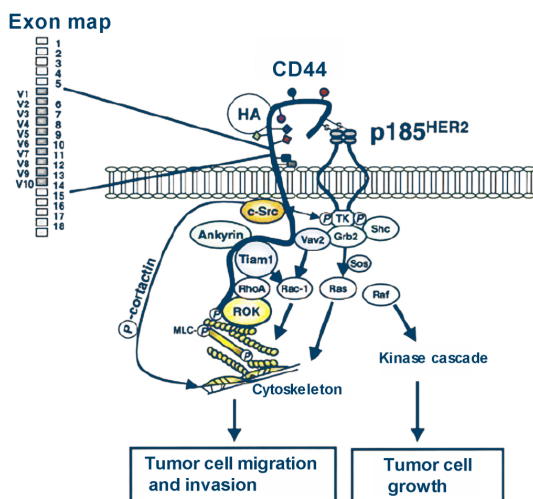


Figure 4. A current model for hyaluronan-CD44 specific interactions. CD44 is coupled with at least two tyrosine-kinases so that its interaction with HA is translated into kinase signaling pathways leading to multiple functions such as tumor cell adhesion, proliferation/growth, migration, and invasion.

CD44 is a transmembrane protein that is encoded by a single gene containing 19 exons. Ten of these exons are subjected to alternative splicing as well as variations in N- or O-glycosylation thus generating multiple CD44 isoforms of different molecular sizes (85÷230 kDa)<sup>25,26</sup>. The smallest CD44 molecule (CD44s), which lacks variant exons, is expressed by both normal and cancer cells, while the CD44 isoforms containing a variable number of exon insertions (CD44v) are mainly expressed by cancer cells<sup>27</sup>. All CD44 isoforms contain a hyaluronan-binding site in their distal extracellular domain, which is composed of 100 residues that interact through ionic bonds with the carboxylic acid groups of the glycosaminoglycan<sup>28</sup>. However, the HA-binding ability of different isoforms is modulated by changes in glycosylation and increases with increasing insertion of variably spliced exons. CD44 isoforms bind selectively with hyaladherins

cytoskeletal proteins expressed by HA, which creates soft matrices due to its hydration effect behaviour<sup>29</sup>. In tumor tissues, the binding of CD44v to hyaluronan induces proteolysis of the matrix that has a duplex effect in tumor growth and spreading. Firstly, it facilitates the detachment of malignant cancer cells from their confined tumor area and promotes the spread of malignant cells to distant sites. Furthermore, the HA expansion upon hydration provide a suitable environment to support this malignant cell migration. Secondly, the partial degradation of HA encourages angiogenesis, a vital requirement for cancer progression. Hence, tumor progression and angiogenesis depend on levels of both HA and hyaluronidase, the enzyme responsible for HA degradation<sup>30</sup>. Due to the fact that HA represents a requisite component of the microenvironment of cancer cells, in recent years it has been exploited in tissue engineering strategies for the artificial fabrication of 3D tumor tissues. These have been exploited as in vitro models in order to better understand the tumor biology and to develop drugs<sup>31</sup>. Conversely, the possibility to realize selectively micro-patterned HA surfaces for the immobilization of single cancer cells should enable higher-resolution visualization of cancer cell interactions thus deeper insights into the understanding of the specific interaction between HA and CD44 isoform<sup>32</sup>. The main scope of these cell arrays would be the formulation of selective therapies and diagnosis exploiting CD44v as promising target molecules.

## 2.1.2 Example of application: Heparin role in malaria-infected red blood cells

Malaria is an acute and/or chronic infectious disease representing one of the leading causes of morbidity and mortality in tropical and subtropical regions of the world<sup>33,34</sup>. It is caused by protozoan parasites of the genus *Plasmodium* that is transmitted through the bite of an infected female *Anopheles* mosquito. Particularly, among the four species of parasite that can infect humans, *Plasmodium falciparum* (*P. falciparum*) is the one causing the most deadly and severe cases<sup>35,36</sup>. Once injected into the bloodstream of the human host, *P. falciparum* sporozoites migrated to the liver, where they infect the liver cells (hepatocytes) and proliferate into thousands of merozoites. Merozoites rupture from the hepatocytes, enter the circulation and invade red blood cells (RBCs). Inside the erythrocytes, some parasites eventually differentiate into sexual stages, female or male gametocytes that are ingested by a mosquito and are essential for transmitting the infection to new hosts through the female mosquitoes. Conversely, the majority of parasites start an asexual division to produce daughter cells develop first into rings, and then into the late forms trophozoites and schizonts. Mature schizont contains around 20 merozoites that are released after *Plasmodium*-infected red blood cells (pRBCs) burst to invade further un-infected RBCs and start the blood cycle again. The blood-stage infection is responsible for all symptoms and pathologies of malaria and the virulence of the parasite is associated with the capacity of the pRBCs to adhere to endothelial cells (sequestration) and to non-infected erythrocytes (rosetting)<sup>36,37</sup>. These events may lead to the formation of clumps with the occlusion of the microvasculature that can cause impaired local oxygen delivery and thereby death of the human host<sup>38</sup>. Therefore, sequestration and rosetting are thought to play a major role in the fatal outcome of severe malaria and pRBCs can be considered main chemotherapeutic target<sup>39</sup>. Several studies revealed that the cytoadherence of pRBCs is mediated by *P. falciparum* erythrocyte membrane protein 1 (PfEMP1), a parasite-derived protein expressed at the surface of pRBCs. Moreover, PfEMP1 expresses glycosaminoglycan (GAG)-binding motifs that act as

rosetting ligand by binding to heparan sulfate (HS) or HS-like glycan molecules exposed on uninfected RBC<sup>40–42</sup>. X-rays crystallographic analyses revealed that the GAG-binding regions are polypeptides localized next to the N-terminal segment of PfEMP1, which are characterized by clusters of arginines and lysines that form high positive charged residues that electrostatically interact with the acidic groups of negatively charged, sulphated GAGs and particularly with HS and its derivative heparin<sup>43</sup>.

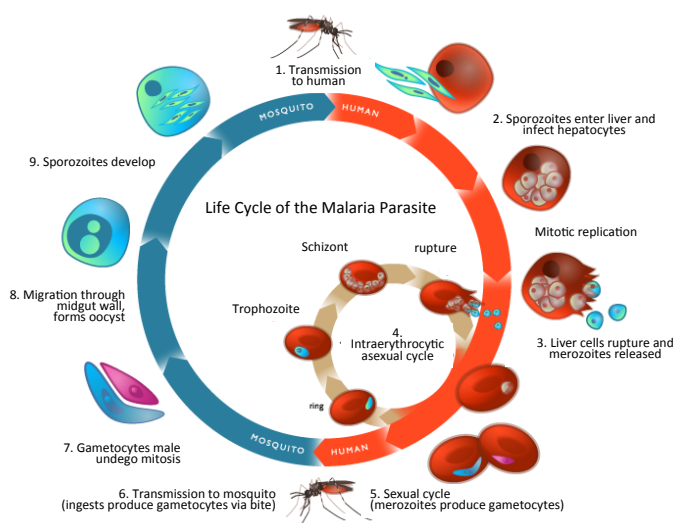


Figure 5. Life cycle of the malaria parasite *P. falciparum*, which is able to reach high parasitaemia because of greater flexibility in the receptor pathways used to invade all RBCs. Disease occurs only as a result of the asexual blood stage after the parasite leaves the liver and begins to invade and grown inside RBCs.

These are long carbohydrate chains consisting of uronic acid-(1-4)-d-glucosamine repeating disaccharide subunits variably modified by epimerization and N- and O-sulfation at different positions, resulting in a large numbers of complex sequences<sup>44</sup>. Particularly, heparin is the most extensively modified form of the glucosaminoglycans, and results as a highly sulfated HS. While the latter is expressed and secreted by almost all mammalian cells, heparin is synthesized just by connective tissue type mast cells. HS- and heparin-protein binding mediate many biological functions, but they are most well known for their anticoagulant activities<sup>45</sup>. Therefore, in order to enhance surface

hemocompatibility, they have been deeply investigated for the development and functionalization of blood contacting biomaterials<sup>46,47</sup>. However, once HS and in particular heparin had been demonstrated to have antimalarial activity and specific binding affinity for pRBCs vs non-infected<sup>37,40,48</sup>, they have been experimented for the development of efficacious drugs acting specifically on target cells, and on the formulation of new targeted drug delivery strategies.

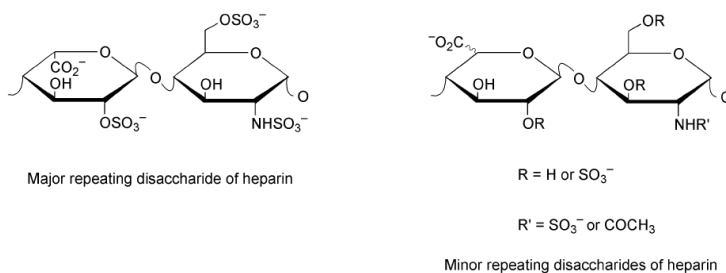


Figure 6. Molecular structures of the major and minor repeating units of heparin.

Heparin and HS-like molecules could be designed as competitors against pRBCs sequestration and rosetting, but also could be used as targeting agents to direct anti-malarial-carrying nanocapsules towards pRBCs with high specificity<sup>49,50</sup>. These targeted delivery systems would replace standard antimalarials administration methods according to which toxic drugs, offering little specificity regarding target cells, release free compound in the blood stream where it can be unspecifically removed by many tissues and organs before entering pRBCs<sup>51</sup>. Due to this lack of specificity, multiple drugs doses are requested to achieve therapeutic levels, but at the same time, their toxicity demands low concentrations, thus contributing to the development of resistant parasite strains<sup>52</sup>.

Nowadays, nanosized carriers have gained special attention with the aim of minimizing the side effects of malarian therapies by increasing drug bioavailability and selectivity. Antibody-functionalized liposomal nanovectors have been successfully synthesized for the targeted delivery of drugs, but antibodies expensive production together with their high immunogenicity limits their role as targeting elements<sup>49</sup>. Consequently, HS and HS-like glycans have

been considered as alternatives and first experimental studies *in vitro* showed promising results<sup>48,50</sup>. Finally, realizing negatively charged GAGs micro arrays would enrich the knowledge about their precise molecular interactions with pRBCs, thus supporting their use in the development of fast and cost-effective assembly of efficacious targeted drug delivery nanovectors<sup>53</sup>.

## 2.2 Biomolecules patterning technologies

Among different patterning technologies that have been developed, **photolithography** is the one that, starting from microelectronic industry, has been used most extensively in a variety of application fields, including for protein and cells patterning<sup>54-56</sup>. Photolithographic conventional technique uses light passing through a patterned photo-mask to selectively irradiate a photosensitive resist layer (photo-resists), whose solubility characteristics are altered upon light irradiation to render them either soluble or insoluble in particular solvent (positive and negative tone respectively).

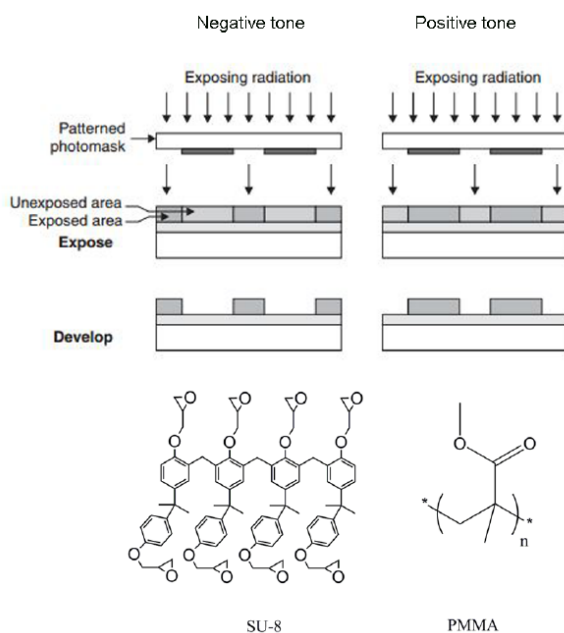


Figure 7. Scheme of the photolithographic process for the two types of existing photo-resists. On the left, negative-tone becomes less soluble when exposed to UV light (e.g. SU-8). On the right, PMMA as an example of positive resist which becomes more soluble when exposed to UV radiation<sup>57</sup>.

The photo-mask placed between the light source and the resist contains the negative of the pattern to be realized, and considering UV light, two are the possible alternatives: quartz photo-masks with a patterned chromium layer that absorbs UV-radiation or polyester masks with a drawn ink pattern realized with

a Computer-Aided Design software. By using polyester photo-masks the cost of the whole process can be effectively reduced, in fact one of the major drawbacks of photolithography is that expensive equipment are usually required thus limiting large scale diffusion in standard laboratories. However, various photolithographic based processes have been developed to achieve biomolecular patterning. Mask-assisted photoablation was exploited for selective removal of antibody-resistant coatings composed of proteins, such as BSA<sup>58</sup> or laminin<sup>59</sup>, which were pre-adsorbed as anti-fouling agents onto bare silicon or polymeric surfaces. The areas where the coating has been removed enable selective physical biomolecules adsorption. Other approaches have been described that employ thiol-terminated siloxane films, previously patterned by UV-light irradiation, to selectively immobilized proteins<sup>60</sup>. Photochemical activations of light sensitive molecules is also widely used as a versatile method to pattern different molecules. In particular, several studies exploited the combination of photoactivation of a UV-sensitive biotin and its high affinity with avidin to develop biotin-conjugated enzymes patterns<sup>20,61,62</sup>.

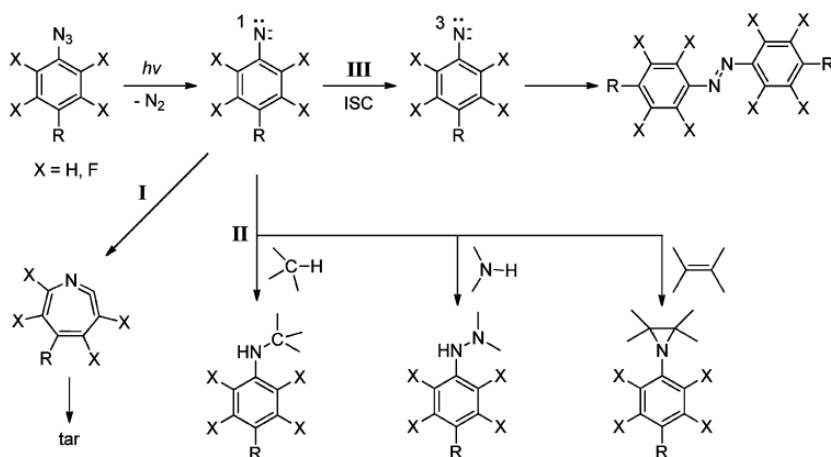


Figure 8. Simplified description of phenylazide photo-chemistry: ring expansion (I), insertion and addition reactions (II), and intersystem crossing (III).

Following this approach, a thin film of photo-activable biotin is first dried on a surface and subsequently exposed to light through a mask, yielding a pattern of biotin covalently coupled to the underlying surface. The biotin patterned is then

used for binding streptavidin, the latter containing two pairs of biotin-binding site on opposite sides. One pair could be used for complexation with the surface bound biotin, while leaving the other pair available for further binding any biotin-conjugated molecule via a biotin-streptavidin-biotin bridge. Generally, photo-activable forms of biotin are heterobifunctional molecules carrying a biotin head, a linker arm and a photo-activable aryl azide moiety<sup>63</sup>. Upon exposure to UV light the azide group converts into an aryl-nitrene which is capable of covalently attaching to C-H, N-H and C=C bonds<sup>64</sup>. Major limitations deriving from exploiting photolithographic techniques for biomolecular patterning, are related to the harsh process conditions such as the usage of photoresist developers and heat treatment, which can cause denaturation of sensitive biomolecules. Moreover, photolithography should also be not compatible with compounds that are sensitive to light or etchants and is not suited to pattern non-planar surfaces. All these drawbacks, together with the high costs associated, prompted the development of alternative non-photolithographic cost-effective techniques<sup>65</sup>, such as **soft-lithographic** techniques, whose key element is an elastomeric stamp used to create patterns on a wide variety of surfaces<sup>65-67</sup>. Among soft-lithographic techniques, **micro-contact printing ( $\mu$ -CP)**, consisting in the transfer of an ink from the stamps to the substrate, was first used in 1993 to patterning alkyl thiols on gold substrates<sup>66</sup> and later extended to print various organic molecules, proteins and biopolymers<sup>68,69</sup>. Polydimethylsiloxane (PDMS) is the most widely used material to make  $\mu$ -CP stamps<sup>70</sup>. PDMS stamps are prepared by casting a mixture of the elastomer precursor and curing agent over a silicon master obtained by photolithography. After curing, the replicated elastomer is released from the mould master, having transferred a reverse structure of the mould master. The widespread use of PDMS is attributed to its properties. First, PDMS low Young Modulus enables it to conform to both planar and non-planar surfaces with good sealing properties (conformal contact). Second, it is characterized by low surface energy, approximately (20 mJ/m<sup>2</sup>), which facilitates easy release from the mould. Finally, PDMS is permeable to oxygen, chemically inert and transparent. Some

drawbacks are related to its elastomeric character. In sub-micrometric patterns, there could be problems of pairing or sagging for a too high or a too low aspect ratio respectively. Shrinking phenomena can also occur upon curing. Moreover, PDMS suffers from swelling in contact with nonpolar solvents such as toluene and hexane<sup>72,73</sup>.

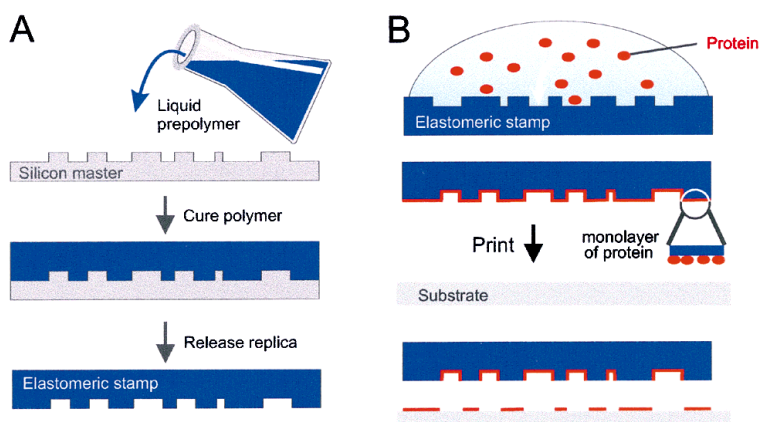


Figure 9. A) Scheme illustrating the fabrication of the PDMS stamp fabrication by replica of the silicon master. PDMS is simply poured on the silicon master and cross-linked for 48h at room temperature, then it is peeled off from the substrate. B) PDMS stamp is equilibrated with the protein solution to be transferred; air dried and brought in contact with the surface<sup>71</sup>.

After peeling from the master, the stamps are inked with the protein solution to be printed, air-dried and brought into conformal contact with the substrate.

In order to achieve efficient molecules transfer, the ink affinity to the underlying substrate must be higher than that for the PDMS stamp. For example, the hydrophobicity of PDMS could limit its application when printing “biological inks”, because polar molecules such as proteins or DNA tend to be repelled by the hydrophobic PDMS surface, resulting in poor stamp inking and as a consequence in a inefficient transfer. The hydrophobic nature can also lead to protein denaturation. However, the stamp surface properties can be chemically/physically modified to give appropriate interfacial interactions with materials<sup>74</sup>.

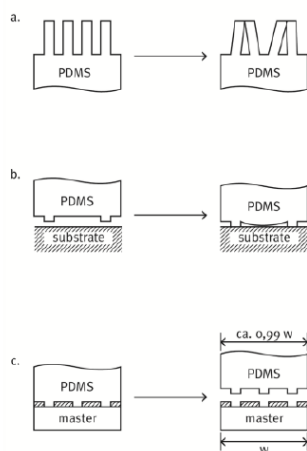


Figure 10. Possible deformations and distortions of microstructures in the surfaces originating from the elastomeric nature of PDMS: a) Pairing, b) sagging, c) shrinking.

For instance, direct  $\mu$ -CP of positively-charged polylysine protein was achieved by plasma oxidizing the stamp to render it more hydrophilic thus allowing the ink adsorption onto the PDMS stamp and its subsequent transfer on the substrate<sup>75</sup>. Otherwise, in order to overcome difficulties deriving from PDMS low polarity and low mechanical stability, several polymers have been investigated as alternatives to PDMS. Poly(ether-block-ester) as well as poly(styrene-block-butadiene-block-styrene) were successfully used<sup>70</sup>. The major advantage of these polyolefins is their higher mechanical strength, which makes them suitable for printing demanding aspect ratio patterns that would not be feasible using PDMS stamps. In the field of biochemistry agarose gel has been adapted for stamp fabrication and used to print proteins<sup>76</sup> and cells<sup>77</sup>.

Together with photolithography and soft-lithography, **ink-jet technology** has been used to fabricate protein patterns with spot size close to 100  $\mu\text{m}$ <sup>78,79</sup>. Following these techniques, a robotic spotter, equipped with actuated micropipettes, is exploited to deliver few nanoliters of protein solutions on different regions of the substrates. Noncontact and contact printing can be either exploited to transfer the protein spots. The former generally uses piezoelectrical or thermal technology to expel small droplets of solution, whereas in contact printing, each print pin directly applies the probe solution onto the microarray

surface<sup>80</sup>. The major advantage of spot-arraying techniques is that the proteins stay in hydrated conformation in solution during the patterning process, ensuring their biofunctionality. Moreover, its high flexibility enables multi protein patterning avoiding cross-contamination.

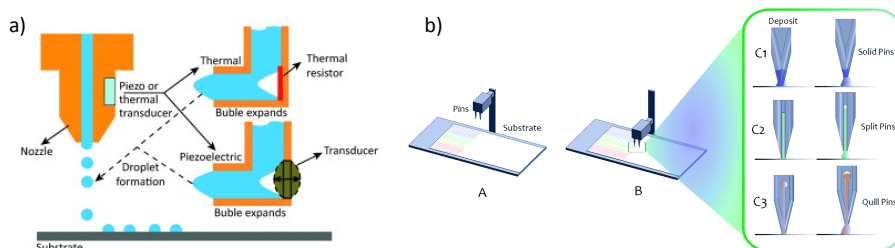


Figure 11. Scheme illustrating (a) noncontact and (b) contact printing processes. In noncontact pin printing, piezo or thermal transducer are used to expel small droplets of protein solution. In contact printing, the pin are loaded with print solution from a source plate and then contact the substrate surface to deposit protein solution<sup>81,82</sup>.

In recent years, other technologies have been developed to achieve molecular scale patterning, otherwise not possible with photolithography and soft lithography that are limited to micron-sized patterns. New possible nanolithographic technologies include **dip-pen nanolithography (DPN)**<sup>83</sup>, a direct-write scanning probe-based lithography that uses an ‘ink’-coated atomic force microscopy (AFM) tip to deliver molecules on a surface *via* a solvent meniscus achieving sub-50-nm resolution<sup>84</sup>. Nanoarrays of small organic molecules, polymers, DNA and proteins have been realized through AFM-based methods<sup>85,86</sup>.

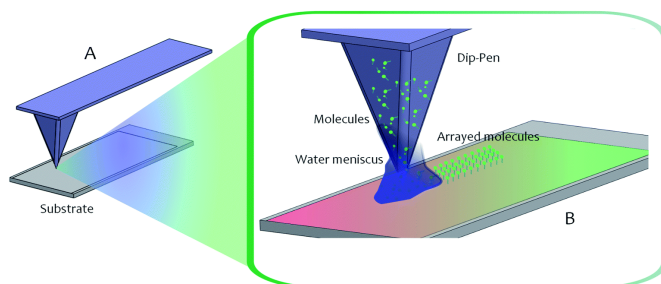


Figure 12. Schematic representation of the DPN process. A water meniscus is formed between the AFM tip, which is coated with “ink” molecules, and the solid substrate<sup>83</sup> and transports molecules to the surface in the desired pattern<sup>81</sup>.

## 2.3 Anti-fouling/fouling-release substrates

A fundamental issue in the development of micropatterned substrates for rare cell capture and isolation is represented by material selection. The performance of the final surface-capture arrays is strikingly affected by the choice of the substrate material that should meet specific requirements. Suitable materials should primarily show biocompatibility, biostability and resistance to biodegradation with low level of extractables that must be non-cytotoxic. However, even surface properties play a critical role in this performance<sup>10,15</sup>. In fact, microarray surfaces, usually immersed into aqueous biological fluids or cell culture media, must be capable of selectively immobilizing biomolecules baits in microscale patterned spots and hence, selectively capturing target cells, but also be efficient at eliminating not specific protein binding or cell capture anywhere else on the surface. To this end, materials showing anti-fouling and fouling-release properties have attracted a significant interest to be used either as surface coating material or as bulky material. Anti-fouling means preventing the adhesion of fouling organisms or protein in static conditions, while fouling release involves the possibility of removing them dynamically by the hydrodynamic forces exerted through a liquid flow and a wide number of parameters contributes to determine these surfaces characteristics. A well-known anti-fouling polymer largely applied in biomedical and biological research is poly(ethylene glycol) (PEG)<sup>87,88</sup>. The generally adopted approach is to minimize non-specific binding of a surface by depositing thin PEG layers. These surface modification can be performed either by PEG physically adsorption<sup>89</sup> or by PEG covalent immobilization<sup>90,91</sup>. Successful PEG deposition prevents both electrostatic and hydrophobic attractions by presenting an uncharged polar surface to the fluid. In fact, the efficacy of PEG as a biologically passivating surface has been linked to both its charge neutrality and to its solvated configuration when interacting with water<sup>92-94</sup>.

Recently, perfluoropolyethers (PFPEs) have also emerged as promising coating materials to be exploited for anti-biofouling<sup>95</sup>. Thanks to their anti-fouling and

fouling-release properties, PFPE functional oligomers are already widely used in marine field to prevent biofouling adhesion on ship hulls, thus reducing hydrodynamic drag and fuel consumption<sup>96,97</sup>. Conversely, in the biomedical field UV curable perfluoropolyether-dimethacrylates (PFPE-DMAs) have been investigated for device microfabrication<sup>98</sup> and more recently amphiphilic structures containing both hydrophilic and hydrophobic moieties have been proposed as potential fouling-release coatings<sup>99</sup>. Finally, other works in the literature have tested the effectiveness of other perfluoropolyether polymers as protein-adhesion resistant substrates<sup>95,100</sup>. The release properties of fluorinated polymers, and of polymeric materials in general, rely on their physico-chemical properties; in particular, surface tension and elastic modulus seem to play an important role. The relationship between surface free energy and bioadhesion has been deeply investigated in the literature. Preliminary experiments, performed to study the role of surface tension on the adhesion of blood proteins and platelets<sup>101</sup>, revealed that protein/fouling adhesion decreases linearly with surface tension up to 25 mN/m, which is the value of Polydimethylsiloxane (PDMS); a further diminishment of surface tension would not be beneficial, where as 20 ÷ 30 mJ/m<sup>2</sup> should be considered as the surface tension values range ideal in preventing bioadhesion<sup>101</sup>. However, more recent studies suggested that surface tension must be considered keeping in mind also the elastic modulus of the material. Moreover, also the coating thickness plays a role, since less force is needed to dislodge a fouling layer from a thicker coating<sup>102,103</sup>. For instance, a more comprehensive approach is to study fouling adhesion against  $(E\gamma)^{1/2}$  to study the effect of both elastic modulus and surface tension<sup>104,105</sup>. The latter is crucial for the initial attachment of proteins, while the former mainly affects the fouling release properties, since it induces the joint formed between the substrate and the protein to fail by peel rather than by shear. The dependence of fouling-release performance on  $(E\gamma)^{1/2}$  was first derived studying the joint between proteins and the coating in terms of fracture mechanics. The approach stems from the Griffith theory that shows how fracture of solids depends not only on surface energy but also on geometry and the elastic properties of the

materials. Considering the case of a thin film of thickness 't' and Young's modulus 'E' sandwiched between an infinite rigid plane and a disk of diameter 2a, the peel force can be expressed as following:

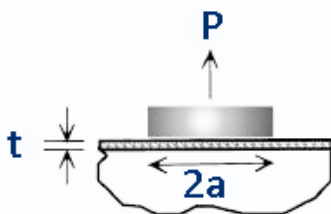


Figure 13. Scheme of an elastomeric film held between a rigid substrate and a rigid disk. P = peel force; a = contact radius; t = coating thickness.

$$P^2 = \frac{2\pi^2 k a^4 \gamma}{t}$$

where P is the peel force necessary to joint failure, a is the contact radius, t is the coating thickness and k is the bulk modulus, that is related to the elastic modulus through the Poisson coefficient as shown in the following equation:

$$E = 3K(1 - 2\nu)$$

combining the two equations it is evident the connection between fouling-release properties and  $(E\gamma)^{1/2}$ . Thus, PFPE polymers are undoubtedly promising fouling-release materials, having both low elastic modulus and low surface tension. However, it must be noted that other parameters such as surface reconstruction<sup>106</sup>, and surface roughness play a role in the assessment of fouling-release properties.

## 2.4 References

1. Veiseh, M., Zareie, M. H. & Zhang, M. Highly Selective Protein Patterning on Gold-Silicon Substrates for Biosensor Applications. *Langmuir* **18**, 6671–6678 (2002).
2. Chen, C. S. Geometric Control of Cell Life and Death. *Science (80-. )*. **276**, 1425–1428 (1997).
3. Asthana, A., Asthana, Y., Sung, I.-K. & Kim, D.-P. Novel transparent poly(silazane) derived solvent-resistant, bio-compatible microchannels and substrates: application in microsystem technology. *Lab Chip* **6**, 1200–1204 (2006).
4. Yarmush, M. L. & King, K. R. Living-cell microarrays. *Annu. Rev. Biomed. Eng.* **11**, 235–257 (2009).
5. Castel, D., Pitaval, A., Debily, M.-A. & Gidrol, X. Cell microarrays in drug discovery. *Drug Discov. Today* **11**, 616–22 (2006).
6. Théry, M. *et al.* The extracellular matrix guides the orientation of the cell division axis. *Nat. Cell Biol.* **7**, 947–953 (2005).
7. El-Ali, J., Sorger, P. K. & Jensen, K. F. Cells on chips. *Nature* **442**, 403–411 (2006).
8. Xu, T., Jin, J., Gregory, C., Hickman, J. J. & Boland, T. Inkjet printing of viable mammalian cells. *Biomaterials* **26**, 93–99 (2005).
9. Huang, Y. *et al.* Dielectrophoretic cell separation and gene expression profiling on microelectronic chip arrays. *Anal. Chem.* **74**, 3362–3371 (2002).
10. Gong, P. & Grainger, D. W. Nonfouling surfaces: a review of principles and applications for microarray capture assay designs. *Methods Mol. Biol.* **381**, 59–92 (2007).
11. Falsey, J. R., Renil, M., Park, S., Li, S. & Lam, K. S. Peptide and small molecule microarray for high throughput cell adhesion and functional assays. *Bioconjug. Chem.* **12**, 346–353 (2001).
12. Belov, L., De la Vega, O., Dos Remedios, C. G., Mulligan, S. P. & Christopherson, R. I. Immunophenotyping of leukemias using a cluster of differentiation antibody microarray. *Cancer Res.* **61**, 4483–4489 (2001).
13. Flaim, C. J., Chien, S. & Bhatia, S. N. An extracellular matrix microarray for probing cellular differentiation. *Nat. Methods* **2**, 119–125 (2005).
14. Rusmini, F., Zhong, Z. & Feijen, J. Protein immobilization strategies for protein biochips. *Biomacromolecules* **8**, 1775–1789 (2007).

15. Ganesan, R., Kratz, K. & Lendlein, A. Multicomponent protein patterning of material surfaces. *Journal of Materials Chemistry* **20**, 7322 (2010).
16. Blawas, A. S. & Reichert, W. M. Protein patterning. *Biomaterials* **19**, 595–609 (1998).
17. Norde, W. & Lyklema, J. Why proteins prefer interfaces. *J. Biomater. Sci. Polym. Ed.* **2**, 183–202 (1991).
18. Jonkheijm, P., Weinrich, D., Schröder, H., Niemeyer, C. M. & Waldmann, H. Chemical Strategies for Generating Protein Biochips. *Angew. Chemie Int. Ed.* **47**, 9618–9647 (2008).
19. Savage, D. *et al.* in *Avidin-Biotin Chemistry: A Handbook* 1–23 (1992).
20. Choi, H. J., Kim, N. H., Chung, B. H. & Seong, G. H. Micropatterning of biomolecules on glass surfaces modified with various functional groups using photoactivatable biotin. *Anal. Biochem.* **347**, 60–66 (2005).
21. Xu, X., Jha, A. K., Harrington, D. A., Farach-Carson, M. C. & Jia, X. Hyaluronic Acid-Based Hydrogels: from a Natural Polysaccharide to Complex Networks. *Soft Matter* **8**, 3280–3294 (2012).
22. Zhang, L., Underhill, C. B. & Chen, L. Hyaluronan on the surface of tumor cells is correlated with metastatic behavior. *Cancer Res.* **55**, 428–433 (1995).
23. Franzmann, E. J. *et al.* Expression of tumor markers hyaluronic acid and hyaluronidase (HYAL1) in head and neck tumors. *Int. J. Cancer* **106**, 438–445 (2003).
24. Teriete, P. *et al.* Structure of the Regulatory Hyaluronan Binding Domain in the Inflammatory Leukocyte Homing Receptor CD44. *Mol. Cell* **13**, 483–496 (2004).
25. Misra, S. *et al.* Hyaluronan–CD44 interactions as potential targets for cancer therapy. *FEBS J.* **278**, 1429–1443 (2011).
26. Naor, D., Sionov, R. V & Ish-Shalom, D. CD44: structure, function, and association with the malignant process. *Adv. Cancer Res.* **71**, 241–319 (1997).
27. Toole, B. P., Wight, T. N. & Tammi, M. I. Hyaluronan-cell interactions in cancer and vascular disease. *Journal of Biological Chemistry* **277**, 4593–4596 (2002).
28. Bajorath, J., Greenfield, B., Munro, S. B., Day, A. J. & Aruffo, A. Identification of CD44 Residues Important for Hyaluronan Binding and Delineation of the Binding Site. *J. Biol. Chem.* **273**, 338–343 (1998).

29. Turley, E. A., Noble, P. W. & Bourguignon, L. Y. W. Signaling Properties of Hyaluronan Receptors. *J. Biol. Chem.* **277**, 4589–4592 (2002).
30. Fishman, W. H. & Anlyan, A. J.  $\beta$ -Glucuronidase Activity in Human Tissues. Some Correlations With Processes of Malignant Growth and With the Physiology of Reproduction. *Cancer Res.* **7**, 808–817 (1947).
31. Prestwich, G. D. Evaluating drug efficacy and toxicology in three dimensions: Using synthetic extracellular matrices in drug discovery. *Acc. Chem. Res.* **41**, 139–148 (2008).
32. Dickinson, L. E., Ho, C. C., Wang, G. M., Stebe, K. J. & Gerecht, S. Functional surfaces for high-resolution analysis of cancer cell interactions on exogenous hyaluronic acid. *Biomaterials* **31**, 5472–5478 (2010).
33. Okiro, E. A. *et al.* Age patterns of severe paediatric malaria and their relationship to *Plasmodium falciparum* transmission intensity. *Malar. J.* **8**, 4 (2009).
34. Tuteja, R. Malaria - an overview. *FEBS J.* **274**, 4670–9 (2007).
35. Snow, R. W., Korenromp, E. L. & Gouws, E. Pediatric mortality in Africa: *Plasmodium falciparum* malaria as a cause or risk? in *American Journal of Tropical Medicine and Hygiene* **71**, 16–24 (2004).
36. Miller, L. H., Baruch, D. I., Marsh, K. & Doumbo, O. K. The pathogenic basis of malaria. *Nature* **415**, 673–9 (2002).
37. Udomsangpetch, R. *et al.* *Plasmodium falciparum*-infected erythrocytes form spontaneous erythrocyte rosettes. *J. Exp. Med.* **169**, 1835–1840 (1989).
38. Pasloske, B. L. & Howard, R. J. Malaria, the red cell, and the endothelium. *Annu. Rev. Med.* **45**, 283–295 (1994).
39. Griffith, K. S., Lewis, L. S., Mali, S. & Parise, M. E. Treatment of malaria in the United States: a systematic review. *JAMA* **297**, 2264–2277 PMID 17519416 (2007).
40. Barragan, A. *et al.* The Duffy-binding-like domain 1 of *Plasmodium falciparum* erythrocyte membrane protein 1 (PfEMP1) is a heparan sulfate ligand that requires 12 mers for binding. *Blood* **95**, 3594–3599 (2000).
41. Chen, Q. *et al.* Identification of *Plasmodium falciparum* Erythrocyte Membrane Protein 1 (PfEMP1) as the Rosetting Ligand of the Malaria Parasite *P. falciparum*. *J. Exp. Med.* **187**, 15–23 (1998).
42. Gangnard, S. *et al.* Functional and immunological characterization of the var2CSA-DBL5e{open} domain of a placental *Plasmodium falciparum* isolate. *Mol. Biochem. Parasitol.* **173**, 115–122 (2010).

43. Cardin, A. D. & Weintraub, H. J. R. Molecular modeling of protein-glycosaminoglycan interactions. *Arteriosclerosis* **9**, 21–32 (1989).
44. Rabenstein, D. L. Heparin and heparan sulfate: structure and function. *Nat. Prod. Rep.* **19**, 312–331 (2002).
45. Rodén, L. *Heparin: Chemical and Biological Properties Clinical Applications*. (Edward Arnold, 1989).
46. Huang, X. J., Guduru, D., Xu, Z. K., Vienken, J. & Groth, T. Immobilization of heparin on polysulfone surface for selective adsorption of low-density lipoprotein (LDL). *Acta Biomater.* **6**, 1099–1106 (2010).
47. Sperling, C., Salchert, K., Streller, U. & Werner, C. Covalently immobilized thrombomodulin inhibits coagulation and complement activation of artificial surfaces in vitro. *Biomaterials* **25**, 5101–5113 (2004).
48. Valle-Delgado, J. J., Urban, P. & Fernandez-Busquets, X. Demonstration of specific binding of heparin to Plasmodium falciparum-infected vs. non-infected red blood cells by single-molecule force spectroscopy. *Nanoscale* **5**, 3673–3680 (2013).
49. Urbán, P., Estelrich, J., Cortés, A. & Fernández-Busquets, X. A nanovector with complete discrimination for targeted delivery to Plasmodium falciparum-infected versus non-infected red blood cells in vitro. *J. Control. Release* **151**, 202–11 (2011).
50. Marques, J. *et al.* Application of heparin as a dual agent with antimalarial and liposome targeting activities toward Plasmodium-infected red blood cells. *Nanomedicine* **10**, 1719–1728 (2014).
51. Na-Bangchang, K. & Karbwang, J. Current status of malaria chemotherapy and the role of pharmacology in antimalarial drug research and development. *Fundamental and Clinical Pharmacology* **23**, 387–409 (2009).
52. White, N. J. The assessment of antimalarial drug efficacy. *Trends in Parasitology* **18**, 458–464 (2002).
53. Fernández-Busquets, X. Heparin-functionalized nanocapsules: Enabling targeted delivery of antimalarial drugs. *Future Med. Chem.* **5**, 737–739 (2013).
54. Kane, R. Patterning proteins and cells using soft lithography. *Biomaterials* **20**, 2363–2376 (1999).
55. Scouten, W. H. [2] A survey of enzyme coupling techniques. *Methods in Enzymology* **135**, 30–65 (1987).

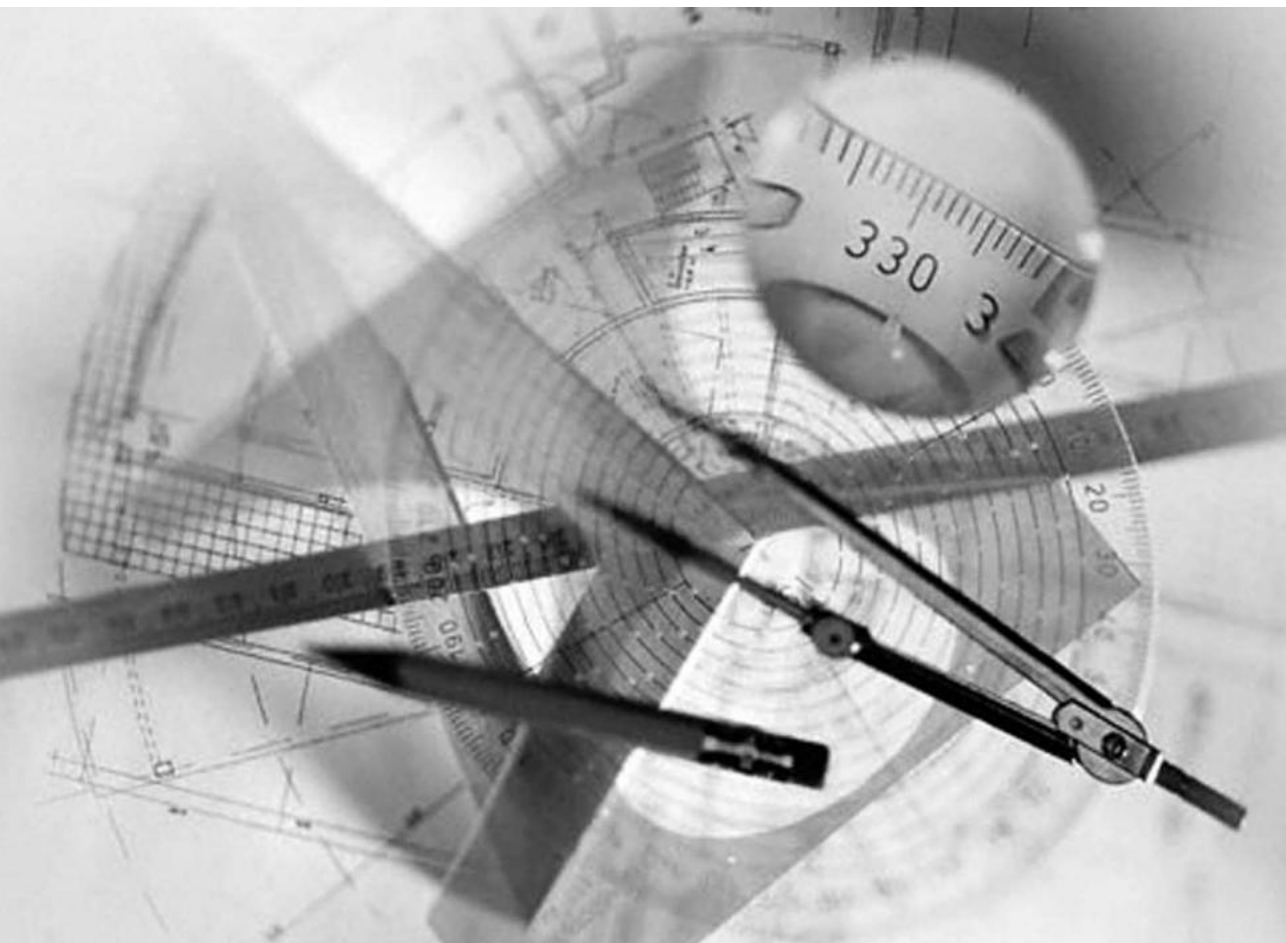
56. Cabral, J. M. & Kennedy, J. F. Covalent and coordination immobilization of proteins. *Bioprocess Technol.* **14**, 73–138 (1991).
57. Waser, R. *Nanoelectronics and Information Technology.* (2012).
58. Brizzolara, R. A. Patterning multiple antibodies on polystyrene. *Biosens. Bioelectron.* **15**, 63–68 (2000).
59. Hammarback, J. A., Palm, S. L., Furcht, L. T. & Letourneau, P. C. Guidance of neurite outgrowth by pathways of substratum-adsorbed laminin. *J. Neurosci. Res.* **13**, 213–220 (1985).
60. Bhatia, S. K., Hickman, J. J. & Ligler, F. S. New approach to producing patterned biomolecular assemblies. *J. Am. Chem. Soc.* **114**, 4432–4433 (1992).
61. Langer, R. & Vacanti, J. P. Tissue engineering. *Science (80-. )*. **260**, 920–926 (1993).
62. Shamansky, L. M., Davis, C. B., Stuart, J. K. & Kuhr, W. G. Immobilization and detection of DNA on microfluidic chips. in *Talanta* **55**, 909–918 (2001).
63. Pandurangi, R. S., Lusiak, P., Desai, S. & Kuntz, R. R. Chemistry of bifunctional photoprobes - 4. Synthesis of the chromogenic, cleavable, water soluble, and heterobifunctional sulfosuccinimidyl (N-methylamino perfluoroaryl azido benzamido)-ethyl-1,3'-dithiopropionate: An efficient protein cross-linking agent. *Bioorg. Chem.* **26**, 201–212 (1998).
64. Liu, L. H. & Yan, M. Perfluorophenyl azides: New applications in surface functionalization and nanomaterial synthesis. *Acc. Chem. Res.* **43**, 1434–1443 (2010).
65. Xia, Y. & Whitesides, G. M. SOFT LITHOGRAPHY. *Annu. Rev. Mater. Sci.* **28**, 153–184 (1998).
66. Kumar, A. & Whitesides, G. M. Features of gold having micrometer to centimeter dimensions can be formed through a combination of stamping with an elastomeric stamp and an alkanethiol “ink” followed by chemical etching. *Appl. Phys. Lett.* **63**, 2002–2004 (1993).
67. Whitesides, G. & Ostuni, E. Soft lithography in biology and biochemistry. *Annu. Rev.* ... (2001). at <<http://www.annualreviews.org/doi/pdf/10.1146/annurev.bioeng.3.1.335>>
68. Perl, A., Reinhoudt, D. N. & Huskens, J. Microcontact Printing: Limitations and Achievements. *Adv. Mater.* **21**, 2257–2268 (2009).
69. Wendeln, C. & Ravoo, B. J. Surface patterning by microcontact chemistry. *Langmuir* **28**, 5527–5538 (2012).

70. Kaufmann, T. & Ravoo, B. J. Stamps, inks and substrates: polymers in microcontact printing. *Polymer Chemistry* **1**, 371 (2010).
71. Bernard, A., Renault, J. P., Michel, B., Bosshard, H. R. & Delamarche, E. Microcontact printing of proteins. *Adv. Mater.* **12**, 1067–1070 (2000).
72. Lee, J. N., Park, C. & Whitesides, G. M. Solvent Compatibility of Poly(dimethylsiloxane)-Based Microfluidic Devices. *Anal. Chem.* **75**, 6544–6554 (2003).
73. Kunzler, J. Silicone hydrogels for contact lens application. *TRENDS Polym. Sci.* **4**, 52–59 (1996).
74. Olander, B., Wirsén, A. & Albertsson, A. C. Oxygen microwave plasma treatment of silicone elastomer: Kinetic behavior and surface composition. *J. Appl. Polym. Sci.* **91**, 4098–4104 (2004).
75. James, C. D. *et al.* Patterned protein layers on solid substrates by thin stamp microcontact printing. *Langmuir* **14**, 741–744 (1998).
76. Mayer, M., Yang, J., Gitlin, I., Gracias, D. H. & Whitesides, G. M. Micropatterned agarose gels for stamping arrays of proteins and gradients of proteins. in *Proteomics* **4**, 2366–2376 (2004).
77. Stevens, M. M. *et al.* Direct patterning of mammalian cells onto porous tissue engineering substrates using agarose stamps. *Biomaterials* **26**, 7636–7641 (2005).
78. Pardo, L., Wilson, W. C. & Boland, T. Characterization of Patterned Self-Assembled Monolayers and Protein Arrays Generated by the Ink-Jet Method †. *Langmuir* **19**, 1462–1466 (2003).
79. Mosbach, M. *et al.* Picodroplet-deposition of enzymes on functionalized self-assembled monolayers as a basis for miniaturized multi-sensor structures. *Biosens. Bioelectron.* **16**, 827–837 (2001).
80. Miller, M. B. & Tang, Y.-W. Basic concepts of microarrays and potential applications in clinical microbiology. *Clin. Microbiol. Rev.* **22**, 611–633 (2009).
81. Romanov, V. *et al.* A critical comparison of protein microarray fabrication technologies. *Analyst* **139**, 1303–1326 (2014).
82. Tasoglu, S. & Demirci, U. Bioprinting for stem cell research. *Trends Biotechnol.* **31**, 10–19 (2015).
83. Piner, R. D. “Dip-Pen” Nanolithography. *Science (80-. )*. **283**, 661–663 (1999).

84. Salaita, K., Wang, Y. & Mirkin, C. A. Applications of dip-pen nanolithography. *Nat. Nanotechnol.* **2**, 145–55 (2007).
85. Lee, K.-B., Park, S.-J., Mirkin, C. A., Smith, J. C. & Mrksich, M. Protein nanoarrays generated by dip-pen nanolithography. *Science* **295**, 1702–5 (2002).
86. Chi, Y. S. & Choi, I. S. Dip-Pen Nanolithography Using the Amide-Coupling Reaction with Interchain Carboxylic Anhydride-Terminated Self-Assembled Monolayers. *Adv. Funct. Mater.* **16**, 1031–1036 (2006).
87. Xu, F. J. *et al.* Spatially well-defined binary brushes of poly(ethylene glycol)s for micropatterning of active proteins on anti-fouling surfaces. *Biosens. Bioelectron.* **24**, 773–780 (2008).
88. Kim, P. *et al.* Fabrication of nanostructures of polyethylene glycol for applications to protein adsorption and cell adhesion. *Nanotechnology* **16**, 2420 (2005).
89. Gingell, D., Owens, N., Hodge, P., Nicholas, C. V & O'Dell, R. Adsorption of a novel fluorescent derivative of a poly(ethylene oxide)/poly(butylene oxide) block copolymer on octadecyl glass studied by total internal reflection fluorescence and interferometry. *J. Biomed. Mater. Res.* **28**, 505–513 (1994).
90. Malmsten, M., Emoto, K. & Van Alstine, J. M. Effect of Chain Density on Inhibition of Protein Adsorption by Poly(ethylene glycol) Based Coatings. *J. Colloid Interface Sci.* **202**, 507–517 (1998).
91. Jo, S. & Park, K. Surface modification using silanated poly(ethylene glycol)s. *Biomaterials* **21**, 605–616 (2000).
92. Kirby, B. J., Wheeler, A. R., Zare, R. N., Fruetel, J. A. & Shepodd, T. J. Programmable modification of cell adhesion and zeta potential in silica microchips. *Lab Chip* **3**, 5–10 (2003).
93. Ostuni, E., Grzybowski, B. A., Mrksich, M., Roberts, C. S. & Whitesides, G. M. Adsorption of proteins to hydrophobic sites on mixed self-assembled monolayers. *Langmuir* **19**, 1861–1872 (2003).
94. Andrade, J. D. & Hlady, V. in *Biopolymers/Non-Exclusion HPLC* **79**, 1–63 (1986).
95. Kwon, S., Kim, H., Ha, J.-W. & Lee, S.-Y. Prevention of protein and polymeric nanoparticles adsorption using perfluoropolyether. *J. Ind. Eng. Chem.* **17**, 259–263 (2011).
96. Hu, Z. *et al.* Optically Transparent, Amphiphilic Networks Based on Blends of Perfluoropolyethers and Poly(ethylene glycol). *J. Am. Chem. Soc.* **130**, 14244–14252 (2008).

97. Yarbrough, J. C. *et al.* Contact Angle Analysis, Surface Dynamics, and Biofouling Characteristics of Cross-Linkable, Random Perfluoropolyether-Based Graft Terpolymers. *Macromolecules* **39**, 2521–2528 (2006).
98. Rolland, J. P., Van Dam, R. M., Schorzman, D. A., Quake, S. R. & DeSimone, J. M. Solvent-Resistant Photocurable “Liquid Teflon” for Microfluidic Device Fabrication. *J. Am. Chem. Soc.* **126**, 2322–2323 (2004).
99. Wang, Y. *et al.* Photocurable Amphiphilic Perfluoropolyether/Poly(ethylene glycol) Networks for Fouling-Release Coatings. *Macromolecules* **44**, 878–885 (2011).
100. Bajpai, A. K. Blood protein adsorption onto a polymeric biomaterial of polyethylene glycol and poly[(2-hydroxyethyl methacrylate)-co-acrylonitrile] and evaluation of in vitro blood compatibility. *Polym. Int.* **54**, 304–315 (2005).
101. Baier, R. E., Depalma, V. A., Goupil, D. W. & Cohen, E. Human platelet spreading on substrata of known surface chemistry. *J. Biomed. Mater. Res.* **19**, 1157–1167 (1985).
102. Kendall, K. The adhesion and surface energy of elastic solids. *J. Phys. D. Appl. Phys.* **4**, 1186–1195 (1971).
103. Brady, R. F. A fracture mechanical analysis of fouling release from nontoxic antifouling coatings. *Prog. Org. Coatings* **43**, 188–192 (2001).
104. Magin, C. M., Cooper, S. P. & Brennan, A. B. Non-toxic antifouling strategies. *Mater. Today* **13**, 36–44 (2010).
105. Hu, Z. Novel Perfluoropolyethers as Fouling-Release Coatings. (University of North Carolina, 2009).
106. Gudipati, C. S., Finlay, J. A., Callow, J. A., Callow, M. E. & Wooley, K. L. The antifouling and fouling-release performance of hyperbranched fluoropolymer (HBFP)-poly(ethylene glycol) (PEG) composite coatings evaluated by adsorption of biomacromolecules and the green fouling alga ulva. *Langmuir* **21**, 3044–3053 (2005).

### **3.** **Aim of the work**



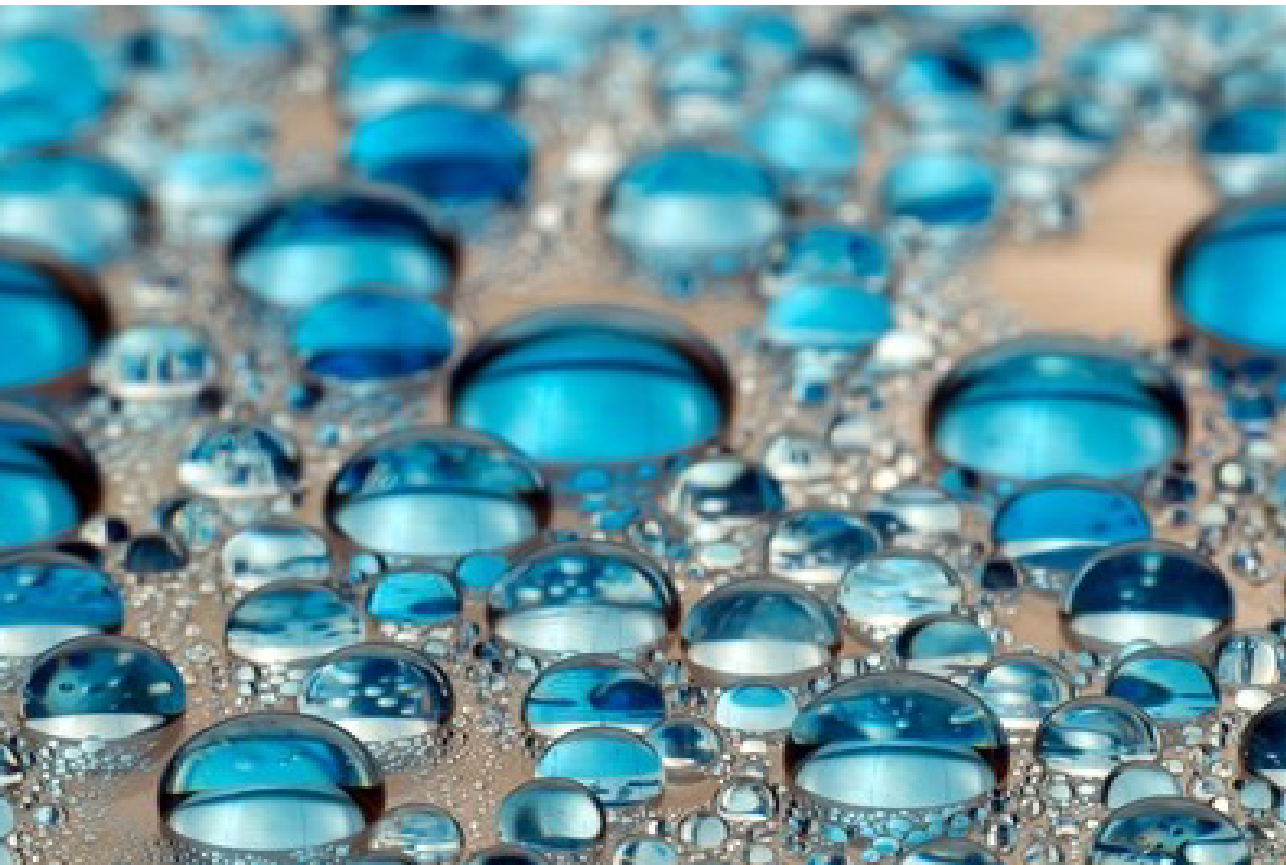
The main objective of the first part of the present thesis is the development and validation of **3D synthetic matrices for the osteo-chondral tissue engineering** where around 12% of the wounded population could be treated using autologous-engineered substitutes, as alternative to standard graft procedures, which are affected by limited supply and possible immune rejection. The strategy involves the fabrication and functionalization of advanced experimental 3D scaffolds, which are engineered to enable **independently tuning their physico-mechanical properties**, in terms of scaffold geometry and surface stiffness. Therefore, they could enable **disentangling and investigating the specific role that each stimulus** has on the commitment of bone marrow stem cells towards the osteo-chondral lineage. Nowadays, **3D freestanding scaffolds with tailored geometry** can be fabricated by **two-photon polymerization (2PP)**, which allows rapid prototyping of 3D complex polymer structures thus enabling the transition from 2D to 3D cell culture techniques in vitro. In order to **widen the range of the mechanical properties** of the 2PP structures in contact with the cells, we focus on **hydrogels** as potentially biomimetic materials **suitably for 2PP scaffold coating** because of their biocompatibility and bioactivity. Moreover, hydrogels chemical and mechanical properties can be processed via **cross-linking and conjugation reactions**, thus offering the possibility to fine-tune their mechanical and chemical properties. Different chemical and photochemical cross-linked **hyaluronic acid-** and **gelatin-based** hydrogels are studied and we aim to understand how to keep control over the cross-linking processes in order to **synthesize hydrogels with tailored stiffness**. Subsequently, **immobilization strategies based on physical, chemical and photochemical interactions** could be explored to efficiently functionalize 2PP structures with a thin layer of hydrogels without affecting the overall porosity.

The second part of the present research concerns the field of **biomolecular patterning** and the main goal was the design and realization of **patterned functional surfaces for rare cell capture and isolation**. Currently, biomolecular

patterning is considered one of the key technologies for the realization of living-cell arrays and for the **study of specific individual cellular processes**. Among all the different kinds of proper chemicals, derivatives of **hyaluronic acid** and **heparin** were first chosen as baits due to their preferential interactions with **cancer cells and malaria-infected red blood cells (pRBCs)** respectively. Particularly, HA is involved in tumor growth and metastasis, while heparin is able to bind to the protein domain expressed by malaria-infected erythrocytes. The availability of HA or heparin in well-defined positions may open several perspectives in the field of devices for molecular biology and nanomedicine. It is possible to exploit their affinity with cancer cells and pRBCs to immobilize them and to make them available for specific tests and experiments thus encouraging the discovery and formulation of new drugs and therapies. A fundamental issue in the development of these cell capture microdevices is represented by **material selection** that deeply affects the selective sorting efficiency of the final array, hence a **deep characterization** is required. To this end, our first aim is to **compare different perfluoropolyether (PFPE)**-based materials, considered promising as protein adhesion resistant substrates, to highlight the possible **relationship between their main structural parameters and their protein resistance behavior** and to select the high performing antifouling PFPE material. The second goal is the **identification of the simplest and most effective patterning technology** to selectively functionalize PFPE substrates. For this purpose both photolithography and soft-lithography could be employed and **different immobilization chemistries**, including photografting and biomolecular recognition, **were explored** to find the best solution to efficiently graft HA and heparin.



## 4. Hydrogel synthesis and fine tuning of mechanical properties



## 4.1 Introduction

Adult stem cells (SCs) are specialized and essential for tissue maintenance and repair<sup>1</sup>. In the body, SCs reside within instructive tissue specific niches, which regulate SCs fate providing proper chemical and mechanical stimuli. Consequently, mimicking such tridimensional environment in vitro is the main goal of regenerative medicine and is challenging to understand the role of each specific aspect in affecting SCs differentiation. Actually, the most promising strategy involves seeding SCs on a scaffold, an interim synthetic extracellular matrix, culturing them giving proper cues until maturation into a functional tissue ready to be transplanted in an injured patient. The key element is the scaffold that must be engineered to provide and maintain a micro- and nanostructured three-dimensional (3D) environment until the SCs have built their own connective tissue. Moreover, recent studies revealed the fundamental effect that mechanical properties of the artificial in vitro environment have on many aspects of cell functions including adhesion, migration, proliferation<sup>2,3</sup> and on differentiation<sup>3</sup>. In particular, after several weeks in culture, mesenchymal stem cells (MSCs) are proved to commit to the lineage specified by the substrate stiffness they sense which measure the resistance that a cell feels when deforming the extracellular matrix (ECM). The elastic constant  $E$  of the matrix also best represents the matrix of the tissue they derive; e.g. soft matrices ( $0.1 \div 1$  kPa) are neurogenic, stiffer matrices ( $8 \div 17$  kPa) are myogenic and rigid matrices ( $10 \div 40$  kPa) are osteogenic<sup>4</sup>. Therefore, it is of great interest to functionalize scaffold surfaces with suitable coating materials whose mechanical properties could be finely tuned, in order to vary substrate stiffness encompassing the physiological values of the specific tissue needed for transplantation. Due to their many favorable and biomimetic properties, hydrogels have been increasingly recognized as challenging biomaterials and have gained considerable attention in such biomedical engineering applications<sup>5-8</sup>. They can be chemically or physically modified under mild biocompatible conditions to exhibit specific cell-material interactions<sup>9</sup>, furthermore, they can be

designed to have elastic moduli similar to those of soft tissue.

Among hydrogels, we focused on hyaluronic acid (HA), a well known linear polysaccharide composed of long chains of repeating disaccharide units of N-acetyl-D-glucosamine (GlcNAc) and D-glucuronic acid (GlcA) linked by  $\beta$  1-4 glycosidic bond<sup>10</sup>. Physiologically present in the human body, its highest occurrence is in the extracellular matrix (ECM) of human connective tissue especially in the synovial fluid of joints, in the brain, in the dermis of the skin and in the vitreous body of the eye. Moreover, in physiological conditions HA is negatively charged and highly hydrophilic, surrounded by a sphere of water molecules linked by hydrogen bonds. Its strong hydrophilic character together with its high molecular weight values ( $10^5$  Da in serum to  $10^7$  Da in vitreous<sup>11</sup>), give to HA both structural and functional roles in the body. Being a hydrogel based on naturally occurring carbohydrates, HA even offers the inherent advantages of being biocompatible and biodegradable by a complex enzymatic mechanism involving hyaluronidase enzymes<sup>12</sup>. Finally, to improve its mechanical properties, to control the degradation rate and to prevent its rapid re-dissolution in water, HA can be chemically modified with cross-linking or conjunction reactions<sup>13-16</sup>. Therefore HA is an appropriate biomaterial to be exploited as scaffold coating material with graded elasticity to reproduce mechanical substrate properties of native stem cell niches environment. In the present work, we aim to establish a simple, reliable and controlled methodology for the preparation and characterization of HA hydrogels encompassing the range of physiologically osteo-chondral relevant moduli. To this end, a homogeneous crosslinking process was first optimized to obtain biocompatible chemical hydrogels using divinyl sulfone (DVS), highly reactive and efficient cross-linker, that creates ether linkages between HA primary hydroxyl groups<sup>9,17</sup>. Different HA cross-linking conditions process were tested in terms of cross-linking density (HA:DVS stoichiometric ratio) and cross-linking conditions (reaction time and temperature). As a minor, biocompatible photocrosslinkable hydrogels were obtained by HA linking with glycidyl methacrylate (GMHA) and UV-exposing in the presence of a photoinitiator. An in-depth mechanical

characterization process based on three different techniques was optimized and implemented to determine if hydrogels properties suit for osteo-chondral tissue engineering application. HA:DVS mechanical properties were studied on macroscopic samples by dynamic rheological analysis with measurements of dynamic moduli and estimation of density of cross-linking. Rheological results were successively benchmarked with swelling experiments following the Flory-Rehner theory<sup>18</sup>, applied also to the GMHA hydrogel samples, and by atomic force microscopy (AFM) nanoindentation, which are experimental techniques much more suitable for the investigation of local mechanical properties of small-scale hydrogel samples as typically those coated onto scaffolds<sup>19</sup>. The final goal is to keep control over the cross-linking process and to prepare HA hydrogels with tailored mechanical properties suitable as coating material for scaffold used to recreate osteo-chondral niches environment in vitro. It is also of great interest for our scope, the implementation and validation of swelling experiments and AFM analyses as characterization techniques that give the possibility to directly evaluate the mechanical properties of functionalized microscaffolds without altering the sample.

## 4.2 Experimental section

### 4.2.1 Materials

Hyaluronic acid sodium salt ( $M_w$   $1.6 \times 10^6$  g/mol) obtained by fermentation of *Streptococcus equi* bacteria - bacterial glycosaminoglycan polysaccharide; divinyl sulfone (DVS), sodium hydroxide (NaOH), glycidyl methacrylate, triethylamine, N-vinyl pyrrolidone (VP) and 1H,1H,2H,2H perfluorodecyltriethoxysilane (PFDTES, 97%) were all purchased from Sigma-Aldrich. Photoinitiator 2-Hydroxy-1-[4-(2-hydroxyethoxy) phenyl]-2-methyl-1-propanone, commercial name Irgacure 2959, was bought from Ciba Specialty Chemicals. All the reagents were used without any purification.

### 4.2.2 Hydrogels synthesis and functionalization

Hyaluronic acid (HA) hydrogels were prepared exploiting both chemical and photochemical crosslinking methods.

#### 4.2.2.1 Hyaluronic acid (HA) chemical hydrogels

Powdered Hyaluronic acid sodium salt (NaHA,  $1.6 \times 10^6$  g/mol) was chemically cross-linked using a homogeneous method based on previously protocols<sup>20</sup>, and involving addition of the cross-linking agent directly into the HA solution. Briefly, powdered HA was dissolved in alkaline solution (3% w/v, 0.2M NaOH, pH13) and divinyl sulfone (DVS) was added dropwise with three different HA:DVS molar ratio (1:2; 1:5 and 1:10 with respect to HA primary hydroxyls). The mixture was poured in a 50-mm Petri dish, after stirring it for 4 minutes in a closed vial to allow DVS uniform diffusion without its uncontrolled evaporation. The reaction was allowed to proceed at 4°C and the gels were cross-linked at different reaction times (2h; 12h and 96h). Both DVS-content and reaction time were varied in order to study the impact of these parameters on hydrogels mechanical properties (for brevity, these hydrogels will be referred to as HA:DVS from here on). Each sample, representative of one cross-linking parameters combination,

was prepared thrice. At the end of the curing processes, the gels were poured in excess of water and washed several times in phosphate-buffered saline (PBS) to end the cross-linking reaction and to remove the potentially cytotoxic unreacted DVS. The hydrogels were finally swollen at their equilibrium value for three days in a large excess of distilled water.

#### 4.2.2.2 HA hydrogels biocompatibility tests

Cell tests were performed at the Laboratory of Biological Structures Mechanics (LaBS) to assess hydrogels biocompatibility. Round-shape cover slip glasses ( $\Phi = 12\text{mm}$ , BioOptoka, Milano, Italy) were covered with a thin film of HA:DVS hydrogels 1:10, with the highest DVS-content. MG63 human osteosarcoma cells (86051601-1VL, Sigma-Aldrich) were first resuscitated and expanded in minimum essential medium (MEM) supplemented with 2mM glutamine, 10% fetal calf serum (FCS), 1% non-essential amino acids (NEAAs), and 1% penicillin/streptomycin. Cells were cultured in standard flask until semi-confluence under 5% CO<sub>2</sub> atmosphere at 37°C.

After cells trypsinization and counting, they were seeded and cultured for 4 days on HA:DVS coated glass slide and on a bare glass slide taken as control. Prior to cell seeding, samples were positioned in a 24 multi-well plates (costar 3473, Corning) and UV-sterilized. Cells viability was assessed by the ethidium/calcein colorimetric assay used to verify the membrane integrity. The cellularized samples were marked using a live/dead kit (L3224, Invitrogen-Molecular Probes), in which the polyanionic dye calcein is retained within live cells producing green fluorescence, and ethidium homodimer-1 (EthD-1) enters cells with damaged membranes and binds to nucleic acids, producing a red fluorescence. The samples were incubated in 2  $\mu\text{M}$  calcein and 4  $\mu\text{M}$  EthD-1 solutions for 45 min. Images were acquired using an inverted phase contrast/fluorescence microscope (IX70, Olympus).

### 4.2.2.3 Synthesis and photochemical cross-linking of Glycidyl Methacrylated-hyaluronic acid (GMHA) hydrogels

Photocrosslinkable hydrogels were synthesized functionalizing HA chains with methacrylate groups exploiting the simple and fast reaction with glycidyl methacrylate deeply described by several authors<sup>15,21,22</sup>. HA solution (1% w/v in distilled water) was reacted at room temperature for 24 h with a 20-fold molar excess of glycidyl methacrylate in the presence of 20-fold molar excess of triethylamine acting as a catalyst. The reaction was allowed to proceed for 24 hours. Then the solution was precipitated twice in acetone (20 times the volume of the reaction solution) and dissolved in distilled water in order to remove excess reactants. The GMHA solution was frozen, lyophilized for 48-72 h (VirTisBenchTop Freeze dryer 2K, 40÷50mTorr) and stored desiccated in the dark at -20°C.

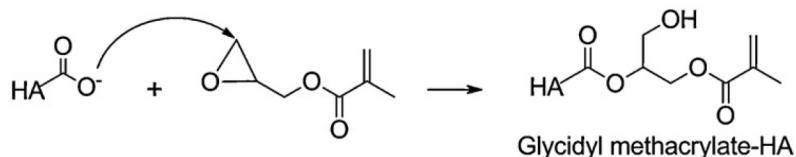


Figure 1. Hyaluronic acid esterification with glycidyl methacrylate.

Proton nuclear Magnetic Resonance (<sup>1</sup>H-NMR) spectroscopy analyses were performed on GMHA conjugates in order to verify the efficiency of methacrylic functionalization<sup>21</sup>. Deuterium oxide (D<sub>2</sub>O) was used as solvent, and the polymer concentration was 1% by mass fraction. <sup>1</sup>H-NMR was also used to determine the methacrylation conversion or degree (DM) on modified HA. The DM is defined as the amount of methacryloyl groups per one HA disaccharide repeat unit and was calculated from the ratio of the relative peak integrations of the methacrylate protons (peaks at ~6.1, ~5.6, and ~1.9 ppm according with literature) and HA's methyl protons (~1.9 ppm)<sup>15</sup>. Following this strategy GMHA could be synthesized at different methacrylation degrees in order to tune its mechanical properties.

The resultant HA derivatives were converted into elastic hydrogels by radical polymerization, exposing GMHA solution (0.2% w/v in PBS) to UV-light ( $\lambda = 365$  nm, 4 mW/cm<sup>2</sup> MF 1030, Nuova Delta Elettronica) for 10 minutes in nitrogen

atmosphere in the presence of the photoinitiator 4-(2-hydroxyethoxy)phenyl-(2-hydroxy-2-propyl)ketone (1.5% w/v, marketed as Irgacure 2959) and N-vinyl pyrrolidone (VP; 1.5% v/v), acting as reactive co-monomer as well as solvent for the photoinitiator otherwise insoluble in GMHA solution. GMHA concentration, photoinitiator and co-monomer content were chosen according to literature to tailor the properties of the resultant networks and to obtain hydrogels with elastic moduli closely approximating those of physiological values.

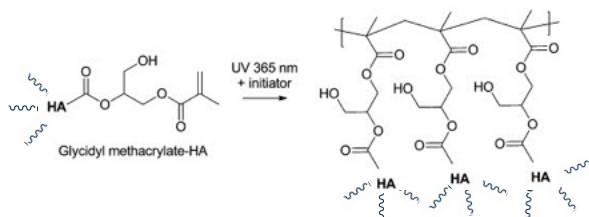


Figure 2. GMHA photo cross-linking scheme.

### 4.2.3 Physical characterization

HA:DVS hydrogel mechanical properties were studied on macroscopic samples by dynamic rheological measurements with measurements of dynamic moduli and estimation of density of crosslinking. Rheological results were successively benchmarked with swelling experiments following the Flory-Rehner theory<sup>18</sup>, and by Atomic Force Microscopy (AFM) nanoindentation which are experimental techniques much more suitable for the investigation of small-scale hydrogel samples as typically those coated onto scaffolds. Further swelling experiments were conducted on the GMHA photocross-linked samples.

#### 4.2.3.1 Rheological measurements

Storage ( $G'$ ) and loss ( $G''$ ) moduli of hydrogels were measured using a Rheometrics Dynamic Stress Rheometer 200 operating under a 25 mm parallel-plate configuration and a 1.5 mm plate spacing. After preliminary stress sweep experiments to identify the linear viscoelastic range of the hydrogels, isothermal

frequency sweep tests were performed considering a frequency range from 0.01 to 1 Hz. The rubber elasticity theory was exploited to estimate both the Young's modulus  $E$ , assuming a Poisson's ratio  $\nu$  of 0.5<sup>2</sup> and the crosslink density  $\nu_{RH}$  of the hydrogel networks according to the following relationships:

$$E = 2G' (1 + \nu) \text{ Equation 1}$$

$$\nu_{RH} = \frac{G'}{RT} \text{ Equation 2}$$

where  $G'$  is the plateau storage modulus,  $R$  is the gas constant (8.314 J mol<sup>-1</sup>K<sup>-1</sup>) and  $T$  is the temperature at which the modulus was measured (310.15 K).

#### 4.2.3.2 Swelling measurements and Flory-Rehner calculations

##### 4.2.3.2.1 Theoretical Background

Chemically cross-linked hydrogels are three-dimensional covalent networks able to absorb a large amount of water. An equilibrium swelling value is reached as a compromise between the random coil expansion in good solvent, and the entropic-elastic retraction force. Flory<sup>18</sup> first described the thermodynamics of swollen polymer networks considering that the free energy change ( $\Delta G$ ) involved in swelling experiments consisted of two parts:

$$\Delta G = \Delta G_{el} + \Delta G_m \text{ Equation 3}$$

where the elastic free energy  $\Delta G_{el}$  is related to entropic elasticity and the free energy of mixing  $\Delta G_m$  concerns polymer-solvent interactions. According to the molecular theory of rubber elasticity, the  $\Delta G_{el}$  is due to the change in chain conformations, which lead to an entropy variation. Considering an isotropic extension during swelling and being  $\nu_2$  is the volume fraction of polymer component in the swollen gel, the following equation is obtained:

$$\Delta G_{1,el} = \frac{\rho RT}{\bar{M}_c} V_1 v_2^{1/3} \text{ Equation 4}$$

Where  $n_1$  and  $V_1$  are respectively the mole fraction and the molar volume of the solvent. As far as the free energy of mixing  $\Delta G_m$  is concerned, the final Flory - Huggins equation for the molar free energy of mixing is:

$$\Delta G_{1,m} = RT \left( \ln(1 - v_2) + \left(1 - \frac{1}{x}\right) v_2 + \chi v_2^2 \right) \text{ Equation 5}$$

Where  $\chi$  is the Flory polymer-solvent interaction parameter. At the swelling equilibrium  $\Delta G_1 = \Delta G_{1,el} + \Delta G_{1,m} = 0$ , therefore:

$$\ln(1 - v_{2e}) + v_{2e} + \chi v_{2e}^2 + \frac{\rho V_1}{\bar{M}_c} v_{2e}^{1/3} = 0 \text{ Equation 6}$$

where subscript  $e$  indicates the maximum, or equilibrium, swelling.

Generally,  $q$  is used to indicate the swelling ratio and it is equal to  $V/V_0$  and so, at the equilibrium,  $q_e = 1/v_{2e}$ . If we solve the latter equations for  $v_{2e} = 1/q_m$ , assuming that we are at low degree of cross-linking and with good solvent ( $q_m > 10$ ), a simplified relationship is obtained highlighting the dependence of the equilibrium swelling ratio on the thermodynamic quality of solvent ( $\chi$ ):

$$q_e^{5/3} \cong \frac{\bar{M}_c}{\rho V_1} \left( \frac{1}{2} - \chi \right) \text{ Equation 7}$$

#### 4.2.3.2.2 Thermogravimetric (TGA) analyses

Swelling experiments were conducted to measure the degree of mass swelling  $q_m$  of both chemically and photochemically cross-linked HA hydrogels. Such parameter is strictly correlated to the mechanical strength of cross-linked networks and to their density of cross-linking (§4.2.3.2.1)<sup>23</sup>. Particularly,  $q_m$  was calculated as  $W_s/W_d$  which are respectively the weight of the equilibrium-

swollen gel sample ( $W_s$ ) and of the dried sample ( $W_d$ ), and both were measured using a Q500 (TA Instrument) thermogravimetric analyzer (TGA). A small swollen piece of HA hydrogel, corresponding to  $W_s$  (40 ÷ 50 mg), was placed in the TGA weighing pan and slowly heated at 50°C fixed-temperature until a constant mass, corresponding to  $W_d$ , was achieved. In order to assess the cross-link density  $\nu_{FR} = \rho_p / \bar{M}_c$ ,  $M_c$  which is the average molecular weight between cross-links, was first calculate by applying the Equation 7. This represents an approximate expression of the Flory-Rehner equation that is valid for networks with low degrees of cross-linking swollen in good solvent and where in our experimental conditions:

- $V_1$  which is the molar volume of the solvent was 18 cm<sup>3</sup>/mol (water);
- $\rho_p$  which is the density of the dry polymer was 1.229 g/cm<sup>3</sup>;
- $\chi$  which is the Flory polymer-solvent interaction parameter, was estimated to be 0.473 for HA in water based on the assumption that HA is comparable to that for dextran, a well-studied polysaccharide with HA similar chemical structures<sup>21,24</sup>;
- $q_e$  is the volumetric swelling ratio determined from  $q_M$ <sup>25</sup>:

$$q_e = 1 + \frac{\rho_p}{\rho_s} (q_M - 1) \text{ Equation 8}$$

with  $\rho_s$  is the density of the solvent which is water in our case.

#### 4.2.3.3 AFM nanoscale indentation

AFM nanoindentation experiments were performed for a highly spatially resolved mechanical testing of the equilibrium-swollen HA:DVS hydrogels<sup>26</sup>. Particularly, were tested two types of samples obtained with two different DVS-content (1:5 and 1:10) and same reaction time (12h), which were supported over a glass microscope slide. Since the swelled hydrogel must remain hydrated, all the samples were indented just after the hydration process, keeping a constant relative humidity of 50% to minimize hydrogel water loss, which can significantly influence their mechanical behavior<sup>23</sup>.

Every force-distance curve was obtained in air by means of an NSCRIPTOR™

atomic force microscope (NanoInk, Inc., Skokie, IL) in a controlled atmosphere chamber ( $T = 23^{\circ}\text{C}$ ). The NSCRIPTOR<sup>TM</sup> instrument is provided with a closed-loop correction, which consists in a piezo scanner fitted with a secondary monitoring system that has its own feedback loop. This allows the closed-loop scanner to perform with a high degree of linearity. In addition, to correct time-independent non-linearity of the scanner, before any experimental round, a linearization procedure available in the SPM Cockpit software was carried out, determining the optimum linear range of the x-y feedback sensors (x-y area in which the scanner is currently linear).

A colloidal probe (series HYDRA6R-200NG-COLL, AppNano, Santa Clara, CA, USA) with a nominal spring constant  $k_c = 0.035 \text{ N/m}$  and a spherical glass tip was used in all measurements after its silanization in air with perfluorodecyltriethoxysilane ( $100^{\circ}\text{C}$  for 16h in a sealed vial) to make the tip hydrophobic and to reduce the tip-gel adhesion phenomenon. All the nanoindentation curves were dynamically acquired with an indentation rate of 0.05 Hz and evaluated using the Cockpit<sup>®</sup> software. The maximum force applied onto the hydrogel surface was  $14.7 \pm 3.1 \text{ nN}$ . In order to convert the cantilever deflection signal from mV (force-displacement) to nm (force-indentation), the deflection sensitivity of the instrument and so the sensitivity of the probe was calculated from calibration by applying a load on a substrate (a piranha-cleaned Si surface) assumed to be an infinitely rigid substrate (zero indentation). At least 20 nanoindentation curves were collected for each samples and results were averaged.

Fitting of the raw AFM curves was carried out by means of OriginPro 8.5 software and the quality of the fitting was evaluated in terms of coefficient of determination  $R^2$ . For the fitting, all the datasets were firstly restricted so that the maximum penetration depth of the tip into the sample was acceptable for the mathematical model subsequently exploited to determine the elastic modulus  $E$ , this implies that the maximum penetration depth should be comparable to the tip radius. The datasets were then limited to the beginning of the experimental range in order to consider not only the elastic part of deformations but also a range of indentation slower than 0.1% of

sample thickness. This prevented the stiffness of substrates from affecting modulus measurements of samples. The datasets were lastly selected from a statistical point of view. The adjusted  $R^2$  coefficient was compared for different datasets in order to select a dataset with an adjusted  $R^2$  value higher than 0.99.

The elastic modulus  $E$  was determined by fitting the Johnson-Kendall-Roberts (JKR) mathematical model (Eq.14) with experimental data together with the geometrical features of the calibrated tip<sup>27</sup>.

Table 1. AFM tip dimensions and indentation depth

	<b>Tip Radius <math>R</math></b> <b>[<math>\mu\text{m}</math>]</b>	<b>Indentation Depth <math>\delta</math></b> <b>[<math>\text{nm}</math>]</b>
<b>Fwd</b>	2.5 ÷ 4.5	638 ± 55
<b>Rev</b>	2.5 ÷ 4.5	335 ± 66

The JKR model, derived from the classical Hertzian relation<sup>28</sup>, is suitable for spherical tip and soft sample with large adhesion force and it predicts that the contact radius  $a$  between the tip and the sample and the elastic indentation depth  $\delta$  are given by:

$$\delta = \frac{a^2}{R} - \frac{4}{3} \sqrt{\frac{aF_{ad}}{RE_{tot}}} \quad \text{Equation 9}$$

$$a = \left[ \frac{R}{E_{tot}} \left( \sqrt{F_{ad}} + \sqrt{F + F_{ad}} \right)^2 \right]^{1/3} \quad \text{Equation 10}$$

where  $R$  is the tip radius (2.5 ÷ 4.5 mm),  $F_{ad}$  the pull-off force between the tip and the hydrogel surface,  $F$  the applied force and  $E_{tot}$  the reduced modulus. Considering  $E_s$ ,  $\nu_s$  and  $E_t$ ,  $\nu_t$  the Young's moduli and the Poisson's ratios for the sample and the tip respectively, the reduced modulus is defined as:

$$\frac{1}{E_{tot}} = \frac{3}{4} \left( \frac{(1-\nu_s^2)}{E_s} + \frac{(1-\nu_t^2)}{E_t} \right) \quad \text{Equation 11}$$

Then, assuming the tip infinitely stiff and neglecting its deformation, Eq.11

simplified to:

$$\frac{1}{E_{tot}} = \frac{3}{4} \left( \frac{(1-\nu_s^2)}{E_s} \right) \text{ Equation 12}$$

The Young's modulus of the sample can also be expressed by the following equation using the JKR model:

$$E_{tot} = \frac{9}{4} (1 - \nu_s^2) R F_{ad} \sqrt{\left( \frac{\left( \left( 3 \sqrt{\frac{\Delta d}{\Delta d_{ad}}} + 1 - 1 \right) \left( \frac{1}{9} \left( \left( \sqrt{\frac{\Delta d}{\Delta d_{ad}}} + 1 \right) + 1 \right) \right)^{1/3} \right)^3}{3R\delta} \right)} \text{ Equation 13}$$

where  $\Delta d$  is the range of cantilever deflection considered in the contact part of the force curve for calculating the modulus and  $\Delta d_{ad}$  the pull-off cantilever deflection in the withdrawn curve.

For all measurements  $\nu_s$  was assumed to be 0.5<sup>29</sup>. According to the JKR theory, the location of the point of zero indentation is established from the force curve where the applied force  $F = - (8/9) F_{ad}$ , as obtained by setting  $\delta = 0$  in the Eq.9, substituting the definition of contact radius given by Eq.10 and solving for  $F$ <sup>30</sup>.

Young moduli  $E_{AFM}$  obtained with nanoindentation were compared with  $E_{RH}$  values derived from rheological measurements taking into account that the two analyses were performed at different temperature, parameter affecting the mechanical behavior of rubbery materials.  $E_{RH}$  (23°C) was therefore calculated fitting Eq.1 with  $G' = \nu_{RH}RT$  where  $T = 296.15$  K and  $\nu_{RH}$  the cross-linking density previously estimated with Eq.2.

## 4.3 Results and discussion

### 4.3.1 Hydrogels chemical and photochemical cross-linking

Hyaluronic acid hydrogels were prepared exploiting both chemical and photochemical crosslinking. Experience<sup>31,32</sup> has shown that enhancing the repeatability of reported experimental cross-linking procedures and their outcomes, requires paying attention to the procedures concerning HA solution preparation and HA mixing with cross-linking agents.

Chemically cross-linked hydrogels were prepared by adding divinyl sulfone as cross-linking agent directly in the HA aqueous solution (3% w/v). In order to avoid DVS evaporation and irreproducibility of results due to not homogeneously cross-linked hydrogels, the reaction was allowed to proceed at low temperature ( $\approx +4^{\circ}\text{C}$ ) in closed vials. A total of nine hydrogels were prepared varying cross-linking agent content and curing time, and from here on samples will be addressed/named as indicated in Table 2. In the acronyms HA3%<sub>x,y</sub>, HA3% refers to the HA solution concentration (3% w/v), x refers to HA:DVS ratio and y to the curing time.

Table 2. Summary of hydrogels samples prepared with all the possible combinations for HA:DVS stoichiometric ratios (column 2) and reaction times considered (column 3).

<i>Sample</i>	<i>HA : DVS</i>	<i>t<sub>ret</sub> [h]</i>
HA_1/2_2h	1:2	2
HA_1/2_12h	1:2	12
HA_1/2_96h	1:2	96
HA_1/5_2h	1:5	2
HA_1/5_12h	1:5	12
HA_1/5_96h	1:5	96
HA_1/10_2h	1:10	2
HA_1/10_12h	1:10	12
HA_1/10_96h	1:10	96

Instead, photo cross-linked hydrogels were synthesized by exposing Glycidyl methacrylated-hyaluronic acid (GMHA) to UV-light in the presence of the photoinitiator Irgacure 2959 and N-vinyl pyrrolidinone (a reaction accelerant

and comonomer). GMHA was synthesized as previously described, exploiting the simple and fast reaction with glycidyl methacrylate which probably reacts with a nucleophilic site on HA by a reversible trans-esterification through the primary hydroxyl group and an irreversible ring-opening conjugation through the carboxylic acid group toward the highest substituted carbon of epoxide<sup>15,33</sup>. An excess of GM with respect to HA was used because of the slight solubility and hydrolysis of GM in aqueous medium. <sup>1</sup>H-NMR spectroscopy was implemented on the GMHA purified product to confirm the presence of methacrylate functionality in the polysaccharide. Compared to native HA<sup>21</sup>, the <sup>1</sup>H-NMR spectrum collected from modified HA (Fig.3) showed two peaks in the range of 5.2 ÷ 5.7 ppm which are attributable to the presence of vinyl-carbon linked hydrogen by glycidyl methacrylate addition. The peaks offset, compared to data from literature, is probably due to the relative pH of the solution that could trigger a subtle change in shielding.

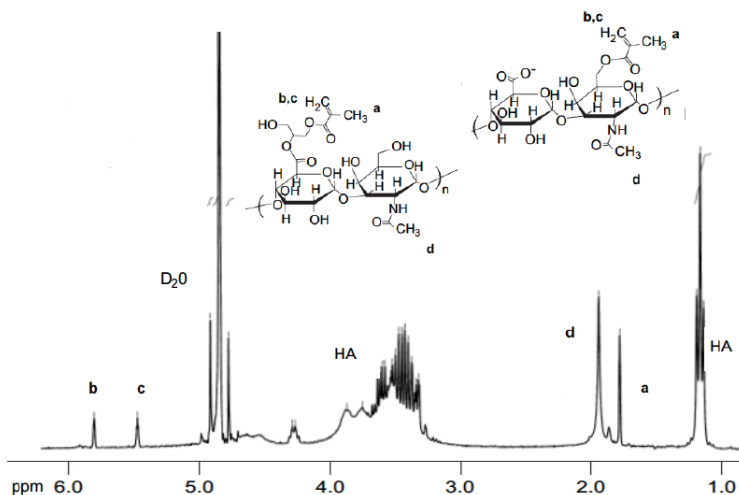


Figure 3. <sup>1</sup>H-NMR spectrum of modified HA dissolved in D<sub>2</sub>O.

The primary peaks in the spectrum including one at 1.2 ppm and the complicated splitting in the range 3.2 ÷ 3.8 ppm are all indicative of the native HA structure<sup>34</sup>. Some additional peaks in the range of 4.7 ÷ 5 ppm could be residual D<sub>2</sub>O solvent from the lyophilization. Methacrylation percentage of HA was determined by

integrating the methyl peak at  $\sim 1.9$  ppm and the acrylic double bond peaks and the results suggested approximately 10% modification. Increasing the DM or the concentrations of GMHA, I2959 or VP yielded gels with increased firmness. However, in the present work, these parameters were fixed according to literature and GMHA hydrogels were obtained from a 0.2% w/v GMHA solution doped with 1.5% w/v of photoinitiator and 1.5 v/v of VP co-monomer.

### 4.3.2 HA biocompatibility

In order to verify the HA:DVS cross-linked hydrogels biocompatibility, even in excess of potentially cytotoxic DVS, tests were performed seeding and incubating osteosarcoma cells on thin hydrogels coating for 4 days. MG-63 cell viability was evaluated by performing a fluorescence live/dead assay, in which live cells stain green and dead cells stain red. As shown in Figure 3a and 3b, cells cultured on bare glass are all viable and well anchored to the substrate and proliferated rapidly forming a confluent homogeneous monolayer. Cells cultured on HA-coated slide are almost viable (Fig.4c and 4d) thus attesting the citocompatibility of the hydrogels.

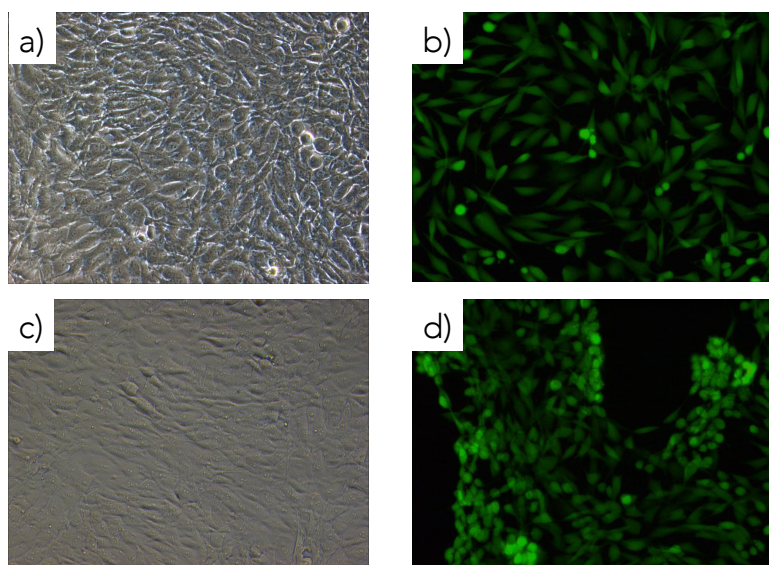


Figure 4. Phase contrast and fluorescent Live/Dead images of cells cultured on a bare glass slide (a) and (b) and on HA:DVS-coated glass slide.

The presence of few dead cells is probably due to the HA layer detachment from the underlying substrates (Fig.5), which causes cells loss of adhesion and membrane breakage.

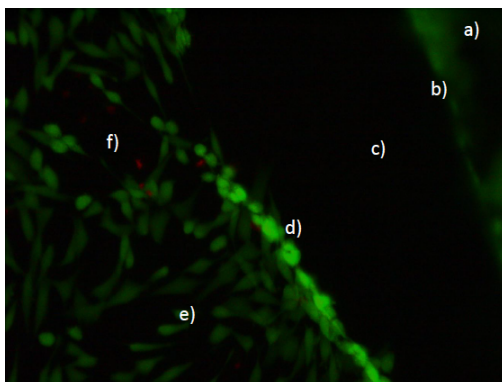


Figure 5. Fluorescence microscope image of a HA:DVS coating partially detached from the glass slide. a) Viable cells adhering to the underneath glass after coating detachment; b) glass edge; c) uncoated glass slide still not repopulated by cells; d) viable cells on detached HA layer; e) viable cells on HA-coated glass; f) dead cells (in red) in the proximity of HA layer detachment.

### 4.3.3 Hydrogel characterization

A reliable methodology based on three independent techniques was used to test the mechanical behavior of DVS-cross-linked swollen hydrogels and photocross-linked GMHA hydrogels: rheological analysis, swelling ratio measurements with Flory-Rehner calculations, and AFM nanoindentation. While rheology is a consolidated method giving the most reliable experimental results that allows to directly evaluating the cross-linking efficiency, it is unsuitable to test small size samples as those typically used for coating scaffolds. In those conditions thermogravimetric experiments and/or AFM measurements can be alternatively carried out. However, their reliability has to be assessed with proper crosscheck experiments.

#### 4.3.3.1 Rheology

Rheological measurements were carried out for HA:DVS swollen gels after three days of immersion in deionized water. The viscoelastic behavior of 3% HA

solution without DVS was also considered. According to the experimental curves obtained HA solution behaves as a viscous liquid with  $G'' > G'$  in all frequency range explored (Fig.6).

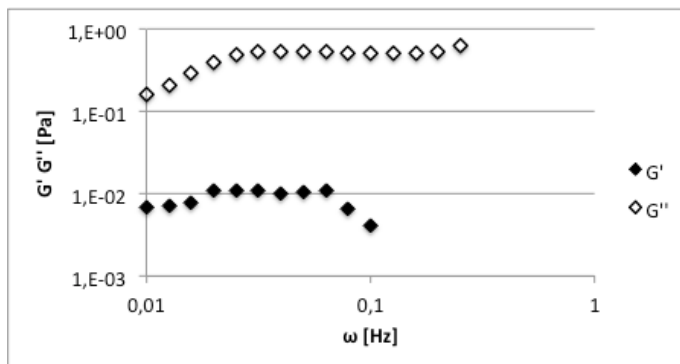


Figure 6. Viscous ( $G''$ ) and elastic ( $G'$ ) modulus components obtained for HA solution 3% (w/v).

After covalent cross-linking HA molecules, (Fig.7, 8, and 9) the elastic component prevails with storage modulus almost independently on frequency and always higher than loss modulus for all HA3%<sub>1/10</sub> samples. Similar behavior but with lower  $G'$  plateau values are shown by HA3%<sub>1/5</sub> samples.

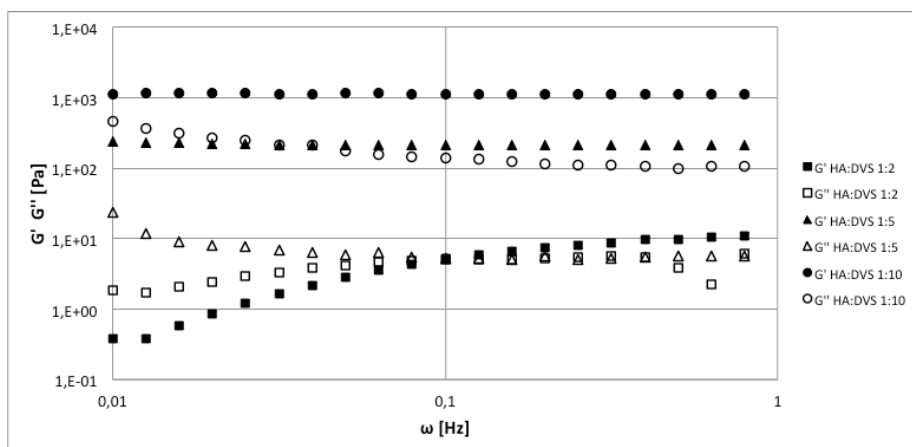


Figure 7. Viscous ( $G''$ ) and elastic ( $G'$ ) modulus components for hydrogels obtained after 2 hours of curing. While the HA3%<sub>1/10</sub> and HA3%<sub>1/5</sub> behave as cross-linked hydrogels with  $G'$  predominating over  $G''$ , the HA3%<sub>1/2</sub> has a change from viscous liquid behavior ( $G'' > G'$ ) at lower frequencies to elastic solid behavior ( $G'' < G'$ ) at higher frequencies

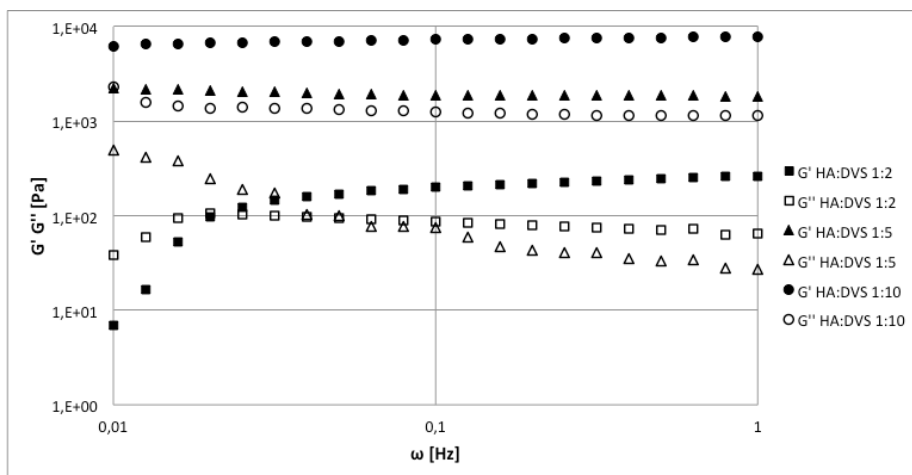


Figure 8. Viscous ( $G''$ ) and elastic ( $G'$ ) modulus components for hydrogels obtained after 12 hours of curing. Increasing in crosslinking reaction time till 12 hours, without changing in DVS content, lead to elastic and viscous moduli enhancement. A crossover phenomenon is still observed for HA3%<sub>1/2</sub>.

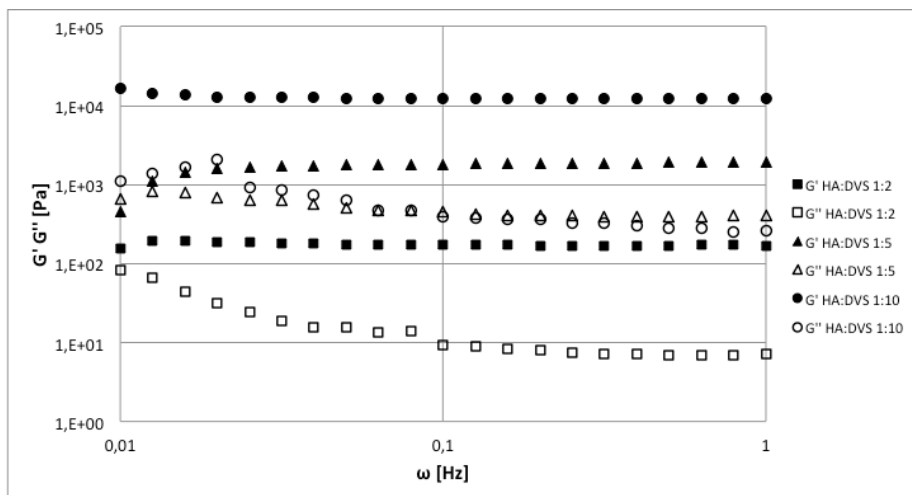


Figure 9. Viscous ( $G''$ ) and elastic ( $G'$ ) modulus components for hydrogels obtained after 96 hours of curing. Elastic and viscous moduli are almost constant within all frequency range, with  $G'$  predominating over  $G''$ . Further moduli enhancement, even if restrained, is observed comparing to 12 hours of curing moduli values.

For the sample HA3%<sub>1/2\_2h</sub> a sol-gel transition at 0.1 Hz is observed suggesting incomplete cross-linking. A qualitatively similar behavior was observed also for the others HA3%<sub>1/2</sub> samples although with much lower crossover frequency (higher molecular weight). We assumed HA3%<sub>1/2\_2h</sub>

parameters conditions (2h curing time, HA:DVS = 1:2) as threshold values to efficiently cross-link HA. Results showed that both stoichiometric ratio and reaction times can be used to fine-tune the hydrogel stiffness to the desired value. Actually, according to Equation 1 the corresponding Young's moduli  $E_{RH}$  are in the range from 0.03 to 37 kPa (Table 3).

Extending the reaction time without varying DVS content is efficient to strengthen hydrogels; increasing from 2h to 12h led to an enhancement in  $G'$  of nearly an order of magnitude, whereas extending curing time till 96h has a minor effect. This may allow for a reduction of DVS quantities with better hydrogel biocompatibility or less laborious washing treatments.

Finally, the cross-linking density  $\nu_{RH}$  of the networks was estimated according to Equation 2, and results are shown in Table 3. Actually  $\nu_{RH}$  values range from  $4.18E-09$  mol/cm<sup>3</sup> to  $4.08E-06$  mol/cm<sup>3</sup>.

Table 3. Storage modulus  $G'$  and cross-link density  $\nu$  obtained from rheological analyses (RH). Numerical values obtained showed the trend of hydrogels enhancing with increasing both curing time and DVS content.

Sample	$G'_{RH}$ [kPa]	$\nu_{RH}$ [mol/cm]
HA3%_1/2_2h	0.01 ± 0.003	4.18E-09 ± 1.2E-09
HA3%_1/2_12h	0.17 ± 0.01	6.47E-08 ± 5.6E-09
HA3%_1/2_96h	0.19 ± 0.01	6.77E-08 ± 5.6E-09
HA3%_1/5_2h	0.21 ± 0.01	8.45E-08 ± 5.6E-09
HA3%_1/5_12h	1.5 ± 0.5	5.95E-07 ± 1.8E-07
HA3%_1/5_96h	1.87 ± 0.41	7.26E-07 ± 1.6E-07
HA3%_1/10_2h	1.11 ± 0.04	4.43E-07 ± 1.65E-08
HA3%_1/10_12h	7.5 ± 2.2	2.92E-06 ± 8.5E-07
HA3%_1/10_96h	12.4 ± 0.9	4.08E-06 ± 3.5E-07

#### 4.3.3.2 Swelling ratio determination and Flory-Rehner calculations

The extent of swelling of hydrogels can be related to their density of cross-linking. The swelling was measured through thermogravimetric analysis, using the Flory-Rehner theory to calculate both the molecular weights between cross-links  $M_c$  and cross-link densities  $\nu_{FR}$  for HA:DVS. As data reported in Table 4 showed, as DVS content and curing time increased, swelling ratio  $q_M$  decreased, indicating higher levels of cross-linking which is in accordance with the theory of rubber elasticity<sup>35</sup>. Flory-Rehner calculations showed that increased HA:DVS stoichiometric ratio and curing time led to decreased molecular weights between cross-links (ranging from 86.2E+06 g/mol for HA:DVS 1:2 and curing time 2h, to 3.06E+05 for HA:DVS 1:10 and curing time 96h), as well as increased cross-link density  $\nu_{FR}$  (ranging from 1.42E-08 mol/cm<sup>3</sup> to 5.37E-06 mol/cm<sup>3</sup>).

Table 4. Storage modulus  $G'_{FR}$ , cross-link density  $\nu_{FR}$ , swelling ratio  $q_M$  and molecular weight between cross-links  $M_c$  obtained from TGA analysis (indicated with the subscript FR) are presented.  $G'_{FR}$  and  $\nu_{FR}$  values resulted in good agreement with numerical values obtained from rheological tests attesting the trend of hydrogels enhancing with increasing both curing time and DVS content.

Sample	$q_M$	$M_c$ [g/mol]	$\nu_{FR}$ [mol/cm <sup>3</sup> ]	$G'_{FR}$ [kPa]
HA3%_1/2_2h	839.56	86.2E+06	1.42E-08 ± 2.6E-09	0.037 ± 0.007
HA3%_1/2_12h	781.88	76.6E+06	1.60E-08 ± 4E-09	0.041 ± 0.01
HA3%_1/2_96h	552.46	42.9E+06	3.28E-08 ± 6E-09	0.084 ± 1.5E-02
HA3%_1/5_2h	331.46	18.3E+06	9.63E-08 ± 1.2E-08	0.25 ± 3.1E-02
HA3%_1/5_12h	120.12	4.47E+06	4.93E-07 ± 2.27E-07	1.27 ± 5.8E-01
HA3%_1/5_96h	79.03	1.6E+06	8.32E-07 ± 1.4E-07	2.14 ± 3.5E-01
HA3%_1/10_2h	161.67	5.53E+06	4.93E-07 ± 3.3E-07	1.27 ± 8.6E-01
HA3%_1/10_12h	50.95	8.03E+05	1.19E-06 ± 4.8E-07	3.06 ± 1.2
HA3%_1/10_96h	28.63	3.06E+05	5.37E-06 ± 1.9E-06	1.39E+01 ± 4.9

Those data were used for fitting the Equation 2 in order to calculate  $G'_{FR}$ . The difference between  $G'_{RH}$  and  $G'_{FR}$  experimental values ranges from a minimum of 0.027 kPa to a maximum of 4.14 kPa (Fig.10), a reasonably narrow gap taking into account that the two analyses are based on completely different approaches. TGA estimated storage moduli matches with rheological measured values thus

allowing to exploit TGA as an easy and reliable way to indirectly evaluate the mechanical characteristic of hydrogels scaffold thin coatings, just sampling a few milligrams of HA from the functionalized scaffold surfaces, necessary to be sensed in the TGA weighing pan.

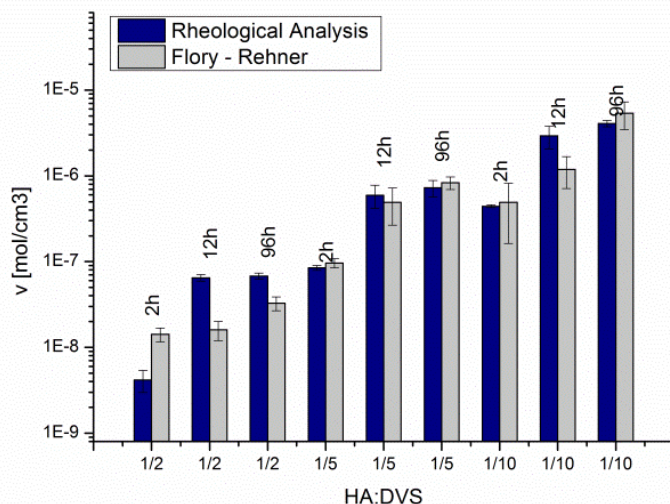


Figure 10. Comparison of cross-link density  $\nu$  values obtained with rheology and TGA analyses.

Having attested its reliability, TGA analyses were implemented on the GMHA photocross-linked hydrogels samples obtained by radical polymerization of 2 mg/ml GMHA solution mixed with 1.5% (w/v) I2959 photoinitiator in the presence of UV-light. The cross-link density  $\nu_{FR}$  values obtained, reported in Table 5, were comparable to those from HA:DVS hydrogels cross-linked for 12 h with 5-fold DVS molar excess. Finally, molecular weights between cross-links  $M_c$  and crosslink densities  $\nu_{FR}$  were used to fit the Equation 2 in order to calculate the  $G'$  storage modulus which resulted of about 0.4 kPa.

Table 5. Numerical values obtained from TGA analyses. Swelling ratio  $Q_M$ ; cross-link density  $\nu_{FR}$  and storage modulus  $G'_{FR}$  are reported for GMHA hydrogels.

Sample	$Q_M$	$\nu_{FR}$ [mol/cm <sup>3</sup> ]	$G'_{FR}$ [kPa]
GMHA	208.75 ± 28.07	1.5E-07 ± 3.54 E-08	0.39 ± 0.09

#### 4.3.3.3 AFM Nanoindentation

Finally, Young's moduli  $E_{AFM}$  of 1:5 and 1:10 HA:DVS samples were measured from the force-distance curves obtained randomly indenting HA hydrogel surfaces. AFM nanoindentation of hydrogels is often carried out in liquid phase. The technique isn't however applicable to any AFM instrument and its major drawback is the difficult laser setting on the cantilever, and the disturbed signal on the photodiode due to the refraction given by the water-air interface. On the other hand the main problem arising from AFM nanoindentation in air (as the technique adopted in this work) is the possibility of strong tip-substrate adhesion phenomena, typical of very flexible cantilevers. Actually several problems were met in our case while approaching the sample because the tip was suddenly attracted towards the sample making it difficult to identify the tip/gel surface contact point, and impossible to remove it during the unloading step. Tip-substrate adhesion was effectively minimized - although not completely eliminated - by carrying out a gas-phase hydrophobization of the tip (see Experimental Part 5.2.3.3). The residual adhesion can be taken into account using the JKR model instead of the classical Hertz equation. As shown in Figure 11 and 12, the deflection and force due to the adhesion are much higher than the applied force and this affects both loading and unloading curves<sup>36</sup>. The adhesion force  $F_{ad}$  was calculated according to the Hooke's law from the pull-off cantilever deflection as  $F_{ad} = k_c \Delta d_{ad}$  (Table 6). By comparing the experimental results, it is noteworthy to observe that the HA3%<sub>1/10</sub><sub>12h</sub> sample showed a perfectly elastic behavior with loading and unloading curves totally overlapped. On the contrary, the softer HA3%<sub>1/5</sub><sub>12h</sub> sample showed a hysteresis, suggesting the presence of dissipation phenomena due to the viscoelastic nature of the hydrogel and high water content of these cross-linked hydrogels. Moreover, while approaching the tip deflection was anticipated for the HA3%<sub>1/5</sub><sub>12h</sub> sample. Probably, this is due to the difference in water content of the two samples, previously attested with  $q_M$  swelling measurements (Table 4), which leads to differences in adhesion force  $F_{ad}$ .

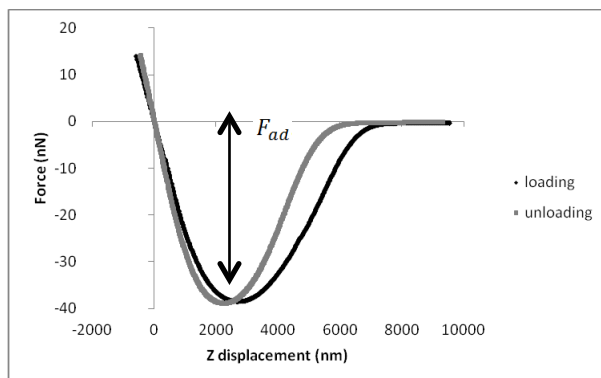


Figure 11. Force-distance curves of HA3%\_1/5\_12h sample. The jump in the signal deflection affecting both the loading and the unloading curves is due to the strong tip-substrate adhesion phenomena as a consequence of the presence of an aqueous meniscus on the hydrogel sample. The hysteresis attested viscoelastic dissipation

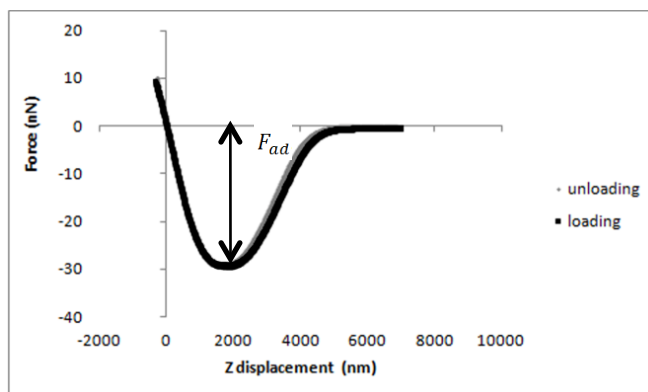


Figure 12. Force-distance curves of HA3%\_1/10\_12h sample: the complete overlapping of the two curves in the linear phase of the signal, attested a perfect elastic behavior of the sample.

The mathematical JKR model (Eq.13), suitable for soft sample and taking into account the adhesive component, was used to estimate Young modulus  $E_{AFM}$  starting from experimental data and tip geometrical characteristics.  $E_{AFM}$  average values turned out to be about 32 kPa for HA3%\_1/5 and 72 kPa for HA3%\_1/10 (Table 6). They indicated increasingly stiffer hydrogels with increasing HA:DVS content confirming the trend seen with previous characterization. We also observed that Young's modulus measured by AFM varied depending on the selection of

indentation depths: the variation of the indentation depth from 400 nm to 800 nm could result in a decrease of  $E_{AFM}$  from 47 kPa to 20 kPa for HA3%\_1/5. Similarly, HA3%\_1/10 showed a modulus of 79 kPa at small indentation depth of 230 nm and its behavior at larger indentation depths (350 nm) revealed a value of 54 kPa.

Table 6. Numerical values for AFM nanoindentation experiments on HA3%\_1/5\_12h and HA3%\_1/10\_12h samples. The elastic indentation of the samples ( $\delta$ ), the adhesion force ( $F_{ad}$ ) and the elastic modulus ( $E_{AFM}$ ) are reported. In the last column the elastic moduli obtained from rheology ( $E_{RH}$ ) are reported as comparison

Sample	$\delta$ [nm]	$F_{ad}$ [nN]	$E_{AFM}$ (JKR) [kPa]	$E_{RH}$ (23°C) [kPa]
HA3%_1/5_12h	567.77 ± 65.68 (400 ÷ 800)	38.47 ± 0.31	32.40 ± 4.23 (20 ÷ 47)	4.4 ± 0.4
HA3%_1/10_12h	281.57 ± 16.88 (230 ÷ 350)	29.45 ± 5.89	72.13 ± 3.24 (54 ÷ 79)	21.6 ± 6.3

These  $E_{AFM}$  values were compared with  $E_{RH}$  values derived from rheological measurements<sup>37</sup> and calculated exploiting the Equation 1 and Equation 2 taking into account that the two analyses were performed at different temperature (See Experimental Part) and the sources of uncertainty in AFM-based materials property measurements, such as the actual cantilever spring constant and the AFM tip shape<sup>37-39</sup>. The values of elastic modulus obtained from AFM nanoindentation resulted rather higher than those from rheology. It is likely that for these samples a major source of systematic error is the partial loss of water during the indentation experiments performed in air that lead the hydrogels to get slightly stiffer than those completely swelled (Table 5). This phenomenon mainly affected the HA3%\_1/5  $E_{AFM}$  -  $E_{RH}$  values due to its higher water content with respect to HA3%\_1/10, in accordance with swelling ratios  $q_M$  (Table 4). Further investigations are needed to systematically minimize this gap, both estimating the actual hydrogel water content during the measurement with proper gravimetric analyses and understanding the effect of the selected indentation depth range on the estimation of the elastic modulus.

## 4.4 Conclusions

In the present work, we presented an in-depth study of the process for chemically cross-linking HA hydrogels allowing to fine tune their physical properties. Particularly, we meant to obtain hydrogels with mechanical properties closely approximating those of natural stem cells ECM niches. We first optimized a cross-linking procedure for HA:DVS hydrogels synthesis and we aimed to understand the effect that varying DVS content and curing time have on HA hydrogels stiffness, which was evaluated through rheology, swelling measurements and first AFM nanoindentation experiments. The first technique is a consolidated and well-known method giving the most reliable experimental results and it allows to directly evaluating the cross-linking efficiency through the storage and loss moduli measurements. However it can be performed over macroscopic sample and it results unsuitable for small-sized hydrogels samples. Rheological results were benchmarked and used to assess the viability of the others two techniques which are experimentally harder but much more suitable for mechanical properties investigation at the microscale. Particularly, for swelling experiments just few milligrams of hydrogels should be collected from the coated scaffold surfaces, whereas AFM nanoindentation could be directly implemented on the hydrogel grafted onto micrometric structures. The good agreement between rheological and thermogravimetric characterization data proved both the repeatability and reliability of samples preparation. Very interestingly, our results demonstrated that combining cross-linking parameters it was possible to prepare samples with Young's moduli in the range from 0.03 to 37 kPa largely included in the stem cells niches physiological range. Moreover, it was possible to strengthen the materials just increasing curing time without varying DVS content, gaining in biocompatibility. This highlights that these hydrogels are suitable candidate as micrometric scaffold surfaces coating to be implemented in regenerative medicine for engineering stem-cells niches. Further improvements in AFM nanoindentation analyses, suggested to be the best small-sized sample characterization technique, will give the chance to directly evaluate

HA-coated micrometric scaffold mechanical properties.

As a minor issue, photocross-linkable hydrogels were prepared by linking hyaluronic acid with glycidyl methacrylate; the resulting hydrogel (GMHA) was UV-cross-linked. The GMHA mechanical properties were tailored by modulating degree of methacrylation, HA and photoinitiator concentration to fit tissue engineering application. Swelling experiments attested GMHA stiffness to be about 0.4 kPa, thus allowing considering even GMHA matrix as a suitable coating material for osteo-chondral niches mimicking.

## 4.5 References

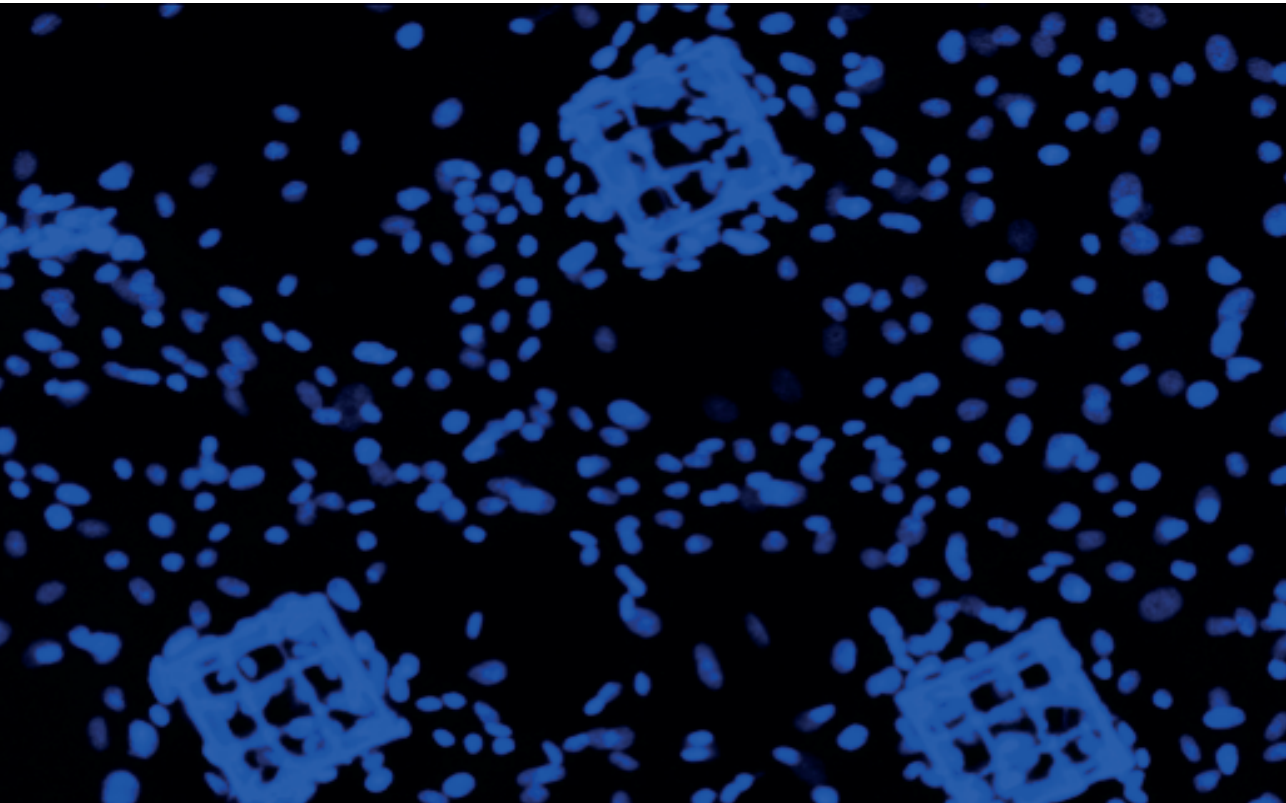
1. Lutolf, M. P. & Blau, H. M. Artificial stem cell niches. *Adv. Mater.* **21**, 3255–68 (2009).
2. Hachet, E., Van Den Berghe, H., Bayma, E., Block, M. R. & Auzély-Velty, R. Design of biomimetic cell-interactive substrates using hyaluronic acid hydrogels with tunable mechanical properties. *Biomacromolecules* **13**, 1818–27 (2012).
3. Discher, D. E., Janmey, P. & Wang, Y. Tissue Cells Feel and Respond to the Stiffness of Their Substrate. *Sci.* **310**, 1139–1143 (2005).
4. Evans, N. D. *et al.* Substrate stiffness affects early differentiation events in embryonic stem cells. *Eur. Cells Mater.* **18**, 1–13 (2009).
5. Engler, A. J., Sen, S., Sweeney, H. L. & Discher, D. E. Matrix elasticity directs stem cell lineage specification. *Cell* **126**, 677–89 (2006).
6. Ibrahim, S., Joddar, B., Craps, M. & Ramamurthi, A. A surface-tethered model to assess size-specific effects of hyaluronan (HA) on endothelial cells. *Biomaterials* **28**, 825–35 (2007).
7. Ji, Y. *et al.* Electrospun three-dimensional hyaluronic acid nanofibrous scaffolds. *Biomaterials* **27**, 3782–92 (2006).
8. Takagi, A. *et al.* Incorporation into a biodegradable hyaluronic acid matrix enhances in vivo efficacy of recombinant human interleukin 11 (rhIL11). *J. Control. Release* **115**, 134–9 (2006).
9. Peppas, N. A., Hilt, J. Z., Khademhosseini, A. & Langer, R. Hydrogels in Biology and Medicine: From Molecular Principles to Bionanotechnology. *Adv. Mater.* **18**, 1345–1360 (2006).
10. Schanté, C. E., Zuber, G., Herlin, C. & Vandamme, T. F. Chemical modifications of hyaluronic acid for the synthesis of derivatives for a broad range of biomedical applications. *Carbohydr. Polym.* **85**, 469–489 (2011).
11. Xu, X., Jha, A. K., Harrington, D. A., Farach-Carson, M. C. & Jia, X. Hyaluronic Acid-Based Hydrogels: from a Natural Polysaccharide to Complex Networks. *Soft Matter* **8**, 3280–3294 (2012).
12. Burdick, J. A. & Prestwich, G. D. Hyaluronic acid hydrogels for biomedical applications. *Adv. Mater.* **23**, H41–56 (2011).
13. Gaffney, J., Matou-Nasri, S., Grau-Olivares, M. & Slevin, M. Therapeutic applications of hyaluronan. *Mol. Biosyst.* **6**, 437–43 (2010).

14. Kenne, L. *et al.* Modification and cross-linking parameters in hyaluronic acid hydrogels--definitions and analytical methods. *Carbohydr. Polym.* **91**, 410–8 (2013).
15. Bencherif, S. A. *et al.* Influence of the degree of methacrylation on hyaluronic acid hydrogels properties. *Biomaterials* **29**, 1739–49 (2008).
16. Yeom, J. *et al.* Effect of cross-linking reagents for hyaluronic acid hydrogel dermal fillers on tissue augmentation and regeneration. *Bioconjug. Chem.* **21**, 240–7 (2010).
17. Camci-Unal, G., Cuttica, D., Annabi, N., Demarchi, D. & Khademhosseini, A. Synthesis and characterization of hybrid hyaluronic acid-gelatin hydrogels. *Biomacromolecules* **14**, 1085–92 (2013).
18. Flory, P. J. *Principles\_of\_Polymer\_Chemistry*. 672 (1953).
19. Markert, C. D. *et al.* Characterizing the micro-scale elastic modulus of hydrogels for use in regenerative medicine. *J. Mech. Behav. Biomed. Mater.* **27**, 115–27 (2013).
20. Collins, M. N. & Birkinshaw, C. Morphology of crosslinked hyaluronic acid porous hydrogels. *J. Appl. Polym. Sci.* **120**, 1040–1049 (2011).
21. Baier Leach, J., Bivens, K. A., Patrick Jr., C. W. & Schmidt, C. E. Photocrosslinked hyaluronic acid hydrogels: Natural, biodegradable tissue engineering scaffolds. *Biotechnol. Bioeng.* **82**, 578–589 (2003).
22. Prata, J. E., Barth, T. A., Bencherif, S. A. & Washburn, N. R. Complex Fluids Based on Methacrylated Hyaluronic Acid. *Biomacromolecules* **11**, 769–775 (2010).
23. Anseth, K. S., Bowman, C. N. & Brannon-Peppas, L. Mechanical properties of hydrogels and their experimental determination. *Biomaterials* **17**, 1647–1657 (1996).
24. Gekko, K. in *Solution Properties of Polysaccharides* **150**, 29–415 (AMERICAN CHEMICAL SOCIETY, 1981).
25. Marsano, E., Gagliardi, S., Ghioni, F. & Bianchi, E. Behaviour of gels based on (hydroxypropyl) cellulose methacrylate. *Polymer (Guildf)*. **41**, 7691–7698 (2000).
26. Butt, H.-J., Cappella, B. & Kappl, M. Force measurements with the atomic force microscope: Technique, interpretation and applications. *Surf. Sci. Rep.* **59**, 1–152 (2005).
27. Johnson, K. L., Kendall, K. & Roberts, A. D. Surface Energy and the Contact of Elastic Solids. *Proc. R. Soc. Lond. A. Math. Phys. Sci.* **324**, 301–313 (1971).

28. Sneddon, I. N. The relation between load and penetration in the axisymmetric boussinesq problem for a punch of arbitrary profile. *Int. J. Eng. Sci.* **3**, 47–57 (1965).
29. Flores-Merino, M. V *et al.* Nanoscopic mechanical anisotropy in hydrogel surfaces. *Soft Matter* **6**, 4466–4470 (2010).
30. Lin, D. C., Dimitriadis, E. K. & Horkay, F. Robust strategies for automated AFM force curve analysis-II: adhesion-influenced indentation of soft, elastic materials. *J. Biomech. Eng.* **129**, 904–12 (2007).
31. Collins, M. N. & Birkinshaw, C. Comparison of the effectiveness of four different crosslinking agents with hyaluronic acid hydrogel films for tissue-culture applications. *J. Appl. Polym. Sci.* **104**, 3183–3191 (2007).
32. Collins, M. N. & Birkinshaw, C. Physical properties of crosslinked hyaluronic acid hydrogels. *J. Mater. Sci. Mater. Med.* **19**, 3335–43 (2008).
33. Van Dijk-Wolthuis, W. N. E., Kettenes-van Den Bosch, J. J., Van Der Kerk-van Hoof, A. & Hennink, W. E. Reaction of dextran with glycidyl methacrylate: An unexpected transesterification. *Macromolecules* **30**, 3411–3413 (1997).
34. Prado, S. S., Weaver, J. M. & Love, B. J. Gelation of photopolymerized hyaluronic acid grafted with glycidyl methacrylate. *Mater. Sci. Eng. C* **31**, 1767–1771 (2011).
35. Treloar, L. R. G. *The Physics of Rubber Elasticity*. (OUP Oxford, 2005). at <<http://books.google.it/books?id=-iyDehYpoAQC>>
36. Akhlaghi, S., Sharif, A., Kalae, M., Nouri, A. & Manafi, M. Morphology, nanomechanical and thermodynamic surface characteristics of nylon 6/feather keratin blend films: an atomic force microscopy investigation. *Polym. Int.* **61**, 646–656 (2012).
37. Clifford, C. A. & Seah, M. P. Quantification issues in the identification of nanoscale regions of homopolymers using modulus measurement via AFM nanoindentation. *Appl. Surf. Sci.* **252**, 1915–1933 (2005).
38. Lin, D. C. & Horkay, F. Nanomechanics of polymer gels and biological tissues: A critical review of analytical approaches in the Hertzian regime and beyond. *Soft Matter* **4**, 669 (2008).
39. Wagner, R., Moon, R., Pratt, J., Shaw, G. & Raman, A. Uncertainty quantification in nanomechanical measurements using the atomic force microscope. *Nanotechnology* **22**, 455703 (2011).



**5.**  
**Mimicking stem cell niches through  
hydrogel functionalization of  
2PP scaffolds**



## 5.1 Introduction

The goal of tissue engineering is to replace or to repair a damaged tissue or organ with artificial tissue made by seeding cells on a synthetic structure, acting as extracellular matrix (ECM), as an alternative to autologous transplant, allograft, xenograft and prosthesis. Stem cells (SCs) that are unspecialized primitive cells able to differentiate into different types of mature cells, ensure support and regeneration of tissue thus possess great potential for these cell-based therapies. Physiologically SCs reside in specific anatomic locations, named niches, where they are exposed to a complex ensemble of chemical and mechanical stimuli affecting their cellular fate. However, before clinical applications, advancements in understanding how efficiently control and manipulate SCs fate is of key importance for successful SCs-based therapies. A promising strategy to achieve this goal consists in trying to regulate stem cells functions in artificial microenvironments, also called “synthetic niches”<sup>1</sup>. Synthetic niches, mimicking individual aspects of the interactions between stem cells and extracellular surroundings, including biochemical (e.g. delivery of soluble factors) and/or biophysical factors (e.g. substrate stiffness), would yield several benefits in understanding cell behavior in truly three-dimensional (3D) conditions. For example, hydrogel-based synthetic niches composed of hyaluronic acid<sup>2</sup> and gelatins<sup>3</sup> were recently used to study the role of matrix microenvironments (architecture, composition, stiffness) in specific commitment of bone marrow derived mesenchymal stem cells (MSCs). Particularly, these adult stem cells could be induced to differentiate exclusively into the adipocytic, chondrocytic, or osteocytic lineages<sup>4,5</sup>.

Within this context, an emergent tool to drive stem cell function is the employment of purely mechanical cues, such as patterned culture substrates inducing different levels of cell deformation. Alterations in the cell adhesion configuration are believed to affect cell cytoskeletal organization, which in turn might promote or inhibit changes in the nuclear morphology, nuclear physical and mechanical properties, DNA packing and gene<sup>6,7</sup>.

However, self-assembled scaffolds<sup>3</sup> do not allow fine controlling the structure geometry. To this end, two-photon laser polymerization (2PP) technique has emerged as a novel technology for the fabrication of advanced culture substrates overcoming self-assembled scaffolds limitations<sup>8</sup>. This powerful tool paved the way for the rapid prototyping of complex arbitrary 3D architectures with finely ultra-precise regulated geometries controlled at the cell scale (10  $\mu\text{m}$ ). Photopolymerization occurs by nonlinear two-photon absorption induced by femtosecond laser pulses tightly focused in transparent photosensitive materials that are basically hybrid inorganic-organic resins<sup>9</sup> whose biocompatibility has been extensively demonstrated<sup>10,11</sup>. 2PP polymeric resists employed have high mechanical stiffness (elastic moduli in the order of several GPa) thus allow obtaining complex free-standing 3D microstructures. On the contrary, this does not allow tailoring this parameter arbitrarily. Since the interactions of niches with the biological components occur at the surfaces, it is fundamental to modify the surface mechanical properties of the 2PP niches to faithfully reproduce physiological conditions. Particularly, cells seem to show a preference for well defined substrate stiffness best representing the tissue they derive from<sup>12</sup>.

In the present work, we have developed a strategy to engineer 3D scaffolds independently controlling both the 3D spatial architecture, allowed by 2PP, and substrate stiffness. To this end, artificial niche substrates were functionalized with thin layers of biocompatible hyaluronan- and gelatin-based hydrogels, which were modified by *via* cross-linking and conjugation reactions in order to tailor their mechanical and physico-chemical properties.

We used this culture model to study the interactions between structural and chemical biomimeticism on the response of MSCs in terms of proliferation and differentiation. To this purpose, we firstly verified the biocompatibility of the coated synthetic niche substrates using an immortalized cell line. Then, we cultured MSCs on the substrates and we evaluated their morphology, proliferation and differentiation.

## 5.2 Experimental section

### 5.2.1 2PP scaffold fabrication

#### 5.2.1.1 SZ2080 Photoresist

2PP synthetic niches were fabricated using the hybrid inorganic/organic photoresist SZ2080 (FORTH, Heraklion) belonging to the organically modified silane family (ORMOSILs) and developed in recent years for 2PP technology<sup>13</sup>. SZ2080 consisted of a blend of methacryloxypropyltrimethoxysilane (MAPTMS, 80%) and zirconium propoxide-methacrylic acid complex (ZPO, 20%). In order to provide an absorption band in the UV and trigger the 2PP process, the resin was doped with 1% (w/w) concentration of two different types of photoinitiator. Bis photoinitiator (Michler's ketone, 4,4'-bis(dimethylamino)benzophenone) adsorbing at 590 nm, and Irg photoinitiator (Irgacure 369, 2-Benzyl-2-dimethylamino-1-(4-morpholinophenyl)-butanone-1) adsorbing at 515 nm. Due to the Bis photoinitiator strong autofluorescence, hindering the characterization of the fluorescent markers used for biological diagnostics within the internal niche structure<sup>14</sup>, following results are presented just for niches obtained with Irg photoinitiator.

The dual-cure mechanism of the resin allows to minimize shrinkage phenomena during 2PP process and to increase photosensitivity thus allowing fabricating high-resolution 3D freestanding structures. The pre-baking step (104°C, 1h) consists of the thermal condensation of alkoxy groups and the formation of the inorganic matrix. While the sample is drying, alcohol, water and other solvents present are released from the system and the unstructured material shrinks. The final step involves the free radical polyaddition of C=C double bounds attached to the inorganic backbone further increasing the connectivity of the material. The pendant methacrylic groups are linked together without the release of any molecules, and thus no shrinkage phenomena are observed. A solution of 2-propanol and 4-methyl-2-pentanone (1:1) was used to remove uncured material.

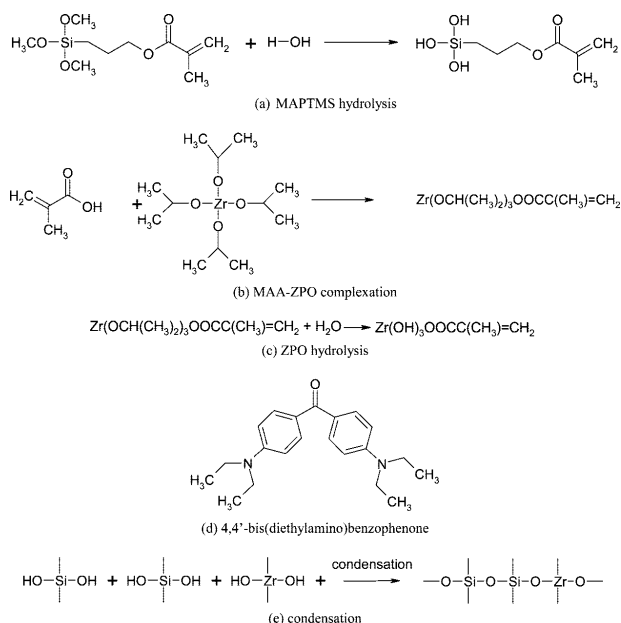


Figure 1. Chemical structure of the reagents and sol-gel process leading to the formation of the inorganic matrix.

### 5.2.1.2 Fabrication of synthetic niches by 2PP

Niches were 2PP fabricated in the SZ2080 photoresist doped with 1% concentration of Irg photoinitiator at the Institute for Photonics and Nanotechnology (IFN)-CNR, Milano, Italy. To achieve an efficient two-photon absorption process in the Irg-based SZ2080, the second harmonic (520 nm wavelength) of a based amplified laser (femtoREGEN, High Q Laser) with 400-fs pulse radiation at 1040-nm wavelength and 1MHz repetition rate was used. The pulses were focused with a 1.4-NA oil immersion microscope objective (Plan-APOCHROMAT, 100x oil immersion, Carl Zeiss, Oberkochen, Germany). Optimum laser writing conditions were 0.7-mm/s writing speed, 23-mW average power. Computer-controlled 3-axis motion stages (ABL-1000, Aerotech, Pittsburgh, PA, USA) interfaced by CAD-based software (ScaBase, Altechna, Vilnius, Lithuania) were used to translate the sample relative to the laser to form the desired 3D microarchitecture of the niches. To improve the robustness of the structures a double irradiation scan was performed with a lateral shift of 500 nm between the

two scans. The niche geometry was selected as the one most favoring spontaneous MSC homing and proliferation<sup>15</sup>. Individual niches were 30  $\mu\text{m}$  high and 90  $\mu\text{m}$  x 90  $\mu\text{m}$  in transverse dimensions and consisted of a lattice of interconnected lines, with a graded spacing between 10 and 30 microns transversely and a uniform spacing of 15  $\mu\text{m}$  vertically. The 3D niche was surrounded by four outer confinement walls formed by horizontal rods spaced by 7.5  $\mu\text{m}$  resulting in small gaps of 2  $\mu\text{m}$  (Fig.2). All the structural truss elements had an elliptical cross section with major axis of 5  $\mu\text{m}$  and minor axis of 2.5  $\mu\text{m}$ . These dimensions could be significantly reduced by fully exploiting the 2PP technique potential however they are required to provide mechanical stability to the engineered niches.

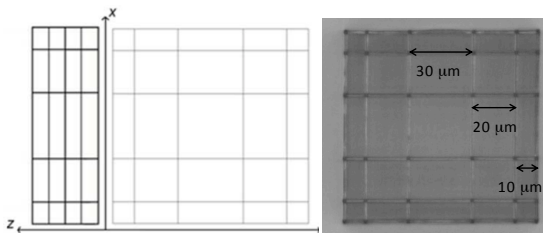


Figure 2. 2D projections of the 2PP engineered niche and MO image: Individual niches were 30  $\mu\text{m}$  high and 90  $\mu\text{m}$  x 90  $\mu\text{m}$  in transverse dimensions and consisted of a lattice of interconnected lines, with a graded spacing between 10 and 30 microns transversely and a uniform spacing of 15  $\mu\text{m}$  vertically.

Microstructures were laser written onto circular coverslip glasses of 150- $\mu\text{m}$  thickness and 12 mm diameter (BioOptika, Milano, Italy). On each cover glass, three niches were arranged in a triangular pattern, at a relative distance of 200  $\mu\text{m}$  (Fig.3).

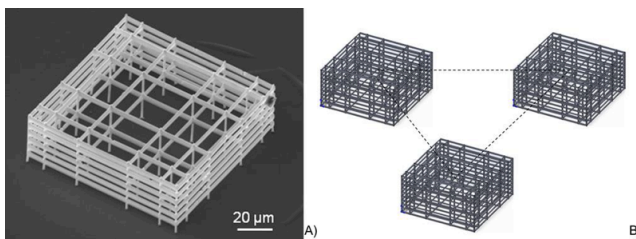


Figure 3. 3D configuration of the artificial niche substrate which was 2PP laser written on glass cover slips: SEM image of an individual 2PP niche (A); Layout of 3 niches rearrangement onto each glass slip (B): scheme of the triangular pattern with relative distance set at 200  $\mu\text{m}$ .

To improve the adhesion of the microstructures to the substrates avoiding their detachment during washing steps, glass cover slips were silanized in air with (3-Mercaptopropyl)trimethoxysilane (12h at 35°C in a closed vial) before depositing the photoresist.

Optical microscope and scanning electron microscope analyses were performed to verify the geometry of the laser written structures assessing the successful optimization of the laser writing conditions.

## 5.2.2 Design of the hydrogels coating

Hyaluronic acid (HA) hydrogels were prepared exploiting both chemical and photochemical cross-linking methods, whereas just a chemical reaction was investigated for gelatin-based hydrogels. Products and reagents, apart when not specified, were all purchased from Sigma-Aldrich and used without any purification.

### 5.2.2.1 Hyaluronic acid-divinyl sulfone (HA:DVS) chemical hydrogels

Powdered Hyaluronic acid sodium salt (NaHA,  $1.6 \times 10^6$  g/mol), obtained by fermentation of *Streptococcus equi* bacteria, was dissolved in alkaline solution (0.5% w/v, 0.2M NaOH, pH 13) and divinyl sulfone (DVS) was added as cross-linking agent directly into the HA solution<sup>16</sup> with HA:DVS molar ratio 1:10 (respect to HA primary hydroxyls). After stirring the mixture for 4 min in a closed vial to allow DVS uniform diffusion without its uncontrolled evaporation, the reaction was allowed to proceed for 12 hours at 4°C. Here on, we will be referring to these chemical cross-linked HA-based hydrogels as HA:DVS.

### 5.2.2.2 Synthesis of Glycidyl Methacrylated-Hyaluronic acid (GMHA) hydrogels

Photocrosslinkable hydrogels were synthesized functionalizing HA chains with methacrylate groups exploiting the simple and fast reaction with glycidyl methacrylate (GM). HA solution (1% w/v in distilled water) was reacted at room temperature for 24h with a 20 – fold molar excess of glycidyl methacrylate in the presence of 20 – fold molar excess of triethylamine acting as a catalyst<sup>17,18</sup>. Then the solution was precipitated twice in acetone, dissolved in distilled water, lyophilized (VirTis BenchTop Freeze dryer 2K) and finally stored desiccated in the dark at -20°C. <sup>1</sup>H-NMR spectroscopy analyses were done on GMHA conjugates dissolved in D<sub>2</sub>O in order to verify the efficiency of methacrylic functionalization<sup>19</sup>. GMHA hydrogels were then cross-linked by exposing GMHA solution (0.2% w/v in phosphate buffered saline, PBS) to UV-light ( $\lambda = 365$  nm, 4 mW/cm<sup>2</sup>, 10 min exposure) in nitrogen atmosphere in the presence of the water soluble photoinitiator Irgacure I2959 (1.5% w/v; Ciba Specialty Chemicals) and N-vinyl pyrrolidone (VP; 1.5% v/v), as reactive co-monomer as well as solvent for the photoinitiator.

### 5.2.2.3 Dopamine-conjugated Hyaluronic acid (HA-DA)

HA-dopamine conjugates were obtained exploiting conventional carbodiimide chemistry in the presence of water soluble 1-ethyl-3-(3-dimethylaminopropyl) carbodiimide hydrochloride (EDC) and 1-hydroxybenzotriazole (HOBT). Briefly, HA was dissolved in 250 ml of pure deionized water (DW) to a concentration of 2 mg/ml. To the solution, 237 mg of Dopamine Hydrochloride (DA) and 174 mg of EDC were added and the reaction mixture was stirred for 2 h at room temperature while maintaining pH value at 4.7 by addition of 0.1M HCl to avoid irreversible oxidation of dopamine<sup>20</sup>. The acidic pH also enables the coupling agent EDC to activate the carboxylic group of HA, thus allowing the bond formation with the amine group of dopamine. At the end of the reaction, HA-DA was precipitated in ethanol, re-dissolved in distilled water and dialyzed against

100mM NaCl solution for 1 day and against distilled water for 2 days. HA conjugation with dopamine was assessed with macroscopic colorimetric analysis: dissolving HA-DA in an alkaline solution (pH 8.5) it was possible to observe the solution turning its color into light brown, indicative of dopamine oxidation and cross-linking<sup>20</sup>. This phenomenon was not observed for an alkaline HA solution thus attesting the efficiency of conjugation.

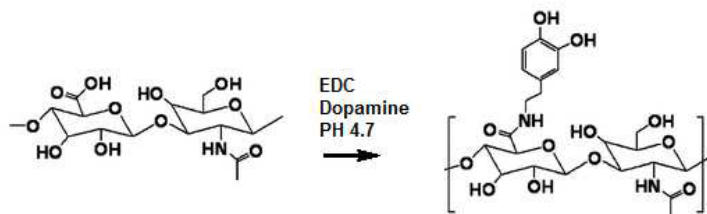


Figure 4. Scheme of HA chains functionalization with dopamine.

#### 5.2.2.4 Thiolated-modified Gelatin (Gel-SH) hydrogels

Thiol-modified gelatin (carboxymethyl gelatin-thiopropionyl hydrazide GTN-DTPH, Gelin-STM, Glycosan BioSystems, Inc.) was cross-linked exploiting a disulfide strategy using thiol-reactive cross-linker poly(ethylene glycol) diacrylate (PEGDA  $M_w = 3,400$  g/mol, Extralink™, Glycosan BioSystems, Inc.)<sup>21</sup>. PEGDA solution (0.5% w/v in DW) was added into the thiolated macromonomer solution (0.25% w/v in DW) to have a thiol: C=C double bonds ratio  $\approx 2:1$ <sup>22</sup>. All hydrogels were prepared under a blanket of nitrogen gas to minimize undesired air oxidation of thiolated groups. The mixture was stirred for 30 s and poured in a petri dish where the reaction was allowed to proceed overnight. Hydrogels mechanical properties can be tuned varying the concentration of both the thiolated gelatin and PEGDA solutions<sup>23</sup>.

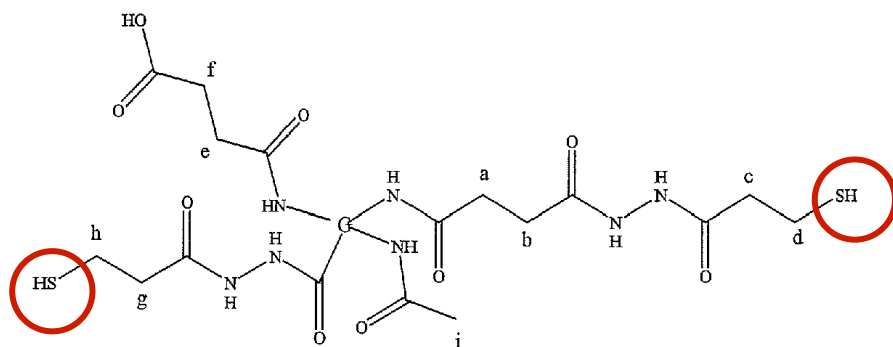


Figure 5. Chemical structure of Carboxymethyl gelatin-thiopropionyl hydrazide Gelin-SH™.

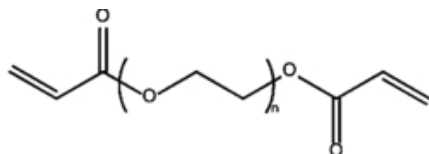


Figure 6. Chemical structure of Poly(ethylene glycol) diacrylate, PEGDA used as cross-linking agent.

### 5.2.3 Microfluidic channel fabrication

Different interactions at the interface between SZ2080 surfaces and the hydrogels were investigated to graft HA, GMHA and Gel-SH hydrogels in order to functionalize the 2PP microstructures. To overcome pores occlusion due to the viscosity and surface tension of the hydrogels solution, together with the small pores dimensions, functionalization processes, explained in following paragraph, were scaled-down and performed in a microfluidic system. Microfluidic channels were fabricated by soft-lithography techniques, according to which soft, organic materials are used to faithfully duplicate the shape, the morphology, and the relief structures present in a master obtained with standard photolithography technologies<sup>24</sup>.

#### 5.2.3.1 SU-8 and photo-lithographic process for master fabrication

SU-8 (GM1070, Gersteltec) is the epoxy resin used to fabricate high aspect ratio structured master by standard photolithography. SU-8 mold was fabricated on a silicon wafer according to the manufacturer instructions.

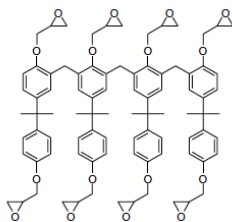


Figure 7. Chemical structure of the epoxy oligomer contained in SU-8 formulations.

The whole process can be schematized as follows:

- Silicon surface (8cm x 3cm) were cleaned with acetone, 2-propanol and ethanol and air-plasma treated (40 Watts for 60 seconds);
- A 200- $\mu\text{m}$  SU-8 film was spin-coated on the silicon surface (400 rpm for 40s) and left on a planar surface overnight to allow solvent evaporation;
- Softbaking of the coated substrate with a hot plate. First, the temperature was increased from room temperature up to 65°C in 20 minutes and substrates were kept at 65°C for 30 minutes. Then, the

temperature was increased up to 95°C in 15 minutes. The substrate was kept at this final temperature for 4 hours. All temperature ramps were performed at 2°C/min;

- SU-8 resist film were UV exposed through a chromium-quartz mask for 5 minutes. Channel profiles on the mask were 500  $\mu\text{m}$  in width and 200  $\mu\text{m}$  in height and were transparent so that UV-light could reach and impress the negative photo-resist;

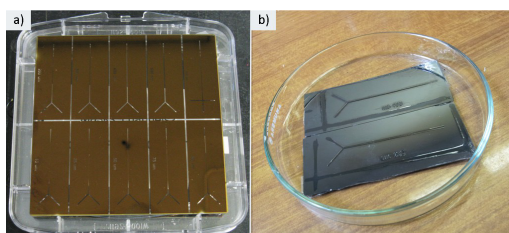


Figure 8: a) Quartz-chromium mask with patterned channels; b) SU-8 replica.

- 10 minutes substrate relaxation at room temperature;
  - Post-baking in four steps. First, the temperature was increased from room temperature to 65°C in 20 minutes. Then, substrates were kept at 65°C for 15 minutes. Finally, the temperature was increased up to 95°C in 15 minutes and samples were kept at that temperature for other 40 minutes;
  - Si wafer was immersed in propylene glycol monomethyl ether acetate (PGMEA) (Gersteltec), the developer. After 22 minutes the sample were rinsed with 2-propanol to stop the development reaction;
  - In the post-exposure baking the temperature was increased up to 135°C at 2°C/min and sample was kept at 135°C for the following 2 hours;
  - Si wafer were immersed in 2-propanol and cleaned with ultrasonic bath;
- Finally, the SU-8 structured wafer was functionalized with 1H,1H,2H,2H-perfluorooctyltriethoxysilane (ABCRCR, Germany) through air phase silanization (16h at 40°C in a closed vial) to later facilitate the release of the elastomeric stamp.

### 5.2.3.2 Micro-channel fabrication and glass bonding

Polydimethylsiloxane or PDMS material was used for the fabrication of micro-channels (500  $\mu\text{m}$  width and 200  $\mu\text{m}$  height) by replica of the SU-8 mold<sup>25</sup>. PDMS liquid pre-polymer and its curing agent (Sylgard® 184 Silicone Elastomer Kit, Dow Corning) were mixed at 10:1 w/w ratio and left 30 minutes under laminar flow hood to remove entrapped air bubbles. Then, the mixture was poured onto the SU-8 master and the cross-linking reaction was allowed to proceed at room temperature for 48 hours<sup>26</sup>.

A simple and versatile polymeric microfluidic system was obtained aligning the 12mm circular glass cover slip, where 2PP scaffolds are laser written, with PDMS  $\mu$ -channels, so that the scaffolds resulted centered. Bonding at the PDMS-glass interface was obtained by air-plasma treatment of the two surfaces (PECVD System, Kenosistech) at 60 Watts for 1 minute. Plasma parameters were experimentally optimized in order to obtain an efficient and reversible sealing that allowed both pumping hydrogels solutions without leakages phenomena and easily detaching the PDMS channels to recover scaffolds at the end of the coating process. PDMS low Young modulus allowed to conform the channels to glass surface with good sealing properties. Prior to bonding, PDMS channels were punched in order to create a hole where a syringe could be fitted in.

## 5.2.4 Scaffold surfaces functionalization

Coating processes were implemented and optimized to functionalize SZ2080 scaffolds surfaces with hydrogels macromolecules. Different hydrogels matrixes were studied and consequently different types of interactions at the interfaces with the SZ2080 synthetic niches were investigated and exploited. All the functionalization processes were scaled-down and performed in the simple and versatile PDMS-glass microfluidic system developed as described in 5.2.3.2.

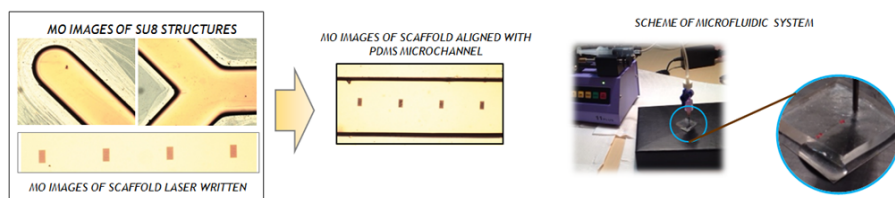


Figure 9. Basic scheme of the PDMS-glass microfluidic system implemented for scaffold surfaces functionalization with hydrogels.

### 5.2.4.1 HA:DVS chemisorption

HA:DVS chemical hydrogels were immobilized on the scaffolds exploiting physical interactions at the interface. HA:DVS solution (1:10 stoichiometric ratio) was prepared and pumped through the microfluidic system at 3  $\mu\text{l}/\text{min}$  (Syringe Pump 11 Plus, Harvard Apparatus) for 2 hours. During the process, two reactions occurred simultaneously, including DVS reaction to chemically cross-linking HA macromolecules, and the hydrogen bonding formation between the hydrophilic moieties of HA, such as carboxylic acid  $-\text{COOH}$  or hydroxyl  $-\text{OH}$  groups, with hydrophilic groups generated on the SZ2080 surfaces after the air plasma treatment. Then, the PDMS channels were peeled off and the DVS reaction was allowed to proceed overnight at  $4^{\circ}\text{C}$ . At the end, the coated samples were rinsed with distilled water in order to remove the unattached gel and avoid niches pores occlusion.

#### 5.2.4.2 GMHA photo-grafting

The GMHA hydrogels were UV-photografted on the SZ2080 surfaces exploiting the free-radical polymerization of the methacrylate groups of the chemically modified hyaluronic acid with the residual unreacted double bonds of the 2PP surfaces. In order to strengthen gels adhesion, SZ2080 surfaces were also functionalized with methacrylate groups through a vapor phase silanisation performed before GMHA functionalization. Glass slip with 2PP structures were air-plasma treated and incubated at 35°C for 12 hours with 0.3 ml aliquot of 3-acryloxypropyl methyldimethoxysilane (APMES, ABCR Germany). Once assembled the microfluidic system, GMHA-photoinitiator mixture, prepared as previously described, was fluxed through the channels at 3  $\mu$ l/min first for 10 minutes and then for 23 minutes. At the end of each flowing section, coated samples were UV irradiated for 3 minutes to allow hydrogel formation. Then, the PDMS was peeled off and coated samples were rinsed with distilled water to remove unreacted material and UV-exposed for 10 minutes in nitrogen atmosphere to complete photografting and photo cross-link reaction.

#### 5.2.4.3 Dopamine conjugated Hyaluronic acid (HA-DA) grafting

HA-DA grafting strategy on the 2PP surfaces exploited the capability of the adhesive protein dopamine to undergo oxidative polymerization at alkaline pH forming polydopamine (PD) surface-adherent layer that can attach to all inorganic and organic surfaces<sup>27,28</sup>. Self-polymerization mechanism involves catechol-quinone transition (catechol oxidation), which is triggered following Michael addition and spontaneous catechol polymerization forming complex networks with free catechol groups responsible for its strong adhesion to any kind of surfaces. HA-DA was first dissolved in 10 mM Tris-HCl (pH 8.5) at 2 mg/ml and then 20  $\mu$ l of solution were dropwised on each samples. After 12 hours at room temperature, the samples were rinsed with deionized water. Catechol groups conjugated to the HA macromolecules are involved in the hydrogel phenomena adhesion to the scaffold surfaces<sup>31</sup>.

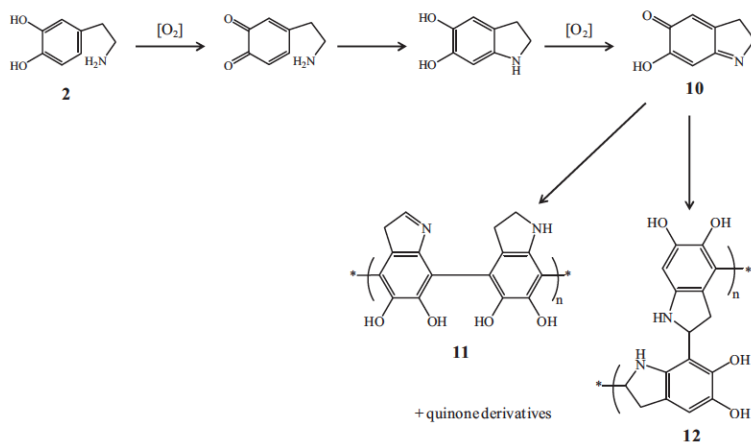


Figure 10. Possible reaction scheme for the formation of polydopamine layer by self-polymerization of dopamine<sup>29,30</sup>.

#### 5.2.4.4 Polydopamine (PD) and thiolated-gelatin (Gel-SH)

Gel-SH hydrogels were grafted on the 2PP surfaces using dopamine as intermediate linker<sup>27</sup>. First, 3D niches were treated with a dilute aqueous solution of dopamine buffered to a pH typical of marine environments (8.5) to form a thin PD layer, which is extremely reactive towards thiols and amines.

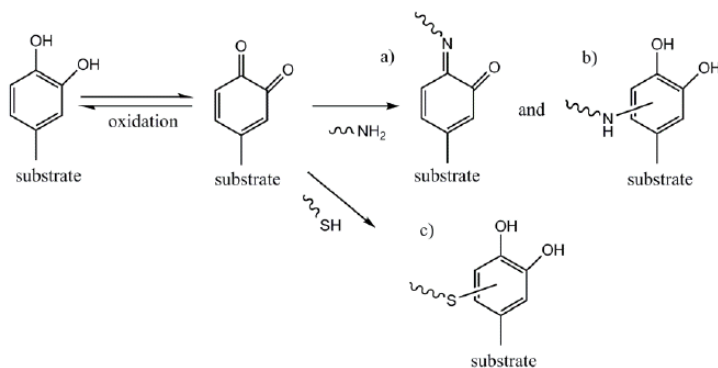


Figure 11. Scheme of the two-steps immobilization strategy exploited for the immobilization of gelatin chains.

A dopamine hydrochloride solution (2 mg/ml in Tris-HCl 10 mM, pH 8.5) was fluxed through the  $\mu$ -structured samples (3  $\mu$ l/min for 12h). Samples surfaces turned to black, the typical mussels color<sup>32</sup>, as the PD deposition proceeded.

Then, the PDMS channels were detached, the PD-coated structures were rinsed with distilled water and incubated overnight with 200  $\mu\text{l}$  of Gel-SH:PEGDA solution in nitrogen atmosphere so that the thiol groups of gelatin can be covalently conjugated to the PD layer via the quinone group thus grafting the gelatin macromolecules to the substrate. At the end the samples were washed with distilled water to remove material in excess.

### 5.2.5 Hydrogels coating characterization

Coating processes efficiency was evaluated through optical microscope (MO) and environmental scanning electron microscope (SEM) analyses. Moreover, the scaffold functionalization processes were implemented onto SZ2080 2D flat surfaces in order to assess the hydrogels grafting even through surface characterization techniques such as optical contact angle (OCA) measurements and atomic force microscopy (AFM) analysis. Finally, the mechanical properties of chemical cross-linked hydrogels were estimated through swelling ratio measurements with Flory-Rehner calculations.

#### 5.2.5.1 Surface characterization

For 2D samples preparation, SZ2080 was spin-coated (800 rpm x 60s; 1500 rpm x 30s and 1800 rpm x 10s) on squared glass slip (20mm x 20mm x 0.16mm). Then, surfaces were left at 104°C for the pre-baking step (6.2.2.1). After 1 hour, flat surfaces were UV-irradiated ( $\lambda = 365 \text{ nm}$ ;  $100 \text{ mW/cm}^2$ ) for 5 minutes in nitrogen atmosphere

#### 5.2.5.2 Optical Contact Angle (OCA)-surface wettability

The wettability of hydrogel coated SZ2080 surfaces was study performing contact angle measurements using an optical contact angle system (OCA-15-Plus, Dataphysics, Germany) equipped with a CCD camera and with a 500  $\mu\text{l}$ -Hamilton syringe to dispense liquid droplets. Measurements were made at room

temperature by means of the sessile drop technique with dedicated software (SCA 2.0) determining the contact angle based on the Young Laplace method fitting. At least five measurements were performed at different places on each sample and results were averaged. Ultra-pure water (HPLC grade, Sigma-Aldrich) was used as probe liquid and the delivered volume was 1  $\mu\text{l}$  with 0.5  $\mu\text{l/s}$  as dispense speed.

### 5.2.5.3 Atomic Force Microscopy (AFM) analyses for surface topography

Atomic force microscopy (AFM) topographic images of the SZ2080 hydrogel functionalized surfaces were obtained using a NSCRIPTOR™ DPN® instrument (NanoInk, USA) operating in tapping mode with a scan rate of 0.5 Hz/s. The measurements were conducted in air on several areas of the surfaces (10  $\mu\text{m}$  x 10  $\mu\text{m}$ ) using a standard ACT probe (AppNano, Santa Clara, CA, USA) with the normal resonance frequency of 300 kHz and a nominal spring constant  $k_c = 40$  N/m. Nano-Rule+™ 2.0 software (Pacific Nanotechnology) was used for processing images analysis and calculating the topographical parameters average  $R_a$  and root mean square surface roughness  $R_q$  directly by the instruments.

$$R_a = \sum_{n=1}^N \frac{|z_n - \bar{z}|}{N}$$

$$R_q = \sqrt{\frac{\sum_{n=1}^N (z_n - \bar{z})^2}{N}}$$

All the samples were analyzed after three days of immersion in deionized water to remove unattached material.

#### 5.2.5.4 Microscopy characterization

Microscopy analyses were implemented in order to study the morphological features of the hydrogels coating and evaluate the efficiency of the different grafting strategies in homogeneously functionalizing the three dimensional structures without affecting their porosity.

A BX60 Olympus was used for optical microscopy (MO). For environmental scanning electron microscopy (ESEM), a ZEISS EVO 50® EP (extended pressure) was used. This instrument works in a continuous vacuum pump up to 3000 Pa, and allows the differentiation of the vacuum degree between the filament chamber and the sample holder chamber thank to a valve system. The electron source is a LaB6 nanocrystal. Electrons are accelerated by a potential difference of 20kV, and the primary beam has an intensity of 250 pA. Analyses were performed with a pressure in the range of  $10^1 \div 10^2$  Pa using the air conductivity avoiding sample metallization.

#### 5.2.5.5 Hydrogel mechanical characterization

Swelling experiments following the Flory-Rehner theory<sup>33</sup> were conducted to estimate the degree of hydrogels swelling which is strictly correlated to the cross-linked network density and to their mechanical strength<sup>34,35</sup>. The extent of swelling  $q_M$  was calculated by dividing the equilibrium-swollen gel mass ( $W_s$ ) by the dried gel mass ( $W_d$ ), both measured through thermogravimetric analysis (TGA, Q500, TA Instrument). Particularly, few milligrams of hydrogel ( $W_s$ ) were collected from the functionalized niche surfaces, placed in the TGA weighing pan and slowly heated at 50°C fixed-temperature until a constant mass ( $W_d$ ) was achieved. The cross-link density  $\nu = \rho_p/M_c$  was then determined by applying an expression of the Flory-Rehner equation approximated for networks with low degrees of cross-linking swollen in good solvent:

$$q_e^{5/3} \simeq \frac{M_c}{\rho_p V_1} \left( \frac{1}{2} - \chi \right)$$

Where  $M_c$  is the average between cross-links,  $V_1$  is the molar volume of the

solvent (18 cm<sup>3</sup>/mol for water),  $\rho_p$  is the density of the dry polymer (1.229 g/cm<sup>3</sup>),  $\chi$  is the Flory polymer-solvent interaction parameter estimated to be 0.473<sup>19</sup> and  $q_e$  is the volumetric swelling ratio determined from  $q_M$ <sup>36</sup>:

$$q_e = 1 + \frac{\rho_p}{\rho_s} (q_M - 1)$$

Being  $\rho_s$  the density of water.

Finally, through the rubber elasticity theory<sup>37</sup> the hydrogels Young's modulus  $E$  was estimated assuming a 0.5 Poisson's ratio<sup>38</sup>:

$$E = 2G(1 + \nu)$$

Where  $G$  is the shear modulus calculated fitting with Flory-Rehner cross-link density  $\nu$  data the following relationship:

$$\nu = \frac{G}{RT}$$

Being  $R$  the gas constant (8.314 J/mol K) and  $T$  the temperature at which the modulus was measured, which was set at 310.15 K to mimic physiological conditions of the human body.

## 5.2.6 Cellular tests

Stem cells behavior was studied on functionalized 2PP scaffolds with cell cultures, which were performed at the Laboratory of Biological Structures Mechanics (LaBS). The study was conducted in two steps and involved seeding of two different types of cells onto coverslip glass each supporting three hydrogel-coated 2PP niches arranged in a triangular pattern (6.2.1.2). Firstly, immortalized cells were seeded to evaluate general aspect of biocompatibility. Then, the behavior of primary mesenchymal stem cells (MSCs) was evaluated in terms of ability to differentiate towards the osteo-chondral lineage. Unless otherwise specified, chemicals and chemofluorescent markers were purchased from Sigma-Aldrich; immunofluorescence markers from Thermo Scientific; cell culture media and supplements from Euroclone; and cell culture plastics from Corning.

### 5.2.6.1 Immortalized cells and hydrogels biocompatibility

An immortalized cell line was used to evaluate aspects of biocompatibility of the niche substrates, including cell viability/cytotoxicity, cell adhesion and their morphological compatibility. MG63 human osteosarcoma cell line (86051601-1VL, Sigma-Aldrich) were resuscitated and expanded in minimum essential medium (MEM) supplemented with 2 mM glutamine, 10% fetal calf serum (FCS), 1% non-essential amino acids (NEAAs), and 1% penicillin/streptomycin, under 5% CO<sub>2</sub> atmosphere at 37°C. Immortalized cells were cultured in standard flasks until semi-confluence.

### 5.2.6.2 Mesenchymal stem cells differentiation behavior

Primary rat MSCs were used to study cell viability, adhesion, migration, proliferation and differentiation on the hydrogel-coated 2PP niche substrates. Bone marrow was obtained from 2-month-old Lewis or Sprague-Dawley rats. Rats were sacrificed and femurs and tibias were aseptically removed. Bone marrow was flushed from the shaft of the bones with  $\alpha$ -MEM medium

(Invitrogen-Gibco) containing 5% of FCS plus 1% penicillin/streptomycin and then filtered through a 100- $\mu\text{m}$  sterile filter to produce a single-cell suspension. MSCs were recovered from bone marrow by their tendency to adhere tightly to plastic culture dishes. Filtered bone marrow cells were plated in  $\alpha$ -MEM supplemented with 20% FCS and 1% penicillin/streptomycin and allowed to adhere for 24h. Non-adherent cells were then removed. The medium was changed regularly every three days until confluence. Adherent cells were detached by trypsin-EDTA (0.5 to 0.2 g/ml, Invitrogen), counted and cryo-preserved in  $\alpha$ -MEM supplemented with 30% FCS and 5% dimethyl sulfoxide (DMSO) until use. After resuscitation, cells were plated and cultured until semi-confluence in standard flasks in complete medium. The animal protocols used in this study comply with the institutional protocols for ethical currently in force.

#### 5.2.6.3 Substrate preparation and cell seeding

For cells seeding, cells were trypsinized and counted. The hydrogel coated 2PP niches (from here on called "samples") were washed thoroughly, kept for 12 hours in deionized water, disinfected for 12 hours in 70% ethanol, washed repeatedly in sterile deionized water, dried and UV-sterilized. Each sample was positioned in a 24 plates ultra-low attachment multi-well (Costar 3473, Corning). MG63 cells and MSCs were suspended in their proper medium and seeded directly in the wells at a density of 20,000 cells/cm<sup>2</sup>. MG63 cells were incubated for 3 days, while MSCs for 14 days, with medium freshly replaces every day.

#### 5.2.6.4 Morphological examination

Both morphological and adhesion cellular aspects were evaluated by microscope imaging. The cell-populated samples were imaged in their wells in phase contrast every day using an inverted phase contrast/fluorescence microscope (IX70, Olympus) equipped with a cooled high-resolution color video camera (4083.CL3, Optika).

For scanning electron microscopy (SEM), the cellularised samples were fixed in

the wells in 1.5% glutaraldehyde and 0.1 M sodium cacodylate and dehydrated in a graded series of ethanol. The samples were extracted from the wells, air dried, glued onto SEM stubs and gold-coated in a vacuum ion coater. All observations were carried out at 17.5 kV using an EVO 50 extended Pressure system (Carl Zeiss).

#### 5.2.6.5 Biochemical assays: Live/Dead and MTT assay

Two standard colorimetric methods were implemented to assess cell viability: the ethidium/calcein assay for membrane integrity assessment and a mitochondrial dye inclusion (MTT) assay for metabolic activity assessment.

The cellularised samples were marked in the wells using a live/dead viability/cytotoxicity kit (L3224, Invitrogen-Molecular Probes), in which the polyanionic dye calcein is retained within live cells producing green fluorescence, and ethidium homodimer-1 (EthD-1) enters cells with damaged membranes and binds to nucleic acids, producing a red fluorescence. The samples were incubated in 2- $\mu$ M calcein and 4- $\mu$ M EthD-1 solutions for 45 min and imaged directly in the wells.

The cell metabolic activity was assayed using the MTT assay (3-(4,5-dimethylthiazol-2-yl)-2,5-diohenyltetrazolium bromide, Sigma Chemical). While incubating samples with 500  $\mu$ g/ml MTT solution for 4 hours, the MTT yellow tetrazole was reduced to insoluble formazan crystals in living cells. Subsequently, MTT solution was removed and samples were suspended in dimethyl sulfoxide (DMSO) to solubilize the converted die. The absorbance of the colored solution obtained by dye conversion is proportional to the number of viable cells and was quantified at 570  $\div$  630 nm with a spectrophotometer (Infinite Pro 200, Team).

The DNA content was assessed on the cell lysate. The culture medium was replaced with deionized water and culture plate containing the cellularised samples was frozen at -80°C and incubated at 37°C repeatedly. The DNA absorbance was measured at 260 nm directly on the cell lysate with a spectrophotometer (Infinite Pro 200, Tecan) equipped with a NanoQuant Plate.

### 5.2.6.6 Fluorescence staining and confocal microscopy

For confocal microscopy, cell-populated synthetic niches were fixed in the wells in paraformaldehyde 2%, permeabilised with Trion 0.2%, blocked with 3% bovine serum albumin (BSA) plus 10% FCS to avoid unspecific labeling, and fluorescently marked. The cell nuclei/DNA were marked in blue by incubation with 4',6'-diamino-2-phenylindole dihydrochloride (DAPI) in solution at 10 µg/ml. The cytoskeletal actin was marked in green using FITC-conjugated phalloidin. Cell proliferation was studied by detection of the Ki67 antigen, which is expressed by cells in all the phases of division cycle, using Cy3 (red)-conjugated mouse anti-human Ki67 monoclonal antibody (NCL-Ki67-MM1, Novocastra). Cell differentiation was studied by detection of Collagen type I, Collagen type II and Osteocalcin, whose expression by cells is considered a first marker of differentiation towards the osteo-chondral lineage. Collagen type I, collagen type II and Osteocalcin were immunolabeled with primary antibodies and then marked in red using Cy3-conjugated secondary antibodies. MG63 cells expressing all the investigated markers were used as positive controls for all the immunostaining procedures<sup>39</sup>. Image acquisition and 3D reconstruction were performed at 15x and at 63x with a laser confocal microscope (LSM 510 Meta, Carl Zeiss).

### 5.2.6.7 Statistical analysis

Depending on the cell culture, respectively at 6 and 14 culture days, cell count was performed on images acquired in fluorescence on the green/red-labeled samples and DAPI-labeled samples, in transmission by an inverted microscope. By this method, all the cell nuclei present on the sample were visualized in projection on the images, instead of what happens in confocal acquisitions where only the projection of a limited sample volume above the cell-populated coated glass surface is visualized. MG63 cell viability was assessed visually by counting viable (green) and not viable (red) cells in square regions of 100 x 100 µm<sup>2</sup>. MSCs count was assessed visually on the DAPI-marked cells by counting the cell nuclei

in square regions of  $100 \times 100 \mu\text{m}^2$ . Cell density was obtained by dividing the cell count of each region by the area of the square region. Results of the cell counts were assigned to experimental groups based on the coating type. For each coating type, cell counts were assigned on the count location: i) coated glass (flat), ii) coated niche internal volume (niche).

For Collagen I-positive cells quantification, DAPI-labeled (blue) and TRITC-labeled (red) fluorescence pictures were converted to grayscale, filtered and manually thresholded. To avoid an overestimation of the fluorescent signal, niches were subtracted before converting into binary format. Then, the overall nuclei area and collagen area were measured on the resulting binary pictures ( $n = 3$  pictures for each sample). Cells positive to Collagen-I, grouped according to the above-mentioned count location, were calculated as the percentage ratio between the collagen area and the nuclei area. The groups were compared using one-way analysis of variance (ANOVA) for independent samples. Pair-wise comparisons among groups were determined with the Tukey HSD test, or with the Student t-test for independent samples. Differences were considered to be significant if  $p < 0.05$ .

## 5.3 Results and discussion

### 5.3.1 2PP Scaffold fabrication

Synthetic niches were fabricated at the Institute for Photonics and Nanotechnology (IFN)-CNR exploiting two-photon polymerization (2PP) technology. 2PP paved the way to the realization of complex 3D polymer scaffolds with micro- and nano-structures controlled at the cell scale ( $5 \div 10 \mu\text{m}$ ) and with geometrical resolution down to  $0.1 \mu\text{m}$ . The optimization of processing conditions (scan speed and laser power) allows for rapid prototyping of arbitrary architectures together with a good mechanical stability. In the present study, a novel Yb-based writing laser was used and an ideal processing window was found to be at 200-kHz repetition rate and 1.9-nJ pulse energy with 1-mm/s scan speed<sup>14</sup>. Synthetic niches were fabricated with a graded niche geometry, which was selected as the one most favoring spontaneous MSC homing and differentiation<sup>15</sup>. Particularly, the graded geometry allowed easy penetration of the cells from the larger central pores and a higher surface-to-volume ratio at the borders of the scaffold. Moreover, the small 2- $\mu\text{m}$  gaps resulting from the four outer confinement walls surrounding the 3D structures, enabled nutrients to pass through the cells in the scaffold but prevented cells within the internal volume from escaping through the sides. Each sample was composed of a circular cover slip with three niches arranged centered in a triangular pattern at a relative distance of  $200 \mu\text{m}$ . This distance was chosen for a dual purpose: first, it allowed to align the structures with the 500- $\mu\text{m}$  width polymeric channel used for scaffold functionalization processes; and secondly it facilitated a homogeneous hydrogel coating of the areas in between the structures. 3D scaffolds were fabricated in the SZ2080 photoresist with 1% concentration of Irg photoinitiator. This hybrid organic-inorganic material silver-zirconium sol gel was selected from ORMOSILs family due to its 2PP easy processability and its biocompatibility. This was assessed with cell tests, performed at the Laboratory of Biological Structure Mechanics (LaBS), which also revealed that SZ2080 is

sufficiently stable to give mechanical support to cells till they managed to synthesize their own physiologic extracellular matrix.

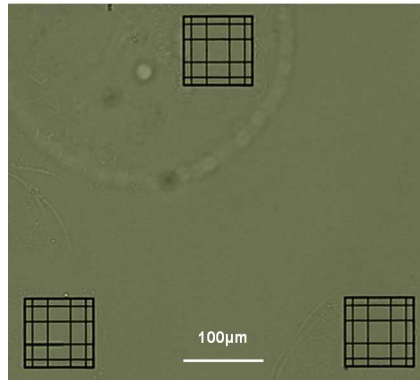


Figure 12. MO image of 2PP scaffolds arranged in a triangular pattern.

Moreover, the dual-cure mechanism of the photoresist minimizes the shrinkage during 2PP enabling the fabrication of high-resolution 3D-free standing structures with good mechanical stability. The magnified view of the structures showed the perfectly graded geometry of the 2PP structure.

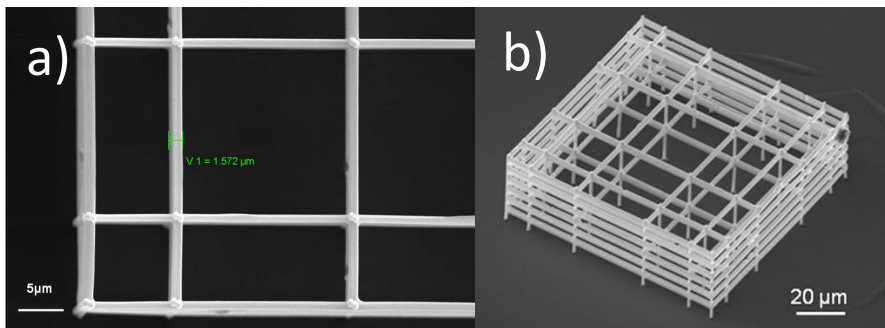


Figure 13. a) Detailed SEM image of a graded pore scaffold and b) SEM image of a 2PP uncoated S22080 structure reproducing the graded-pore geometry exploited.

Instead, the Irg-based photoresist was used because of its biocompatibility<sup>40</sup> and its reduced auto-fluorescence signal which do not interfere in the characterization of the fluorescent markers for cell proliferation.

### 5.3.2 Hydrogel coating

Due to their biocompatibility and wide range of physical and biological properties, hydrogels were considered as suitable coating material to engineer 2PP structures. Particularly, hyaluronic acid- (HA) and gelatin-based hydrogels were modified via cross-linking and conjugation reactions to tailor their chemical and mechanical properties. The aim was to tune the mechano- and chemical-transduction signaling that cells can sense.

Physical, covalent and photochemical interactions at the interface between SZ2080 surfaces and the hydrogels were investigated to graft the different gels matrices. Some were directly grafted to the photoresist, whereas in other cases an intermediate linker was used. A stronger bonding, based on covalent interactions, as for GMHA and Gel-SH, should better avoid the coating detachment eventually caused both by compressive forces that cells induce while adhering on the substrates and by the dynamical swelling behavior of the hydrophilic networks<sup>41</sup>.

The morphology and the stiffness of the coated substrates, mainly influenced by the different cross-linking processes implemented, were investigated to understand their relation with stem cells behavior. Following paragraphs deals with the results obtained from coating surface, mechanical and microscopy characterization.

#### 5.3.2.1 Surface characterization: water contact angle

Static contact angle measurements were performed on functionalized 2D SZ2080 surfaces to study the effect of the hydrogel coating on the change in wettability of the surfaces. The hydrophobic/hydrophilic behavior of the functionalized surfaces could be related to the real presence of the hydrogels macromolecules on the surfaces thus proving the efficiency of the coating processes implemented. Therefore, using Ultra-pure water as test liquid, the contact angles were measured for a bare SZ2080 surface and for each functionalization step of each coating process.

Table 1. Contact angles for 2D SZ2080 surface functionalized exploiting the chemisorption process.

<i>SZ2080</i>	<i>Air Plasma</i>	<i>HA : DVS</i>
$72.3^\circ \pm 0.9^\circ$	$19.5^\circ \pm 5.6^\circ$	$17.9^\circ \pm 3.4^\circ$

The contact angles values measured for each step involved in the chemisorption process are displayed in Table 1. Air-plasma treated SZ2080 surfaces are hydrophilic with contact angles decreasing from approximately 73° to about 20° thus assessing the presence of hydroxyl groups necessary for the hydrogel grafting. HA+DVS functionalized surfaces also showed hydrophilic behavior with contact angles of about 20°. However, after 12 hours the SZ2080 air-plasma treated surfaces partially recovered their static angles (about 50% of the value measured for bare SZ2080), probably due to the reorientation of the polar groups from the surface to the bulk and to the condensation of the surface hydroxyl groups. This recovery phenomenon was not observed for the HA:DVS coating, which showed very hydrophilic behavior even after several days, thus proving the efficient grafting of HA macromolecules onto surfaces.

Table 2. Contact angle measurements for 2D SZ2080 surface coated with photocross-linked GMHA.

<i>SZ2080</i>	<i>APMES</i>	<i>GMHA</i>
$72.3^\circ \pm 0.9^\circ$	$69.9^\circ \pm 12.5^\circ$	$26.3^\circ \pm 4.4^\circ$

As shown in Table 2, contact angles for the photografting process were measured after the air phase silanization step with (3-Acryloxypropyl) methyltrimethoxysilane and at the end of the whole process. The hydrophilic behavior of the surfaces demonstrates the presence of GMHA.

Table 3. Contact angle measurements for 2D SZ2080 surface coated with Gel-SH and cross-linked with PEGDA.

<i>SZ2080</i>	<i>Polydopamine</i>	<i>Gel-SH</i>	<i>Gel-SH+PEGDA</i>
$72.3^\circ \pm 0.9^\circ$	$40.2^\circ \pm 4.2^\circ$	$33.9^\circ \pm 3.2^\circ$	$69.2^\circ \pm 7.2^\circ$

Water contact angles were measured for both polydopamine and thiolated-modified coatings onto SZ2080 (Table 3). Both the PD and the uncross-linked Gel-SH coatings rendered the surfaces more hydrophilic, which was indicated by

a decrease in the average contact angle. Values obtained for polydopamine were in accordance/agreed with those from literature<sup>31,42,43</sup>. Interestingly, coating of thiolated gelatin chemically cross-linked with PEGDA resulted slightly less hydrophilic than HA coatings. This different wettability behavior could be related to a different chemistry of the two hydrogels matrices. In fact, while HA is mainly composed of disaccharides gelatin has a strong composition in protein.

Table 4. Contact angle measurements for 2D SZ2080 functionalized with HA-DA.

<i>SZ2080</i>	<i>HA-DA</i>
$72.3^\circ \pm 0.9^\circ$	$30^\circ \pm 6.8^\circ$

As for GMHA, dopamine-conjugated HA coatings were highly hydrophilic compared to the bare SZ2080 surfaces (Table 4). Values obtained agreed with those from literature<sup>20</sup>.

### 5.3.2.2 Surface characterization: Atomic Force Microscope (AFM)

AFM images were obtained for all hydrogels coating in order to study how the functionalization processes influence the topography and the homogeneity of the surfaces. These confirmed that surface roughness substantially increased after all the hydrogels coating. The root mean square and average roughness were then calculated for each conditions using 10  $\mu\text{m}$  x 10  $\mu\text{m}$  images. Data are showed in Table 5.

Table 5. Summary of surface roughness values obtained for bare and functionalized SZ2080 substrates

<i>Sample</i>	<i>SZ2080</i>	<i>+ HA:DVS</i>	<i>+ GMHA</i>	<i>+ Gel-SH-PEGDA</i>	<i>+ HA-DA</i>
Average Roughness $R_a$ [nm]	0.47	192.16	0.76	19.65	0.96
Root Mean Square Roughness $R_q$ [nm]	1.89	256.83	1.36	44.56	2.22

Surface roughness values obtained for both HA:DVS and Gel-SH:PEGDA coatings were 1÷2 orders of magnitude higher compared to those from bare SZ2080 and to those measured for GMHA and HA-DA coating processes.

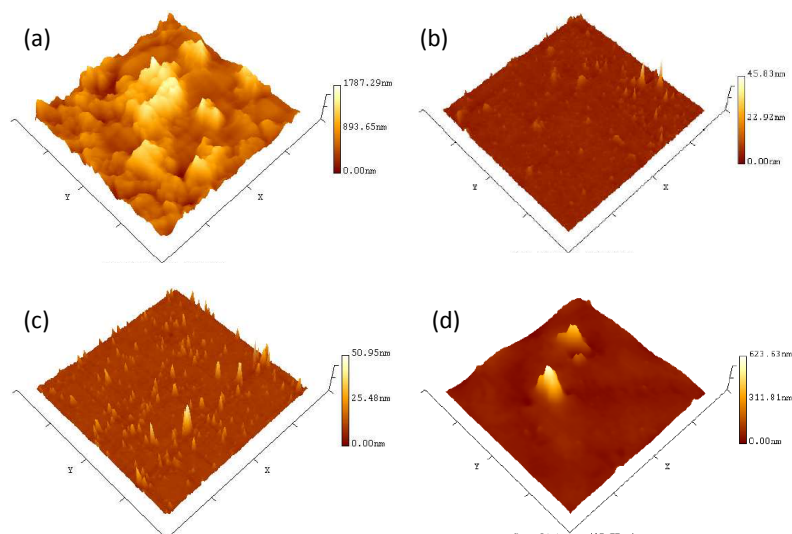


Figure 14. 3D topographical AFM scan obtained for 2D SZ2080 surfaces functionalized with HA:DVS (a); GMHA (b); HA-DA (c); and Gel-SH:PEGDA (d) hydrogels coatings.

Probably, the cross-linking process involving the addition of an external cross-linking agent (DVS and PEGDA respectively) is the main cause of this increase in surface roughness<sup>44</sup>. It is also important to consider that HA:DVS hydrogels grafting, which exploited physical interactions at the interfaces of the two materials, could lead to non-specific adsorption resulting inefficient due to an excess of material deposition. Values obtained for GMHA and HA-DA films agreed with those from literature<sup>20,45</sup>, as the same for Polydopamine coatings which were 1.63 nm and 7.3 nm<sup>32</sup>.

### 5.3.2.3 Microscopy characterization of 3D hydrogel functionalized niches

Optical microscope (MO) and environmental scanning electron microscope (ESEM) analyses were performed on the 3D hydrogel-coated 2PP niches to evaluate the grafting efficiency of the different processes implemented. Exploiting the microfluidic systems, the hydrogels solutions were forced to penetrate within the internal volume of the synthetic niches otherwise

impossible with static methods. The flow rate was experimentally set at  $3 \mu\text{l}/\text{min}$  to uniformly filling the microporous structures removing unreacted material but avoiding samples collapse eventually due to high shear stresses. Homogeneous coating of the external walls was achieved without affecting scaffold geometry with all the processes as attested by both MO and ESEM top view images (Fig.15 and 16). A thin hydrogel layer was deposited on the  $\mu$ -structures with the scaffold rods resulting thicker after functionalization processes. Where the coating could not be directly visualized by ESEM analyses, it is likely because a very thin layer of macromolecules was grafted. Moreover, it is important to consider that these types of analyses are performed in low-pressure conditions in an ultra-dried chamber, for sure damaging the soft hydrogels coating. In order to check the presence of the coating inside the structures, ESEM analyses were performed tilting the sample holder of  $45^\circ$ , not directly visible from ESEM top views (Fig.17).

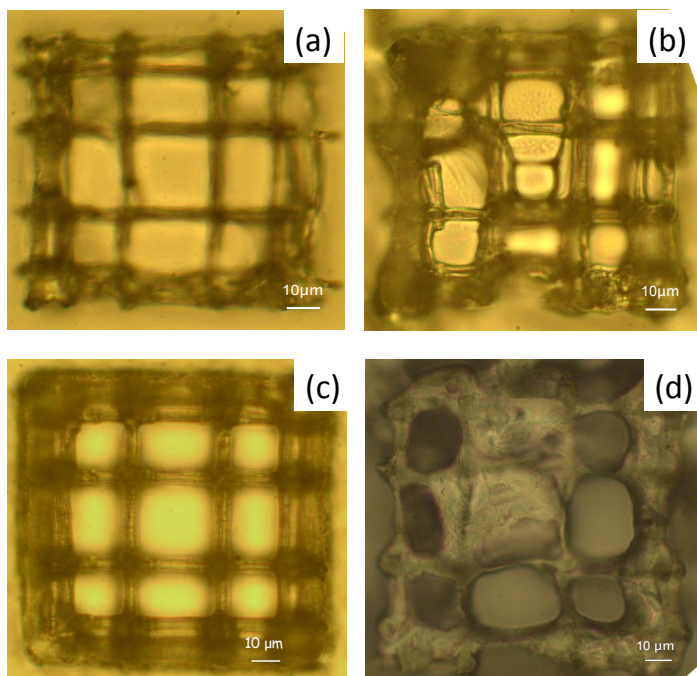


Figure 15. MO images of a 3D scaffold functionalized with HA:DVS (a); GMHA (b); HA-DA (c) and Gel-SH (d) hydrogels coating

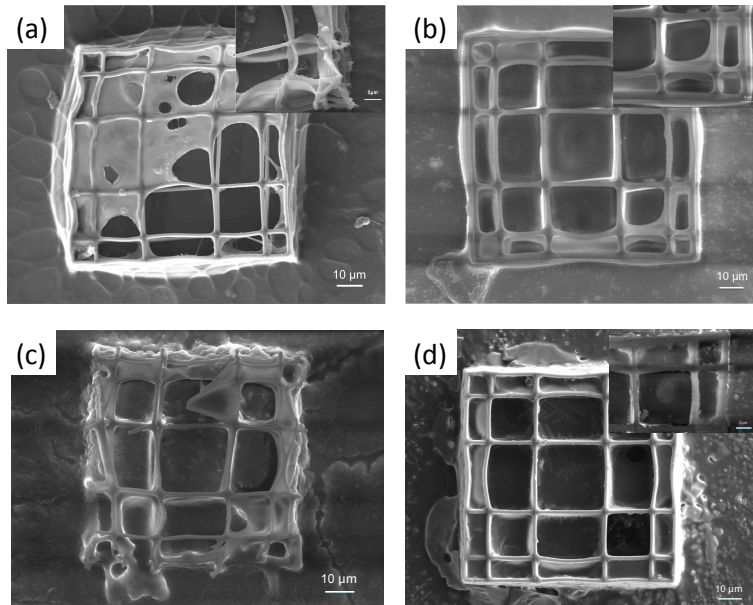


Figure 16. SEM images of HA:DVS (a); GMHA (b); HA-DA (c) and Gel-SH (d) coated scaffolds. Top view.

It was verified that even the internal niches volumes were functionalized with little effect on the overall  $\mu$ -porosity considered fundamental for cell proliferation and growth. Major problems were encountered in avoiding the obstruction of the 2- $\mu$ m small gaps formed by the outer walls confinements. In fact, some hydrogels conglomerates, probably originating from a non-specific adsorption, were formed to the sides of the scaffolds, thus altering their original geometry. It is worthwhile noticing that the coating process is not specific to the microscaffolds, but also covers the surrounding glass surfaces in between the structures. In fact, it is technologically very challenging to confine the coating to the microstructures (90x90x30  $\mu$ m). Therefore, each 2PP-coated sample shows a 2D coated-glass region and 3D coated niches, from here on called “flat” and “niche” respectively, and SCs behavior was investigated in the two different regions.

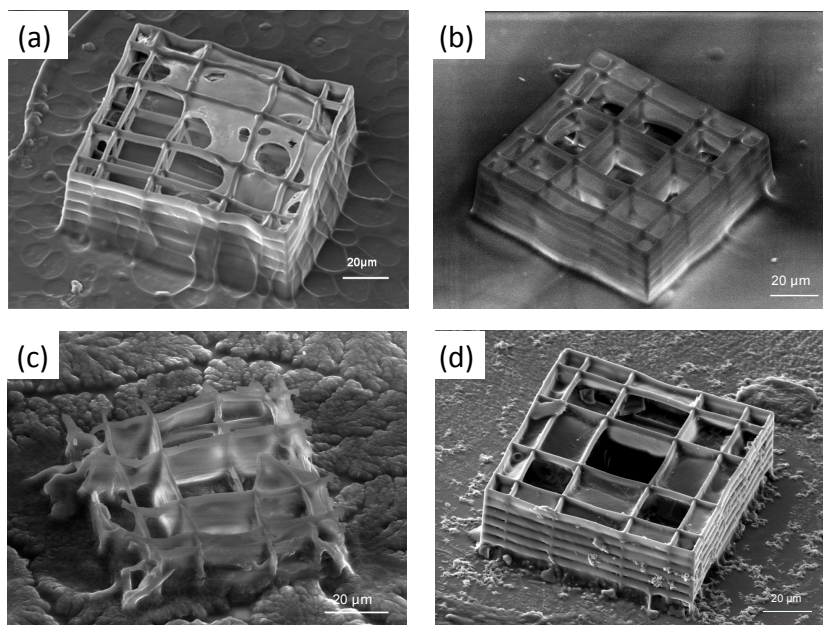


Figure 17. SEM images of HA:DVS (a); GMHA (b); HA-DA (c) and Gel-SH (d) coated scaffolds tilted at  $45^\circ$  in order to check the coating inside. It is possible to see even some material grafted on the bare glass in the area in between the structures.

#### 5.3.2.4 Mechanical properties of the coatings

Depending on the process exploited, different cross-linking conditions parameters were chosen according to literature to fine-tune the gels stiffness and to obtain elastic moduli ranging in the order of physiological values. Particularly, for HA:DVS hydrogels the main parameters were DVS-content, set at 10-fold molar excess respect to HA, and curing time (12h)<sup>35</sup>. Whereas, photoinitiator I2959 and VP contents for GMHA and thiol:C=C double bonds ratio for Gel-SH samples were the key parameters to be considered in hydrogels mechanical properties tuning.

To establish whether these hydrogels cross-linking formulations addressed or not gels stiffness to range in the desired values, the mechanical characteristics of 2PP-coated samples were indirectly evaluated measuring the extent of hydrogels swelling  $q_M$  through TGA analyses implemented on few milligrams of hydrogels sampled from the functionalized 2PP surfaces. TGA data were then used to fit an approximate expression of the Flory-Rehner equation in order to calculate

hydrogels cross-link density, which is related to the elastic modulus through the rubber elasticity theory. Flory-Rehner calculations lead to elastic modulus values for hydrogels synthesized encompassing the range of physiological niches values (Table 6)<sup>46</sup>, and varying from 20 kPa for HA:DVS samples to 0.2 kPa for Gel-SH samples.

Table 6. Stiffness values experimentally estimated for the three chemical cross-linked hydrogels used to coat the artificial niche substrates

Gel Matrices	Young Modulus [kPa]
HA:DVS	21.6 ± 6.3
GMHA	1.17 ± 0.3
Gel-SH:PEGDA	0.23 ± 0.02

Therefore, it was possible to study the effect that tuning scaffold stiffness and varying hydrogel chemistry could have on MSCs behavior.

Swelling experiments and TGA analyses were not performed with HA-DA samples due to the fact that DA-conjugated chains were simply grafted to the scaffold surfaces but no covalent cross-linking procedures were studied.

Just temporary physical interactions could occur in the hydrogel, which would behave more as a viscous liquid with the viscous component prevailing on elastic one.

### 5.3.1 Cellular Tests

Cellular tests were performed on 3D hydrogels coated niches. First, aspects of biocompatibility, including viability and cytotoxicity of the coatings, were evaluated seeding immortalized cells. Subsequently, we investigated the influence that the different chemistry of the coatings HA- and gelatin-derived substrates, together with their different mechanical properties had on the behavior of mesenchymal stem cells in terms of proliferation and differentiation. As mentioned before (6.3.2.3), due to technological reasons and to the overall size of the microstructures, the coating process was not specific to the microstructures. The advantage arising from this non-selective coating consists

in the fact that it was possible to simultaneously observe on the same sample, cells adhering on the flat surface and cells adhering in the internal niche volume, while sensing the same substrate stiffness in each location of the sample.

#### 5.3.3.1 Biocompatibility of the hydrogel-coated niche substrates

Immortalized cells MG63 derived from the human osteosarcoma were seeded on the 2PP-coated engineered niches to evaluate aspects of biocompatibility such as cell adhesion to the substrates, their morphological compatibility, cell metabolic activity and cell viability.

Cell adhesion was evaluated studying cells morphology through scanning electron microscope analyses. SEM images show that MG63 cells proliferated in three days to confluence homogeneously on the flat-coated surfaces surrounding niches and subsequently invading their internal volumes by climbing the external confinement grids. The elongated-shape cells acquired is deeply indicative of an optimal adhesion to the underneath substrates (Fig.18 and 19).

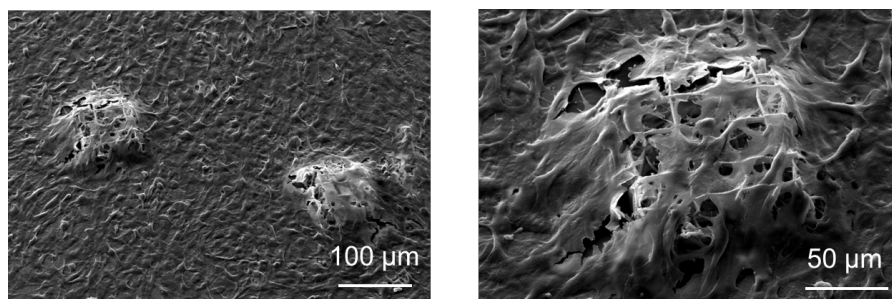


Figure 18. MG63 cells cultured on the GMHA-coated niche substrates at three culture days. Cells proliferated and migrated in the niches aggressively invading their internal volumes.

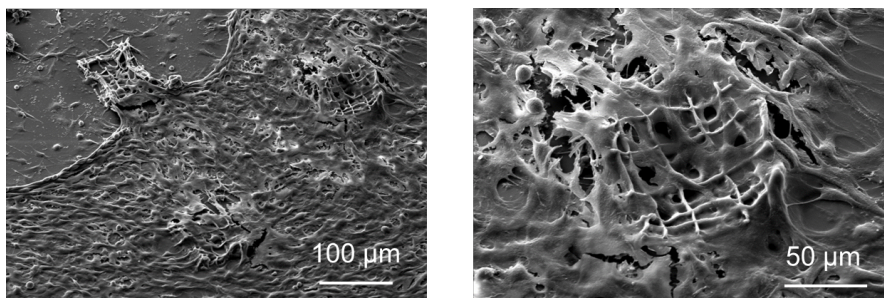


Figure 19. MG63 cells cultured on the Gel-SH coated niche substrates at three culture days.

Cell viability was assessed performing a Live/Dead assay in which live cells stained green whereas dead cells stained red. Phase contrast images (Fig.20a, 20c, 20e, and 20g) and the corresponding merged fluorescence (Fig.20b, 20d, 20f, and 20h) images are reported. While GMHA and Gel-SH coatings showed cell having adhered and proliferated rapidly almost all over the glass samples including the niches, HA-DVS coating showed a non-confluent cell monolayer. Poor cells growth and adhesion was reported also for HA-DA coating. Fluorescence Live/Dead images attested that most cells were viable in all the samples including the internal volume of the niches thus assessing the citocompatibility of the hydrogels coating materials. Few dead cells (stained in red) were detected on the external niche walls for GMHA and Gel-SH, and within large cell aggregates as those present in the HA:DVS substrates maybe due to the local cell density that affects cell viability. Nonviable cells were absent within the internal volume of the niches. Red fluorescence derived from scaffolds walls was due to the photoinitiator autofluorescence as previously explained (6.2.1.1). Viable cells were grouped according to their location into the sample (flat or niche) and visually quantified.

Cells in the coated niches are all viable (100%), whereas the percentage of viable cells anchored on the external walls and on coated-flat surfaces are resumed in the Table 7. Values were normalized to the total number of cell counted in a reference area ( $100 \times 100 \mu\text{m}^2$ ).

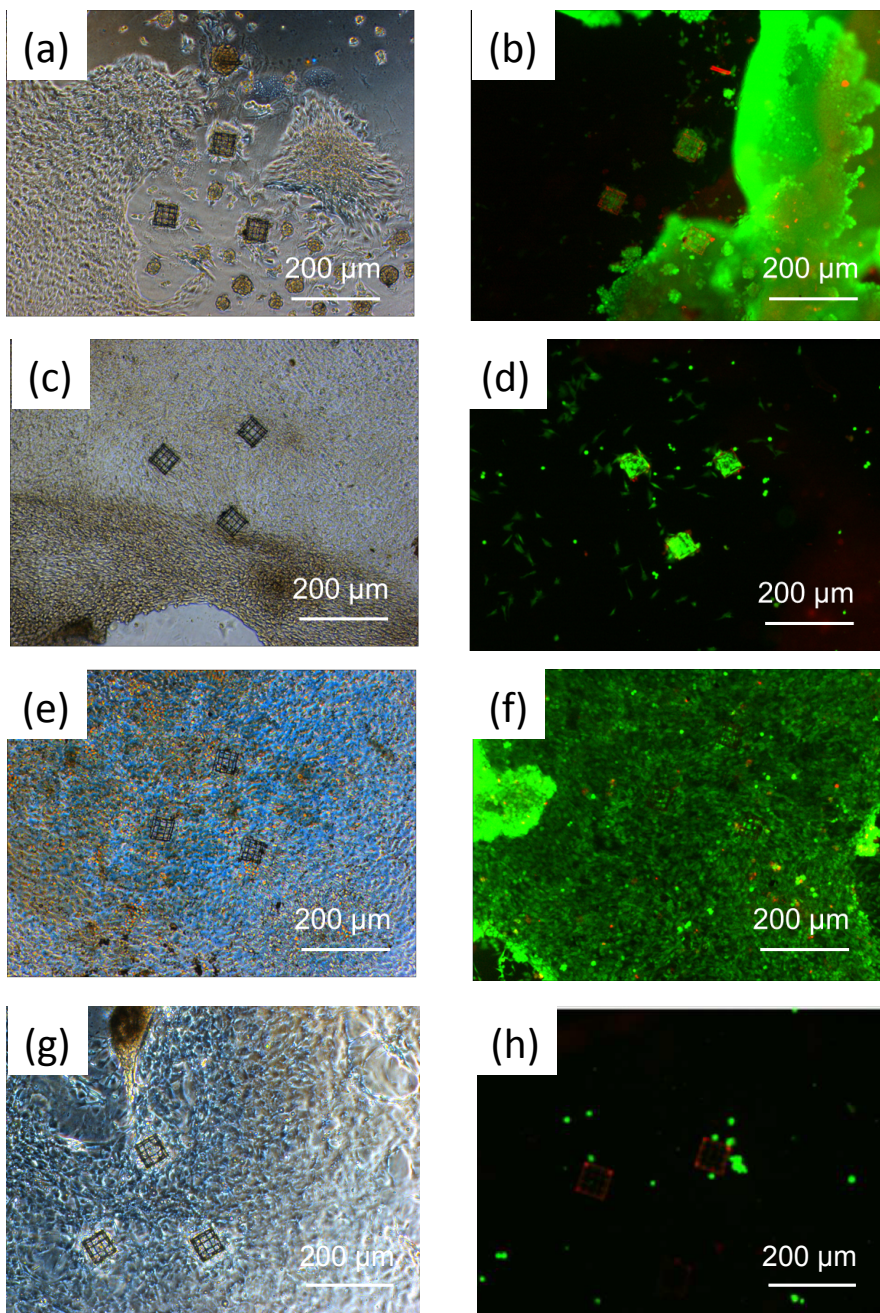


Figure 20. Results of the biocompatibility tests for hydrogel-coated niche substrates. Phase contrast (left) and fluorescence Live/Dead images (right) of cellularised niche substrates with HA:DVS (a and b), GMHA (c and d), Gel-SH (e and f), and HA-DA (g and h).

Table 7. Resume of the percentage of viable cells anchored on different areas of the samples.

Sample	% on external walls	% on coated-flat surfaces
HA:DVS	94.73 ± 4.12	90.16 ± 4.1
GMHA	84.20 ± 7.14	92.3 ± 5.4
Gel-SH:PEGDA	89.47 ± 10.2	86.1 ± 5.1

The diagram illustrating these percentages is displayed in Figure 21. In general, a good biocompatibility of the coated niches was observed. The fact that no cells were counted for HA-DA samples is not a consequence of coating possible cytotoxicity, as proved by its positive results of the MTT assay, which, as explained in the following, was performed to evaluate cell metabolic activity.

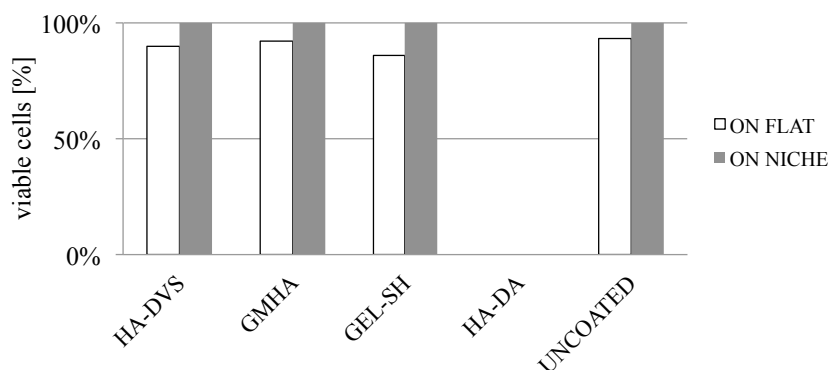


Figure 21. Diagram illustrating the percentage of viable cells normalized to the total number of cells counted in a reference area (100 x 100)  $\mu\text{m}^2$  grouped according to the location into the samples.

The absence of cells within the HA-DA niches could be explained taking into account its low mechanical properties, which could not contrast the force exerted by the high extent of swelling typical of hydrogels immersed in an aqueous solution. This swelling behavior could lead to HA-DA easy detachment from the underlying substrate inducing its dissolution in the aqueous culture media, thus provoking the detachment of cells onto its surface.

In the MTT assay, the mitochondrial dye (purple colored) is incorporated by metabolically active cells. Acquired images in bright field for HA:DVS, HA-DA and

Gel-SH coated samples (Fig.22a, 22c, and 22d respectively) showed an intense purple color both for cells adherent to the glass surfaces. Instead, GMHA coated sample showed metabolically active cells just in the outer areas of the glass, far from the structures. As for the HA-DA case, the negative result for GMHA is not a consequence of the cytotoxicity of the coating if we consider its positive previous results from Live&Dead assay, but is probably due to an excess of material deposition, which prevented cells from entering within the scaffolds.

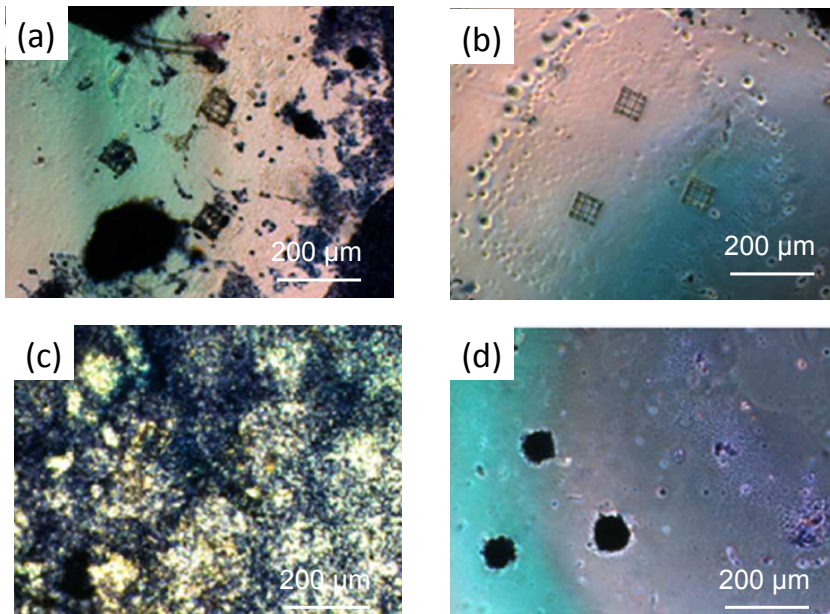


Figure 22. Phase contrast images of cells after MTT dye inclusion for HA-DVS (a); GMHA (b); Gel-SH (c) and HA-DA coated niches. Images show that the mitochondrial dye (in purple) was incorporated by metabolically active cells.

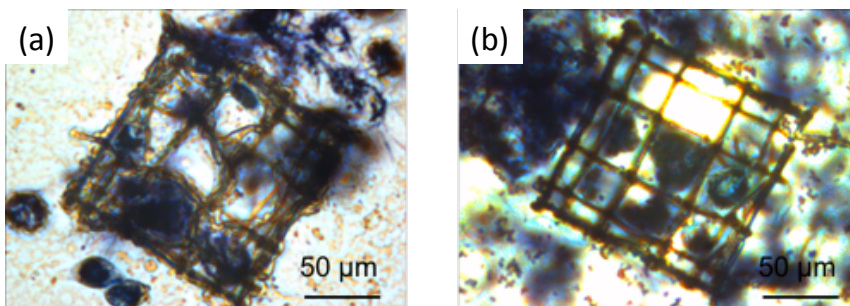


Figure 23. HA:DVS (a) and Gel-SH:PEGDA (b) coated niches showing metabolically active cells within the internal niches volumes.

Absorbance of the MTT converted dye was measured for 2PP-coated samples and for the uncoated glasses (referred to as flat glass) and average values, reported in Figure 24, did not show any statistically significant difference.

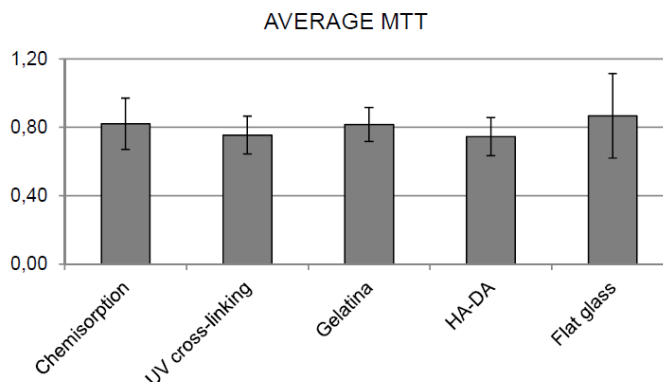


Figure 24. Average absorbance MTT values measured for cells seeded on hydrogels coated samples and for cells cultured on a flat control. No statistically significant differences were observed.

### 5.3.3.2 Stem cells differentiation behavior

Primary rat mesenchymal stem cells (MSCs) were exploited to study cell morphology, metabolic activity, proliferation and differentiation towards the osteo-chondral lineage when cultured for 14 days on hydrogel functionalized niches. Previous results, obtained with MSCs cultured for 21 days on bare 2pp structures, were used as benchmark<sup>15</sup>.

Extensive cell adhesion and colonization even within the internal volume of the niches was observed (Fig.25 a-f). MSCs adhered and proliferated on the glass surfaces where they spontaneously formed aggregates but also migrated towards the niches from the surrounding monolayer. After two weeks of culture, cells formed aggregates within 3D niche microstructures confirming that artificial niches tend to localize the formation of cells colonies in the glass area where they stand<sup>14</sup>. An extended cells agglomerate is formed on the top of the HA:DVS-coated structure (Fig.25a). For uncoated structures 21 days were needed to observe this phenomenon whereas in our case two weeks were enough.

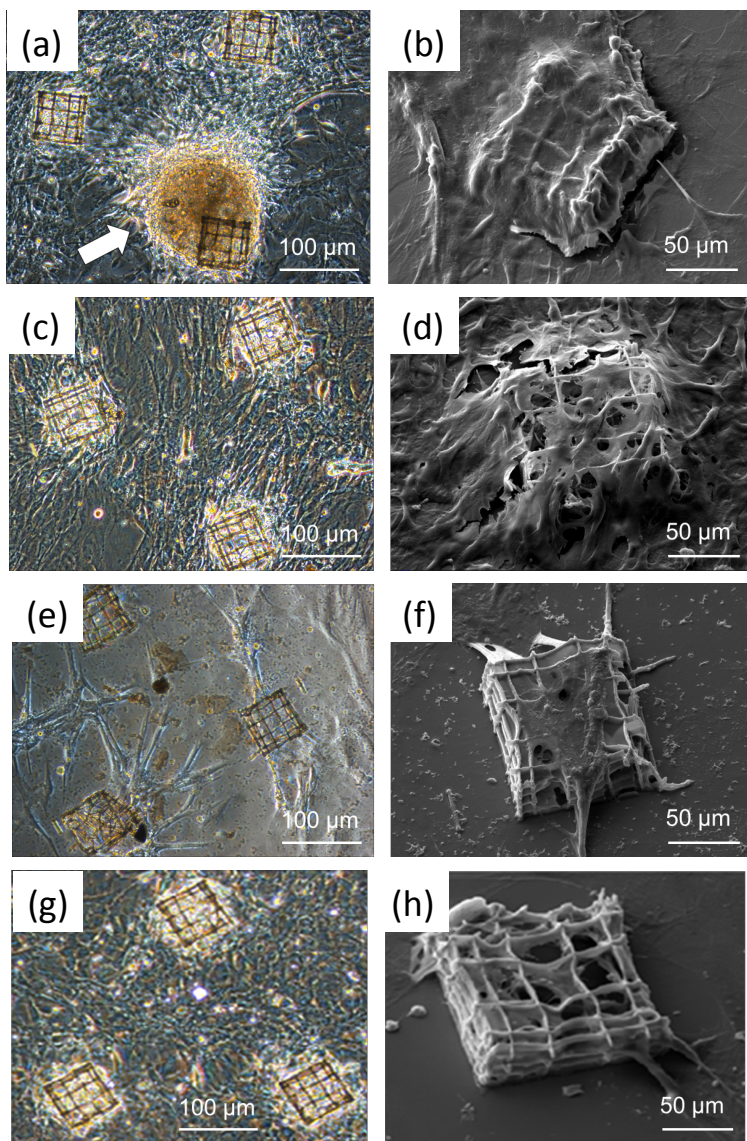


Figure 25. Phase contrast (left) and SEM images (right) acquired on MSC-seeded coated niches after 14 culture days. On the top of the HA-DVS coated niche (a) cells formed an aggregate (arrow); while small aggregates were observed for GMHA (c) and HA-DA (g). Few cells, deeply stretched (f), invaded the Gel-SH-coated niches (e).

Surprisingly, the cells within these agglomerates continue to proliferate raising up from the glass surface progressively forming the spherical aggregate. Moreover, it is important to consider that in order to obtain comparable cell proliferation rate for 2D cultures, it is usually requested the introduction of

chemical stimuli such as Fibroblast growth Factor – FGF. In GMHA and HA-DA coated substrates, cells established small aggregates within the niches (Fig.25c, 25d and 25e, 25f) whereas fewer cells, showing a really stretched morphology, were observed on the Gel-SH and HA-DA coated niches both on the flat and the internal volume.

Cell density for these samples was estimated for cells located in the coated surface surrounding the niches (from here on “flat”), and for cells inside the coated niches (“niche internal volume”).

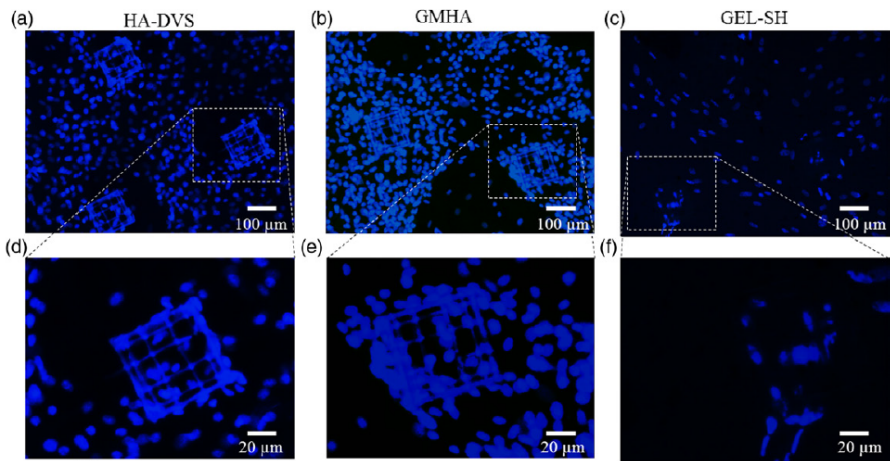


Figure 26. DAPI-labeled pictures of the coated samples at low (a-c) magnification and (d-f) higher magnification for HA:DVS (a and d), GMHA (b and e) and Gel-SH (c and f) coated samples.

It was measured visually on the DAPI-labeled pictures (Fig.26) by counting cells over comparable areas of  $100 \times 100 \mu\text{m}^2$ . Values are reported in Table 8 and clearly displayed in the graph in Figure 27.

Considering each sample singularly, cell density values were higher for coated niches than on coated flats thus underlining the homing behavior of the MSCs, which tend to proliferate in a 3D environment, and attesting the primary role of the microarchitecture. Making comparison among all samples, cell density values did not significantly differ from those estimated for all the colonized glass. Values for uncoated niches were the highest but it is important to take into account that data were measured after 21 days of culture instead of 14 as for the coated

structures. Moreover, the presence of the swelled hydrogel films could have a little effect on the overall porosity of the niches thus affecting cell spreading within their internal volumes.

Table 8. DAPI-labeled cells counted for each samples over comparable areas of  $100 \times 100 \mu\text{m}^2$ . Counting were estimated for flat-coated areas and niches-coated areas.

Sample	Flat $n^\circ\text{cells}/(100 \times 100 \mu\text{m}^2)$	Niche internal volume $n^\circ\text{cells}/(100 \times 100 \mu\text{m}^2)$
HA:DVS	$7.89 \pm 2.37$	$13.99 \pm 2.14$
GMHA	$6.57 \pm 2.98$	$13.58 \pm 1.91$
Gel-SH:PEGDA	$3.36 \pm 2.16$	$6.17 \pm 2.37$
HA-DA	$4.35 \pm 1.04$	$12.34 \pm 1.10$
Uncoated niche	$4.77 \pm 2.02$	$16.77 \pm 2.91$

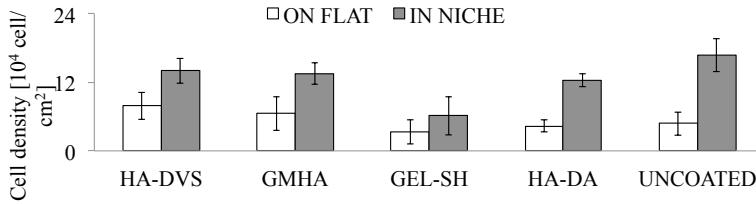


Figure 27. Cell density calculated for flat-coated surfaces and for niche internal volume. On flat area, higher values were observed in HA-coated surfaces, whereas for coated niches, slightly higher cell density was obtained with uncoated samples.

On the contrary, the lowest cell density was registered for Gel-SH coated niches in contrast with what shown in literature where it is deeply studied that gelatin and other collagen substrates influence the growth characteristics of cells enhancing cell-adhesion and proliferation<sup>3,47</sup>. Probably, the poor cell adhesion observed is due to the slight hydrophobicity of the Gel-SH cross-linked coating (6.3.2.1), which can limit adhesion, proliferation and subsequent function of various cells like osteoblasts, chondrocytes as well as MSCs<sup>48,49</sup>. Moreover, the poor mechanical properties of Gel-SH coating ( $E \sim 0.2 \text{ kPa}$ ) play a main role. Firstly, it could lead to its easy detachment from the substrate due to both swelling and traction forces exerted by cells while adhering thus causing the detachment of the cells. Secondly, it is possible that while sensing such softer

substrates, cells tend not to proliferate and migrate towards the coated niches. This is in agreement with results obtained with our stiffer coatings and with studies from literature dealing with cell migration, where it is said that cells locomotion occurs faster as the stiffness of the substrate increases<sup>50</sup>.

Concerning differentiation behavior, cells were positive for collagen type I an early marker of chondrogenesis and negative for collagen-type II and for the other osteogenic and adipogenic markers tested.

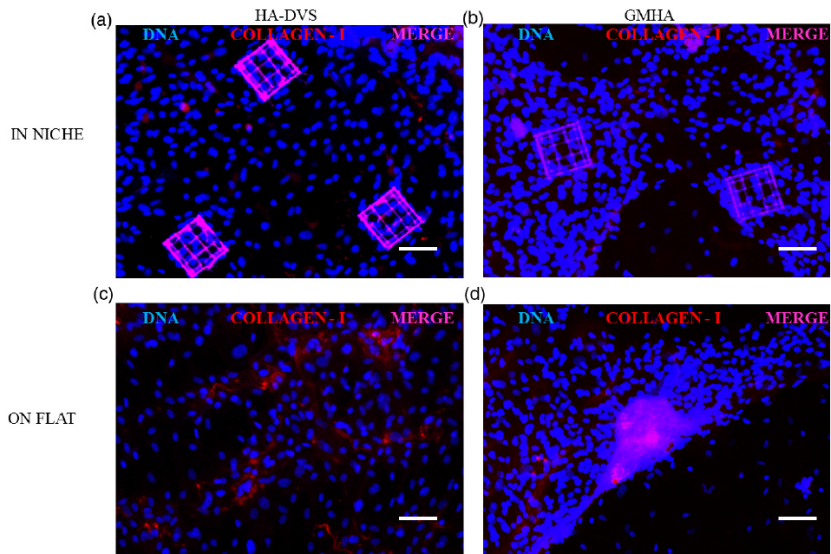


Figure 28. Fluorescence images acquired on HA:DVS (a and c) and GMHA (b and d) coated samples in two distinct areas: flat-coated areas and niches internal volume. Nuclei are stained with DAPI (blue) while collagen type-I is stained in red. In both samples, collagen type-I was expressed only by cells adhering on the flat-coated surfaces.

Positive staining cells were quantified both on coated and uncoated samples normalizing to the number of cells and different trends were observed depending on two parameters: the type of coating and the location of the cells on the samples (Table 9).

In the flat-coated area surrounding the niches, all the coated samples were positive to collagen I suggesting the main role of substrate stiffness in driving cell differentiation towards the osteo-chondral lineage even on 2D culture. The highest values was registered for HA:DVS coating, whose elastic modulus (20kPa) best mimic those of physiological osteo-chondral values (10 ÷ 100 kPa).

Table 9. Collagen I positive cells normalized with respect to the cell number counted on the coated and uncoated samples and grouped according to cell locations on the sample.

Sample	% on flat	Niche internal volume n°cells/(100 x 100 $\mu\text{m}^2$ )
HA:DVS	56.10 $\pm$ 12.5	Not significant
GMHA	38.08 $\pm$ 12.86	Not significant
Gel-SH:PEGDA	16.62 $\pm$ 10.3	37.24 $\pm$ 6.54
HA-DA	16.6 $\pm$ 1.04	Not significant
Uncoated niche	30.1 $\pm$ 4.8	Not significant

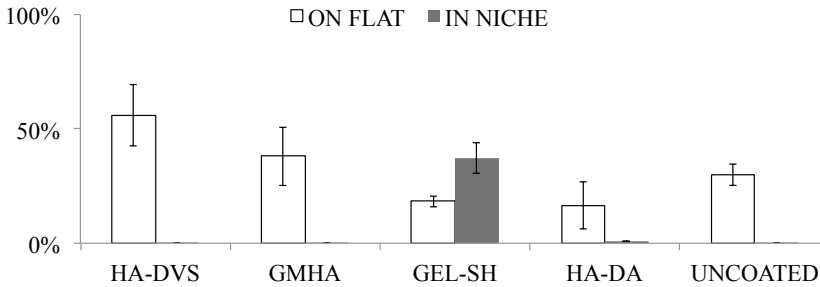


Figure 29. Diagrams for collagen I positive cells normalized with respect to the cell number counted on the coated and uncoated samples. The higher expression on flat surfaces was obtained for HA:DVS samples. Conversely, cells in the Gel-SH coated niches showed the higher positivity values.

The opposite trend was observed for the coated niches where the predominant role of the microarchitecture respect to substrate stiffness was attested by the increasing proliferation rate of cells, which resulted negative to markers of differentiation, while in presence of the HA-coating. The multipotency of these spherical cells aggregates is a consequence of the 3D adhesive configuration that cells assume in the internal niche volume. This suggest one potential application for the HA:DVS engineered niches for the production of therapeutic MSCs in large, pharmaceutically scale. Particularly, MSCs from patients could be expanded and cultured in vitro till the formations of aggregates. These, representing an unlimited autologous source, could be harvested and delivered for cell therapy while maintaining in culture the cells with higher stemness enabling the process

of aggregate fabrication to spontaneously restart thus producing further therapeutic cell doses.

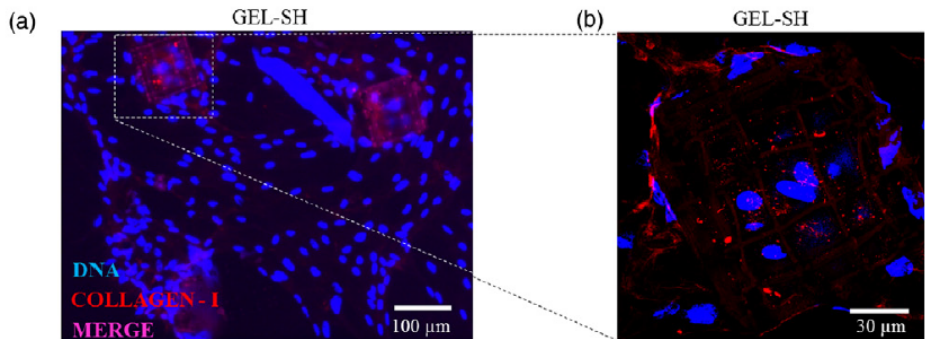


Figure 30. Fluorescence merged picture (a) and Z-stack merged projections of confocal images (b) acquired for Gel-SH coated niches. Cells within the niche and cells adhering on the external niche walls stained positive for collagen type-I (red), an early marker for osteo-chondral differentiation.

Surprisingly, cells on Gel-SH samples showed a significantly strong collagen I expression. As a matter of fact, gelatin and other collagen substrates are known to affect aspects of cell differentiation including mesenchymal stem cells commitment towards the osteo-chondral lineage. It is worthwhile to notice even the highly stretched morphology (Fig.25e and 25f) of MSCs adhering on Gel-SH sample. Thus, it is reasonable to suppose that there it might be a correlation between the morphology a cell assumes while adhering on a substrate and its differentiation behavior.

This result enhances what seen with previous study performed culturing MSCs for 21 days onto 2PP uncoated scaffolds where it was seen that 2PP uncoated niches had an important impact on cell adhesion and proliferation but were not capable to direct MSCs fate/to commit MSCs to osteo-chondral lineage<sup>15</sup>. The fact that MSCs started to differentiate in the functionalized niche presenting the lower stiffness values could indicate the main role that the chemistry of the surface coating combined with the geometry of the 3D architectures, have respect to a pure mechanical stimulus in addressing stem cells differentiation.

Finally, the MTT absorbance and DNA content ( $\mu\text{g}/\mu\text{l}$ ) ratio was measured in order to evaluate the specific metabolic activity of the cells cultured on the

engineered niches. Coherently with the result from immunofluorescence, the MTT/DNA ratio for Gel-SH-coated substrates was 30% greater than those for the other methods, thus attesting that collagen I production in those samples was supported by a high metabolic activity.

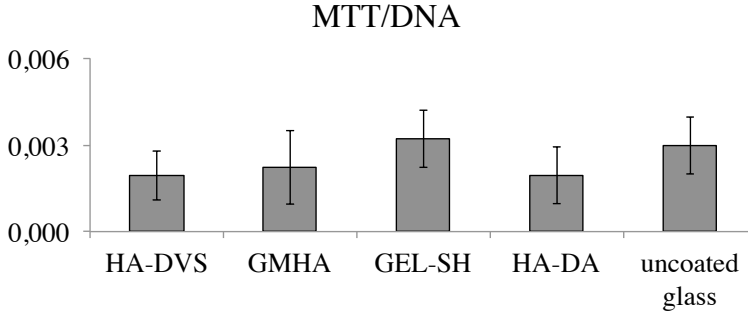


Figure 31. Cells specific metabolic activity measured for the various hydrogel-coated niches substrates. The MTT/DNA ratio measured for the Gel-SH samples resulted higher than the ones measured for the other substrates. Not significance differences resulting comparing to the uncoated control (N = 4 measurements, \* $p < 0,05$ ).

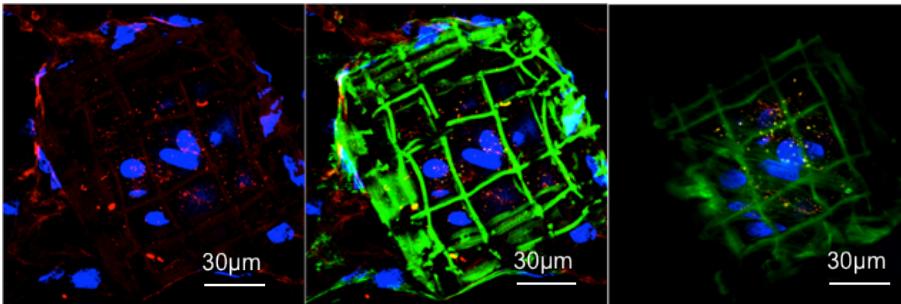


Figure 32. Z-stack projections of confocal images acquired on GEL-SH-coated niche substrates seeded with MSCs and cultured for 14 days. Nuclei stained blue, collagen type-I stained red and actin stained green.

To give more conclusive evidences and disentangle the effects of the different cues some improvements are needed. First, increasing the surface covered by the coated synthetic niches would allow obtaining a critical number of cells to perform quantitative analysis on cell functions (e.g. clonogenic assays, multilineage differentiation assays, PCR analysis for specific gene involved in SCs fate determination). Secondly, seeding fresh bone marrow cells directly on the coated synthetic niches would prevent cells from being influenced by their culture history. Actually, it has been demonstrated that recovering bone-marrow

MSCs from their tendency to adhere tightly to plastic culture affect cell function. Cells are influenced by their culture history, thus by the sum of all physical cues they have interacted with<sup>51</sup>.

## 5.4 Conclusions and future perspectives

Physiological stem cells niches were engineered *in vitro* by functionalizing 3D polymer scaffolds with different hydrogels matrix derived from hyaluronic acid and collagen. By mimicking such 3D microenvironment, we attempted to study the role that mechanical cues (i.e. 3D micro-geometry, topography and surface stiffness), have on driving mesenchymal stem cells functions *in vitro*.

2PP technique allowed fabricating 3D niches with suitable architecture, tailored to interact at the cell scale. The graded-pore geometry adopted was chosen to enhance spontaneous MSCs homing and differentiation. In order to ensure a high-level of control of the micro-geometry and to obtain free-standing structures, the SZ2080 photoresist was employed in 2PP with an elastic modulus of about 4 GPa. Therefore, to modulate the material stiffness sensed by cells adhering to the structures, different hydrogels with controlled mechanical and physico-chemical properties were developed and implemented to functionalize niches surfaces aiming to study the synergistic effect of the micro-geometry and the substrate stiffness on stem cell function.

Hyaluronic acid- and gelatin-based hydrogels were modified via crosslinking and conjugation reactions to widen their chemical and mechanical properties. Thus, different chemical and photochemical cross-linking processes allowed fine tuning the coating stiffness from 0.2 kPa for the thiolated-gelatin coating to 20 kPa for the DVS cross-linked HA coating, encompassing the range of physiological niches values. A simple and versatile PDMS-glass microfluidic system was fabricated to implement the different coating strategies explored to successfully functionalize SZ2080 structures. The hydrogels were efficiently grafted without significantly affecting the 3D micro-porosity, thus demonstrating from the technological side, the feasibility of coating such high-resolution small-sized niches.

Finally, biological tests were performed on hydrogel-coated structures to study aspects of biocompatibility and differentiation. All the hydrogel coatings resulted high biocompatible with enhanced proliferation and higher metabolic activity compared to uncoated scaffolds. Preliminary results confirmed the main role of

the micro-architecture in inducing cell homing behavior and enhancing cell proliferation even in the presence of a coating material. Particularly for HA-coating, cells were observed while migrating from the coated-flat towards the niches highlighting their preference to proliferate in a 3D-like environment while maintaining their pluripotency. The formation of this pluripotent cells agglomerated, localized where the niches were fabricated on the glass slide and characterized by high proliferation rate, suggests synthetic HA-functionalized niches potential application to produce therapeutic MSCs in large, pharmaceutically relevant scales. Conversely, cells anchored to softer Gel-SH coated niches showed type I-collagen expression indicating first commitment to osteo-chondral lineages, which was not observed on uncoated structures. The fact that MSCs started to differentiate in the functionalized niche presenting the lower stiffness values could indicate the main role that the chemistry of the surface coating, combined with the geometry of the micro architectures, has respect to the mechanical properties of the coating in addressing stem cells differentiation while cultured in a 3D niche.

The opposite trend was observed for flat-coated surfaces where the effect of the mechanical properties was predominant with cells highly expressing collagen type-I when cultured on stiffer HA-derived flat-coated surfaces whose stiffness best mimic those from physiological osteo-chondral niches.

Further investigations would deal with the development of hydrogel matrix containing both hyaluronic acid and gelatin to be implemented as coating materials for fine-graded 2PP structures. Combining the HA mechanical properties and gelatin capability to promote cell adhesion and differentiation of coatings containing both hyaluronic acid and gelatin, in order to exploit the mechanical properties of HA and the ability of gelatin to promote cell adhesion and differentiation, in a culture environment provided by three-dimensional scaffolds fabricated with 2PP references.

## 5.5 References

1. Joddar, B. & Ito, Y. Artificial niche substrates for embryonic and induced pluripotent stem cell cultures. *J. Biotechnol.* **168**, 218–28 (2013).
2. Bian, L., Guvendiren, M., Mauck, R. L. & Burdick, J. A. Hydrogels that mimic developmentally relevant matrix and N-cadherin interactions enhance MSC chondrogenesis. *Proc. Natl. Acad. Sci. U. S. A.* **110**, 10117–22 (2013).
3. Angele, P. *et al.* Characterization of esterified hyaluronan-gelatin polymer composites suitable for chondrogenic differentiation of mesenchymal stem cells. *J. Biomed. Mater. Res. A* **91**, 416–27 (2009).
4. Pittenger, M. F. Multilineage Potential of Adult Human Mesenchymal Stem Cells. *Science (80- )*. **284**, 143–147 (1999).
5. Barry, F. P. & Murphy, J. M. Mesenchymal stem cells: clinical applications and biological characterization. *Int. J. Biochem. Cell Biol.* **36**, 568–84 (2004).
6. Nava, M. M., Raimondi, M. T. & Pietrabissa, R. Controlling self-renewal and differentiation of stem cells via mechanical cues. *J. Biomed. Biotechnol.* **2012**, 797410 (2012).
7. Iyer, K. V., Pulford, S., Mogilner, A. & Shivashankar, G. V. Mechanical activation of cells induces chromatin remodeling preceding MKL nuclear transport. *Biophys. J.* **103**, 1416–28 (2012).
8. Maruo, S. & Fourkas, J. T. Recent progress in multiphoton microfabrication. *Laser Photonics Rev.* **2**, 100–111 (2008).
9. Ovsiyanikov, A., Mironov, V., Stampf, J. & Liska, R. Engineering 3D cell-culture matrices: multiphoton processing technologies for biological and tissue engineering applications. *Expert Rev. Med. Devices* **9**, 613–33 (2012).
10. Raimondi, M. T. *et al.* Two-photon laser polymerization: from fundamentals to biomedical application in tissue engineering and regenerative medicine. *J. Appl. Biomater. Funct. Mater.* **10**, 55–65 (2012).
11. Danilevičius, P. *et al.* Laser 3D micro/nanofabrication of polymers for tissue engineering applications. *Opt. Laser Technol.* **45**, 518–524 (2013).
12. Evans, N. D. *et al.* Substrate stiffness affects early differentiation events in embryonic stem cells. *Eur. Cells Mater.* **18**, 1–13 (2009).
13. Ovsiyanikov, A. *et al.* Ultra-low shrinkage hybrid photosensitive material for two-photon polymerization microfabrication. *ACS Nano* **2**, 2257–62 (2008).

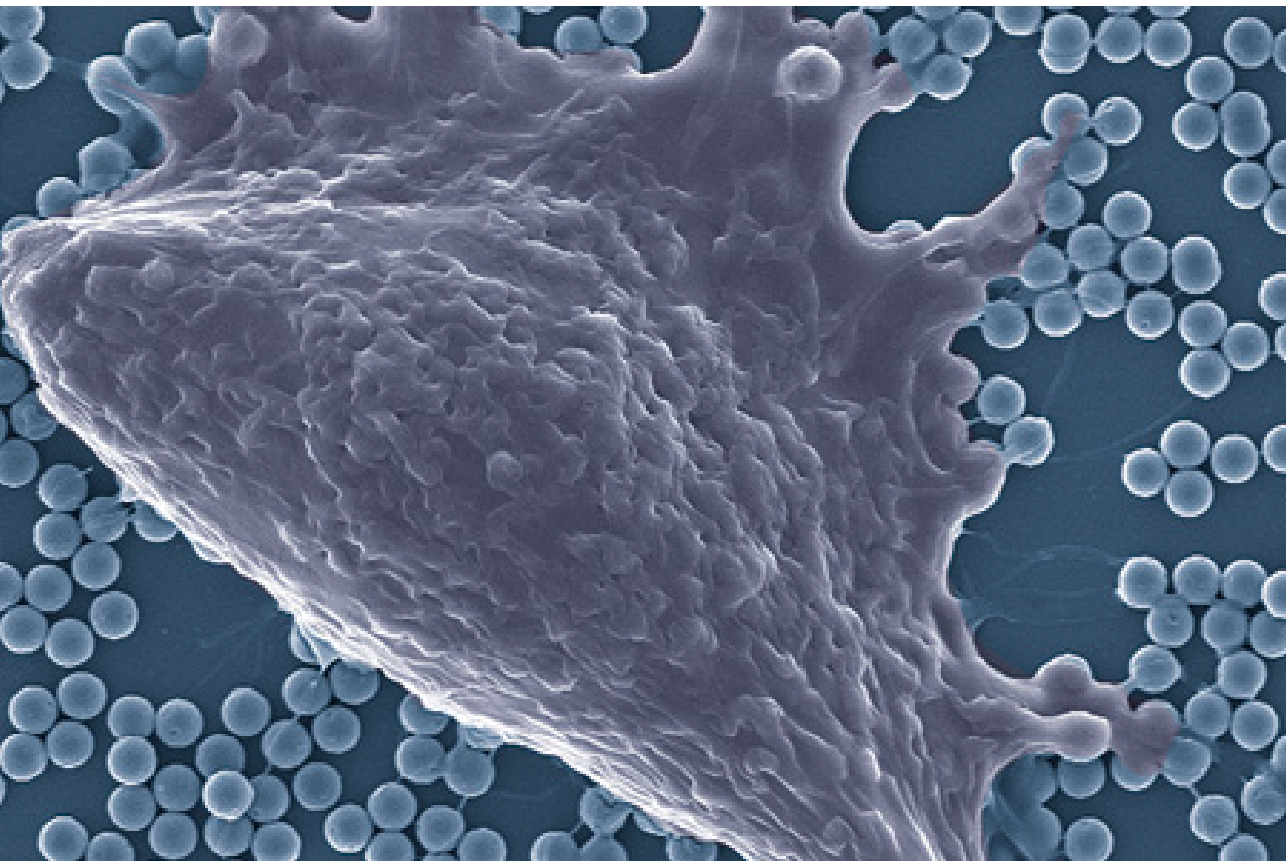
14. Raimondi, M. *et al.* Optimization of Femtosecond Laser Polymerized Structural Niches to Control Mesenchymal Stromal Cell Fate in Culture. *Micromachines* **5**, 341–358 (2014).
15. Raimondi, M. T. *et al.* Three-dimensional structural niches engineered via two-photon laser polymerization promote stem cell homing. *Acta Biomater.* **9**, 4579–84 (2013).
16. Collins, M. N. & Birkinshaw, C. Morphology of crosslinked hyaluronic acid porous hydrogels. *J. Appl. Polym. Sci.* **120**, 1040–1049 (2011).
17. Bencherif, S. A. *et al.* Influence of the degree of methacrylation on hyaluronic acid hydrogels properties. *Biomaterials* **29**, 1739–49 (2008).
18. Prata, J. E., Barth, T. A., Bencherif, S. A. & Washburn, N. R. Complex Fluids Based on Methacrylated Hyaluronic Acid. *Biomacromolecules* **11**, 769–775 (2010).
19. Baier Leach, J., Bivens, K. A., Patrick Jr., C. W. & Schmidt, C. E. Photocrosslinked hyaluronic acid hydrogels: Natural, biodegradable tissue engineering scaffolds. *Biotechnol. Bioeng.* **82**, 578–589 (2003).
20. Kim, T. G., Lee, Y. & Park, T. G. Controlled gene-eluting metal stent fabricated by bio-inspired surface modification with hyaluronic acid and deposition of DNA/PEI polyplexes. *Int. J. Pharm.* **384**, 181–8 (2010).
21. Shu, X. Z., Liu, Y., Palumbo, F. & Prestwich, G. D. Disulfide-crosslinked hyaluronan-gelatin hydrogel films: a covalent mimic of the extracellular matrix for in vitro cell growth. *Biomaterials* **24**, 3825–3834 (2003).
22. Shu, X. Z., Ahmad, S., Liu, Y. & Prestwich, G. D. Synthesis and evaluation of injectable, in situ crosslinkable synthetic extracellular matrices for tissue engineering. *J. Biomed. Mater. Res. Part A* **79A**, 902–912 (2006).
23. Vanderhooft, J. L., Alcoutlabi, M., Magda, J. J. & Prestwich, G. D. Rheological Properties of Cross-Linked Hyaluronan–Gelatin Hydrogels for Tissue Engineering. *Macromol. Biosci.* **9**, 20–28 (2009).
24. Xia, Y. & Whitesides, G. M. SOFT LITHOGRAPHY. *Annu. Rev. Mater. Sci.* **28**, 153–184 (1998).
25. Duffy, D. C., McDonald, J. C., Schueller, O. J. A. & Whitesides, G. M. Rapid Prototyping of Microfluidic Systems in Poly(dimethylsiloxane). *Anal. Chem.* **70**, 4974–4984 (1998).
26. Technical Datasheet. Dow Corning Sylgard.

27. Lee, H., Rho, J. & Messersmith, P. B. Facile Conjugation of Biomolecules onto Surfaces via Mussel Adhesive Protein Inspired Coatings. *Adv. Mater.* **21**, 431–434 (2009).
28. Waite, J. H. & Tanzer, M. L. Polyphenolic substance of *Mytilus edulis*: novel adhesive containing L-dopa and hydroxyproline. *Science* **212**, 1038–1040 (1981).
29. Herlinger, E., Jameson, R. F. & Linert, W. Spontaneous autoxidation of dopamine. *J. Chem. Soc. Perkin Trans. 2* 259–263 (1995). doi:10.1039/P29950000259
30. Faure, E. *et al.* Catechols as versatile platforms in polymer chemistry. *Prog. Polym. Sci.* **38**, 236–270 (2013).
31. Lee, H., Dellatore, S. M., Miller, W. M. & Messersmith, P. B. Mussel-Inspired Surface Chemistry for Multifunctional Coatings. *Sci.* **318**, 426–430 (2007).
32. Zangmeister, R. A., Morris, T. A. & Tarlov, M. J. Characterization of polydopamine thin films deposited at short times by autoxidation of dopamine. *Langmuir* **29**, 8619–28 (2013).
33. Flory, P. J. *Principles of Polymer Chemistry*. 672 (1953).
34. Anseth, K. S., Bowman, C. N. & Brannon-Peppas, L. Mechanical properties of hydrogels and their experimental determination. *Biomaterials* **17**, 1647–1657 (1996).
35. Credi, C. *et al.* Fine tuning and measurement of mechanical properties of crosslinked hyaluronic acid hydrogels as biomimetic scaffold coating in regenerative medicine. *J. Mech. Behav. Biomed. Mater.* **29**, 309–316 (2014).
36. Marsano, E., Gagliardi, S., Ghioni, F. & Bianchi, E. Behaviour of gels based on (hydroxypropyl) cellulose methacrylate. *Polymer (Guildf)*. **41**, 7691–7698 (2000).
37. Treloar, L. R. G. *The Physics of Rubber Elasticity*. (OUP Oxford, 2005). at <<http://books.google.it/books?id=-iyDehYpoAQC>>
38. Hachet, E., Van Den Berghe, H., Bayma, E., Block, M. R. & Auzély-Velty, R. Design of biomimetic cell-interactive substrates using hyaluronic acid hydrogels with tunable mechanical properties. *Biomacromolecules* **13**, 1818–27 (2012).
39. Pautke, C. *et al.* Characterization of osteosarcoma cell lines MG-63, Saos-2 and U-2 OS in comparison to human osteoblasts. *Anticancer Res.* **24**, 3743–3748 (2004).
40. Danilevicius, P. *et al.* Micro-structured polymer scaffolds fabricated by direct laser writing for tissue engineering. *J. Biomed. Opt.* **17**, 081405–1 (2012).

41. Mathe, G., Albersdorfer, A., Neumaier, K. R. & Sackmann, E. Disjoining pressure and swelling dynamics of thin adsorbed polymer films under controlled hydration conditions. *Langmuir* **15**, 8726–8735 (1999).
42. Dreyer, D. R., Miller, D. J., Freeman, B. D., Paul, D. R. & Bielawski, C. W. Perspectives on poly(dopamine). *Chem. Sci.* **4**, 3796–3802 (2013).
43. Yang, K. *et al.* Polydopamine-mediated surface modification of scaffold materials for human neural stem cell engineering. *Biomaterials* **33**, 6952–64 (2012).
44. Schneider, A., Richert, L., Francius, G., Voegel, J.-C. & Picart, C. Elasticity, biodegradability and cell adhesive properties of chitosan/hyaluronan multilayer films. *Biomed. Mater.* **2**, S45–51 (2007).
45. Suh, K. Y. *et al.* Characterization of chemisorbed hyaluronic acid directly immobilized on solid substrates. *J. Biomed. Mater. Res. Part B Appl. Biomater.* **72B**, 292–298 (2005).
46. Engler, A. J., Sen, S., Sweeney, H. L. & Discher, D. E. Matrix elasticity directs stem cell lineage specification. *Cell* **126**, 677–89 (2006).
47. Angele, P. *et al.* Influence of different collagen species on physico-chemical properties of crosslinked collagen matrices. *Biomaterials* **25**, 2831–41 (2004).
48. Fan, H. *et al.* Cartilage regeneration using mesenchymal stem cells and a PLGA-gelatin/chondroitin/hyaluronate hybrid scaffold. *Biomaterials* **27**, 4573–80 (2006).
49. Kay, S., Thapa, A., Haberstroh, K. M. & Webster, T. J. Nanostructured polymer/nanophase ceramic composites enhance osteoblast and chondrocyte adhesion. *Tissue Eng.* **8**, 753–61 (2002).
50. Trichet, L. *et al.* Evidence of a large-scale mechanosensing mechanism for cellular adaptation to substrate stiffness. *Proc. Natl. Acad. Sci. U. S. A.* **109**, 6933–8 (2012).
51. Yang, C., Tibbitt, M. W., Basta, L. & Anseth, K. S. Mechanical memory and dosing influence stem cell fate. *Nat. Mater.* **13**, 645–52 (2014).



**6.**  
**Protein anti-fouling and fouling-release  
in perfluoropolyether surfaces**



## 6.1 Introduction

Anti-fouling materials have attracted a significant interest, especially as marine coatings and in biotechnology. In the former case they are used to prevent biofouling adhesion on ship hulls<sup>1</sup>, thus reducing hydrodynamic drag and fuel consumption, while in bio-chemistry and biotechnology anti-fouling surfaces allow for the design and realization of protein resistant devices and components<sup>2</sup>. In this scenario, Perfluoropolyethers (PFPEs) materials have gained lots of attention as high performance protective coatings materials in marine field<sup>3-5</sup> and for water/oil repellent surface treatments<sup>6,7</sup>.

In contrast to the available information concerning biofouling release properties of PFPEs coatings, very little is known about the mechanism of molecular interaction of these surfaces and proteins. Actually, UV curable perfluoropolyether-dimethacrylates (PFPE-DMAs) have been used for biomedical devices microfabrication<sup>8</sup> and more recently amphiphilic structures containing both hydrophilic and hydrophobic moieties have been proposed as potential fouling-release coatings. Blends of photocurable perfluoropolyether-dimethacrylate/polyethyleneglycol-methacrylate polymeric (PFPE/PEG blend) were developed to study the effect of the PEG chain molecular weight on fouling-release properties against spores<sup>9</sup>. Other works in the literature have tested the effectiveness of other perfluoropolyether polymers as protein-adhesion resistant substrate<sup>10</sup>. First studies revealed the main role that surface properties have on protein adhesion resistance behavior. Particularly, the relationship between surface free energy and bioadhesion of blood proteins<sup>11</sup> and platelets was investigated and 20 and 30 mJ/m<sup>2</sup> was identified as the critical surface tension range ideal in preventing bioadhesion<sup>12</sup>. However, more recent studies suggested that surface tension must be considered keeping in mind also the elastic modulus of the material. A more comprehensive approach is to study fouling adhesion against  $(E\gamma)^{1/2}$  to study the combined effect of both elastic modulus and surface tension<sup>13,14</sup>. A low surface tension is crucial for the initial attachment of proteins, while the elastic modulus of the substrate mainly affects the fouling release

properties, since it induces the joint formed between the substrate and the protein to fail by peel rather than by shear. Finally, also the coating thickness could play a role, since less force is needed to remove a fouling layer from a thicker coating<sup>15,16</sup>. Thus, the joint between proteins and the coating can be studied in terms of fracture mechanics highlighting the dependence of fouling release performance on  $(E\gamma)^{1/2}$ . Following this relation, the main topic of this work was to study the behavior of perfluoropolyether polymers as protein adhesion-resistant substrates. Poly(ethylene glycol) (PEG) was used as positive benchmark due to its well-known protein anti-fouling properties<sup>2,17</sup>. Different UV curable perfluoropolyether polymers, copolymers and blends were described, fully characterized, and their protein antifouling and fouling-release behavior was investigated as a function of both their surface energy and mechanical properties. The main structural parameters<sup>15,18</sup> affecting their functional behavior are highlighted, giving useful information for the design and selection of high performance, protein resistant PFPE surfaces.

## 6.2 Experimental section

### 6.2.1 Perfluoropolyether materials

Two photocurable dimethacryloxy-functionalized perfluoropolyethers (PFPE-DMA) differing for molecular weight were used in the present work. PFPE urethane dimethacrylate oligomer with molecular weight  $M_n = 1980$  g/mol, indicated as PFPE-DMA 2000 in the following, was kindly provided by Solvay Specialty Polymers (Bollate, Italy; commercial name Fluorolink™ MD700). A higher molecular weight PFPE urethane dimethacrylate, indicated as PFPE-DMA 4000 here on, was obtained according to previous work<sup>8,16</sup> starting from the hydroxyl terminated PFPE bifunctional oligomers and end-capping through urethane chemistry with isocyanatoethyl methacrylate (IEM, Alfa Aesar). Briefly, a perfluoropolyether macrodiol (Fluorolink™ D4000, Solvay Specialty Polymers) with  $M_n = 3885$  g/mol and 94.8% of effective OH groups was reacted with IEM at 45°C for 24h in the presence of 1,4-Diazabicyclo[2.2.2]octane (DABCO, Sigma Aldrich) as catalyst and trichlorotrifluoroethane (Freon 113, Sigma-Aldrich), as solvent. The molar ratio between the two components PFPE macrodiol:IEM was 1:2 since every PFPE macrodiol molecule brings two -OH groups. However a little excess of macrodiol was preferred to avoid any non-reacted NCO group at the end of the reaction. DABCO was 0.5% v/v with respect to IEM volume, while the percentage of IEM was 21% v/v with respect to the solvent.

Table 1. PFPE-DMA properties.

PFPE-material	$M_n$ [g/mol]	$\rho$ [g/ml]	$CF_2CF_2O/(CF_2O)$
PFPE-DMA 2000	1980	1.66	1
PFPE-DMA 4000	4127	1.66	1

Two Perfluoropolyether poly(ethylene glycol) diacrylates (PFPE-PEG-DAs) differing for the number of repeating PEG units were kindly provided by Solvay. These experimental materials are obtained from a PFPE diol by the sequential addition of a PEG chain and end-capped by acrylic groups through ester bond, which enable UV cross-linking. One PFPE-PEG-DA sample has a molecular weight  $M_n = 2030$  g/mol and is characterized by 4.6 ethylene glycol (EG) repeating units

in the backbone ( $p$  is 4.6 with reference to fig della sezione); the second one, with molecular weight  $M_n = 2206$  g/mol is constituted by 8 EG repeating units.

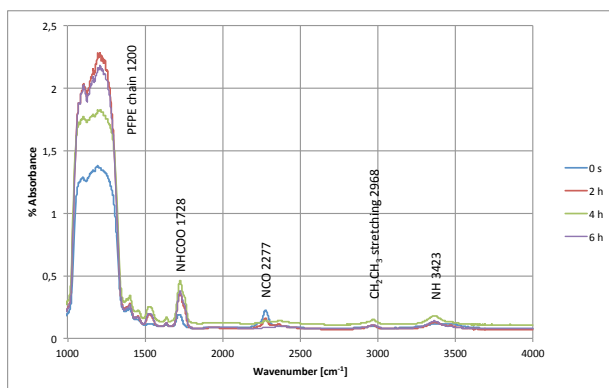
Table 2. PFPE-PEG-DAs properties.

	$M_n$ [g/mol]	EG repeating units
PFPE-PEG4.6-DA	2030	4.6
PFPE-PEG8-DA	2206	8

Subsequent photo curing of the PFPEs is accomplished through blending with 4% of 2-hydroxy-2-methyl-1-phenyl-propan-1-one (Darocur®1173, Ciba) as photoinitiator with the exception of PFPE-DMA 4000 that was prepared by adding 1% wt of the same photoinitiator. Cross-linking was performed in nitrogen atmosphere exposing to UV-light with a bromograph (MF 1030, Nuova Delta Elettronica, Italy) equipped with 4 lamps of 15 W each, with an emitted power density in the UV-A range of 4 mW/cm<sup>2</sup>.

### 6.2.2 Fourier Transform Infrared spectroscopy (FTIR) analysis

The reaction conversion during PFPE-DMA 4000 functionalization was evaluated through FTIR analysis by following simultaneously the progressive disappearance of the NCO stretching located at 2275 cm<sup>-1</sup> and the appearance of the peak located at 1740 cm<sup>-1</sup>, which corresponds to the urethane group (NHCOO).



Graph 1. IR spectra acquired at different times during reaction. The -NCO peak (2277 cm<sup>-1</sup>) progressively disappears with the simultaneous increase of the urethane one (1728 cm<sup>-1</sup>). After 4 hours the reaction ended.

Spectra were acquired using a Thermo Nicolet Nexus 670 FTIR spectrometer that uses Global as IR source and DTGS or MCT as detectors. Its frequency range goes from 400 to 12,000  $\text{cm}^{-1}$  while the spectra resolution is 0.125  $\text{cm}^{-1}$ . The comparison of spectra acquired at different times allows for the estimation of extent of reaction. After 4 h the NCO peak completely disappeared indicating that the reaction ended.

### 6.2.3 Surface characterization

PFPEs substrates for contact angle measurements were prepared by spincoating (900 rpm for 30s; ws400 6npp lite, Laurell Technologies Corp.) on a glass substrate and subsequently UV-irradiating for curing. The contact angle (CA) measurements were performed with an optical video contact angle system (OCA-15-plus, Dataphysics, Germany) equipped with a CCD camera. The static contact angle was measured by means of the sessile drop technique with dedicated software (SCA 2.0) determining the contact angle based on the Young-Laplace fitting. A 1  $\mu\text{l}$  droplet of water (Chromasolv water for HPLC, Sigma Aldrich) was dispensed on the sample using the electronic syringe unit of the instrument equipped with a 500  $\mu\text{l}$ -Hamilton syringe. At least six measurements were performed at different areas on each sample and results were averaged. The same procedure was followed using diiodomethane (Sigma-Aldrich) because at least two liquids are necessary to compute surface tension. Solid surface tension  $\gamma_s$  and their components, dispersive  $\gamma_s^d$  and polar  $\gamma_s^p$ , were calculated by means of Wu method<sup>19</sup> and by using a value of surface tension for water  $\gamma_l = 72.8 \text{ mN/m} = \gamma_l^d + \gamma_l^p = (22.6 + 50.2) \text{ mN/m}$  and for diiodomethane  $\gamma_l = 50.8 \text{ mN/m} = \gamma_l^d + \gamma_l^p = (49.0 + 1.8) \text{ mN/m}$ . Dynamic measurements were done by increasing the drop volume in the wetting process (advancing contact angle) and then decreasing it in the de-wetting phase (receding contact angle). The syringe needle remains in the drop during the whole process. In the first wetting phase a 3- $\mu\text{l}$  drop was created on the solid surface and then slowly increased in volume. In the second phase the surface was de-wetted and the drop size reduced. The whole cycle was

repeated 5 times at 1  $\mu\text{l/s}$ , with a delay time of 1s between each cycle. The method for the calculation of the advanced and receding angles was the elliptic fitting one.

## 6.2.4 Dynamic mechanical analysis

Dynamic mechanical analyses (DMA) of cross-linked polymer films were performed with a Mettler Toledo DMA7SDTA 861 dynamic mechanical analyzer in shear sandwich mode. All samples were tested at 0.1 Hz with  $T = 23^\circ\text{C}$  and  $70^\circ\text{C}$ , and  $G'$  values were obtained as a function of oscillation amplitude.  $G'$  values in the linear viscoelastic range (deformation  $<0.5\%$ ) were extrapolated to obtain Young modulus values. Round-shaped PFPE samples with 15 mm diameter and thickness of  $600 \div 700 \mu\text{m}$  were prepared by casting 0.5 – 1.0 g of oligomer in a rounded cap having diameter of 24 mm and UV-exposing for 10 min. Then, PFPE films were punched to obtain disk with the desired diameter.

## 6.2.5 Anti-fouling and fouling release properties evaluation

### 6.2.5.1 Protein adhesion resistance

Anti-fouling and fouling-release properties against proteins of polymer surfaces were evaluated using a 0.01% (w/v) solution of fluorescein isothiocyanate bovine serum albumin (BSA-FITC) (Sigma-Aldrich) in distilled water. Different materials were tested to benchmark the performances of PFPE photopolymers. Polymethylmethacrylate (PMMA, Perspex<sup>TM</sup> by Lucite) and Polydimethylsiloxane<sup>20</sup> (PDMS, Sylgard<sup>TM</sup> 184 by Dow Corning) are known to absorb proteins while polyethylene glycol<sup>21</sup> (PEG) is a typical anti-fouling material. In particular, a PEG based photopolymer<sup>22</sup>, named as PEG-MA in the following, was tested in the experiments together with a PFPE/PEG blend taken from the literature<sup>9</sup> to compare its non-fouling properties. The latter is a mixture of polyethylene glycol monomethacrylate with molecular weight  $M_n = 450 \text{ g/mol}$  and PFPE-DMA 2000 in weight ratio 10:90 doped with 4% of Darocur 1173 to

allow photocuring. In conclusion, the complete set of test materials was PMMA, PDMS, PEG-MA, PFPE/PEG blend, PFPE-DMA 2000, PFPE-DMA 4000, PFPE-PEG 4.6-DA and PFPE-PEG 8-DA. Anti-fouling static tests were performed by incubating the substrates with BSA-FITC solution for 60 min at 37°C. Then, samples were rinsed with distilled water twice and dried for 25 min at 37°C. Fouling-release dynamic tests were performed pumping BSA-FITC solution at 7.2  $\mu\text{l}/\text{min}$  for 1h, using a microfluidic pump (Syringe Pump 11 Plus, Harvard Apparatus), through a microfluidic system. This was assembled by reversibly sealing a flat surface of the substrate material to be tested (PFPEs, PDMS, PMMA or PEG) with a PDMS channel obtained by replica of a SU-8 (SU-8 2050, MicroChem, USA) mold. Channel dimensions were 500  $\mu\text{m}$  x 200  $\mu\text{m}$ . For sample rinsing, distilled water was fluxed at 100  $\mu\text{l}/\text{min}$  through the same channel. Images of adsorbed proteins were acquired analyzing a samples area of 650 x 500  $\mu\text{m}^2$  by a fluorescence microscope (Olympus IX70 inverted microscope) and their fluorescence intensities were evaluated by ImageJ<sup>TM</sup> software. Quantitative analyses were performed through the tonal distribution (image histogram) of digital fluorescent images. They represent the number of pixels for each tonal value on a scale having 255 green tonalities. The mean tonal value was taken as the reference parameter to evaluate BSA adhesion on tested materials. The standard deviation was calculated averaging the mean tonal values of three different images for each sample material.

#### 6.2.5.2 Protein adhesion test automatization

A microarrayer (SpotBot® 2 Protein Edition - SPA2PRO, ArrayIt®) was exploited to perform static protein adhesion resistance tests of PFPEs substrates in controlled standard conditions. Tests were performed at the Institute for Bioengineering of Catalonia (IBEC). SPA2PRO utilizes advanced micro-robotics that enable to easily and affordably print different types of protein solutions in close contact on the same substrates. For these experiments, proteins solutions at different concentrations (0.002, 0.02, 0.2, and 2 mg/ml) were prepared diluting Bovine Serum Albumin (BSA), Streptavidin (StAv), and ImmunoglobulinG Donkey

Anti-Goat (H+L) (IgG), all Alexa Fluor® 555 conjugated (Thermo Fischer Scientific), in PBS. For protein printing, 25  $\mu\text{l}$  of each protein solutions were loaded in the dedicated reservoirs constituted of a 384-well microplate (Fig.1a) and the substrates to be patterned were located in a homemade PMMA sample holder positioned in the printing desk (Fig.1b). The holder is equipped with pins and holes connected with pumps and compressors used to both flowing washing buffers and fluxing air over the printed samples thus allowing the automatization of the washing and air-drying steps requested after each printing process to remove aspecifically-adsorbed biomolecules.

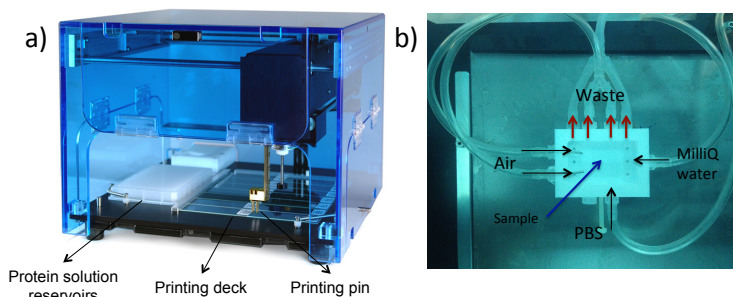


Figure 1. Pictures illustrating (a) the SPA2PRO® arrayer exploited for automatized protein printing and (b) the PMMA homemade sample holder located in the printing desk.

A pattern consisting in 12 blokes of 18 dots of 100  $\mu\text{m}$  nominal diameter and 200- $\mu\text{m}$  spaced (Fig.2) was designed and implemented through dedicated software (Multiple Microarray Format SpotSupport) to program the arrayer. To deliver the protein on the substrates, the printing pin was moved to the first loading position in the 384-well microplate, lowered to the bottom of the plate, and paused for 3 seconds allowing the protein samples to load into the pin tip by capillary action (Fig.3a and 3b). The flat tip allows a thin layer of sample to form at the end of the tip which directly contacts the underlying surface leaving a printed microarray spot (Fig.3c). After each spot printing, the pin was washed and dried before loading a new sample volume and repeating the printing. Thanks to the humidification apparatus and the built-in temperature controlling system, during the printing process the whole chamber was kept constant at 37°C and 80% of humidity thus better mimicking physiological conditions and

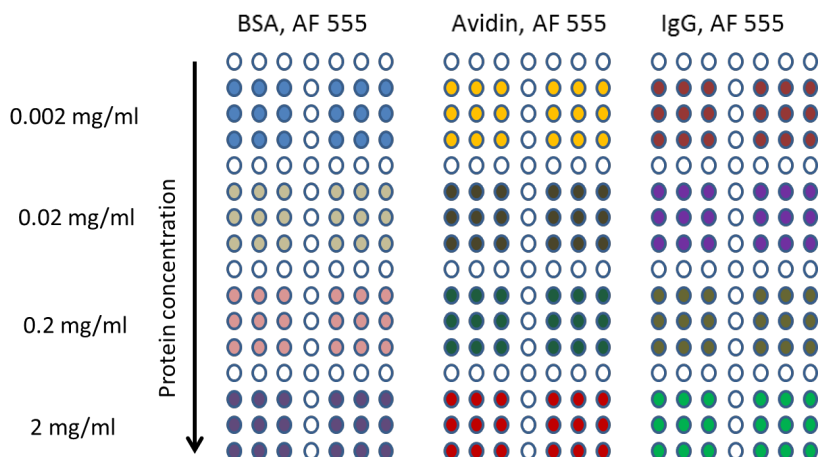


Figure 2. Scheme illustrating the printed protein pattern constituted of 12 blokes of 18 dots each.

avoiding early protein solution evaporation. At the end of the printing process, after 1h of incubation in the chamber, the substrates were washed and dried. For this step, PBS and water were pumped through dedicated pins onto the patterned substrates until the volume of the holder was filled.

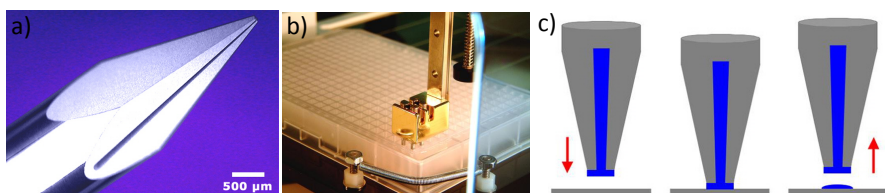


Figure 3. (a) Image of a printing pin showing the uptake channel. (b) The protein solution is loaded into the pin channel by capillary action. (c) The pin is horizontally leveled to allow the formation of a thin protein sample layer, which is printed on the substrate by direct contact.

Then, the washing solution was removed and the sample was dried by fluxing air. Prior and after the washing and drying steps, images of the patterned proteins arrays were acquired by a fluorescence microscope (Nikon E1000) and their fluorescence intensities were then evaluated by ImajeJ™ software. Particularly, for each arrays was calculated the integrated density which estimates a value of fluorescence taking into account the mean gray value of a selected area and the size of this area (in our case the area of the spots) or could be the sum of all the pixel intensities in the reference area.

### 6.2.5.3 Cell adhesion resistance

Cell adhesion resistance of PFPE-DMA 4000 substrates was evaluated in static conditions seeding cells on the surfaces and incubating for two days. Tests were performed at the Laboratory of Biological Structures Mechanics (LaBS). Unless otherwise specified, chemicals were purchased from Sigma-Aldrich, cell culture media and supplements from Euroclone and cell culture plastics from Corning. MG63 human osteosarcoma cells line (86051601-1VL, Sigma-Aldrich) were resuscitated and expanded in minimum essential medium (MEM) supplemented with 10% v/v Fetal Bovine Serum (FBS), 1% v/v Non Essential Amino Acids 100X solution (NEAAs), 1% v/v Penicillin/Streptomycin 100 X solution, and 1% v/v LGlutamine 2mM solution. Cells were grown for two days in an incubator (NAPCO) under 5% CO<sub>2</sub> atmosphere at 37°C. After removal of the growth medium and after rinsing with a PBS solution to remove suspended cells, cells were detached from the culture plate incubating with a trypsin solution containing 0.05% trypsin 10X and 0.02% EDTA and incubating for 15 minutes.

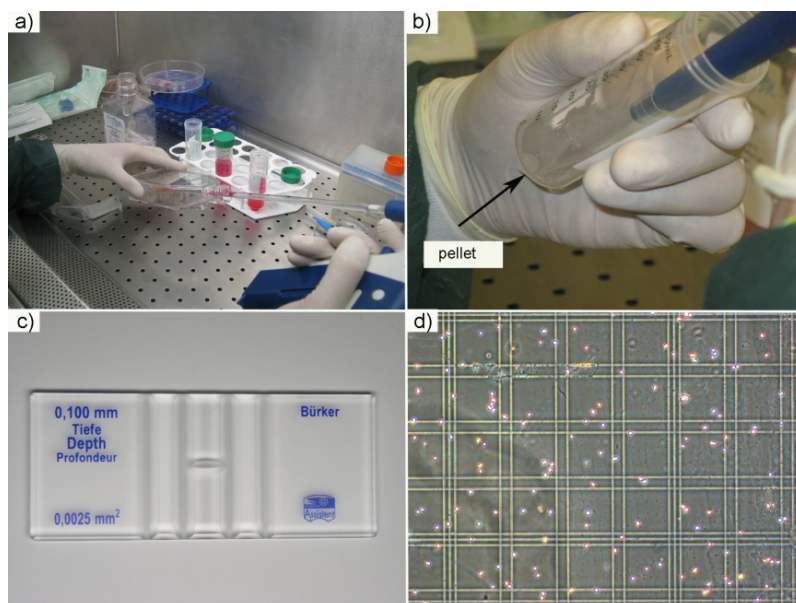


Figure 4. Cells are trypsinized and detached from the culture plate (a); after centrifugation, the cell pellet is washed and resuspended (b); picture of the Bürker chamber (c) and the counting net engraved in its central platform, where dead cells stain blue due to trypan solution which permeates dead cell membranes.

Then trypsin was removed and cells were resuspended in 2.5 ml of growth medium, centrifuged for 5 minutes at 2000 rpm (Sigma 3-16 PK, Euro Clone) (Fig.4a and 4b). The liquid phase was removed and the pellet was diluted in 10 ml of cell growth medium. To discriminate between live and dead cells, 10  $\mu$ l of cell solution were mixed with 10  $\mu$ l of trypan blue which stains dead cells having permeable membranes (0.05% in PBS) and the mixture was poured in a Burker chamber (Fig.4c and 4d). Approximately 1,000,000 cells/ml were counted. For cells seeding, two disk-shaped fully cured PFPE-DMA 4000 samples were prepared, sterilized for 20 minutes under UV light and located in a multiwell. Phase contrast (Olympus IX70) and scanning electron microscope (EVO 50 extended Pressure system, Carl Zeiss) images were acquired to assess cell behavior onto PFPE surfaces.

## 6.3 Results and discussion

### 6.3.1 Photocurable PFPEs

To study the effect that chemical structure has on material performance against anti-fouling/fouling release properties, telechelic PFPE diols were modified to create PFPE urethane methacrylic and PFPE-PEG acrylic polymers. PFPE molecular structure is composed of three main parts: a central perfluoropolyether backbone, two more polar lateral segments and terminal photocurable moieties. It can be schematized as  $G-R_h$ -PFPE- $R_h-G^{23}$ , where  $G$  is the photo reactive group,  $R_h$  is the polar moiety and PFPE refers to the main perfluoropolyether chain. For PFPE-DMAs the photoreactive  $G$  unity is represented by a methacrylic group, while  $R_h$  refers to the lateral polar urethane group. PFPE-PEG-DAs instead have acrylic functionalities as for  $G$  and lateral polar poly(ethylene glycol) segments as  $R_h$  groups (Fig.5). PFPE-PEG-DAs instead are composed of acrylic photoreactive groups ( $G$ ) and lateral polar poly(ethylene glycol) segments ( $R_h$ ) (Fig.6).

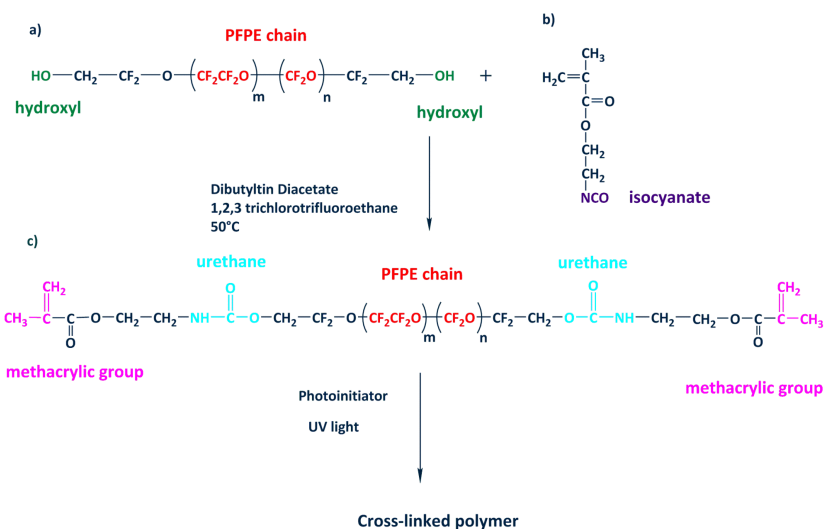


Figure 5. Perfluoropolyether dimethacrylates (c) obtained from the reaction of a perfluoropolyether macrodiol (a) with an isocyanate ethyl methacrylate (b).

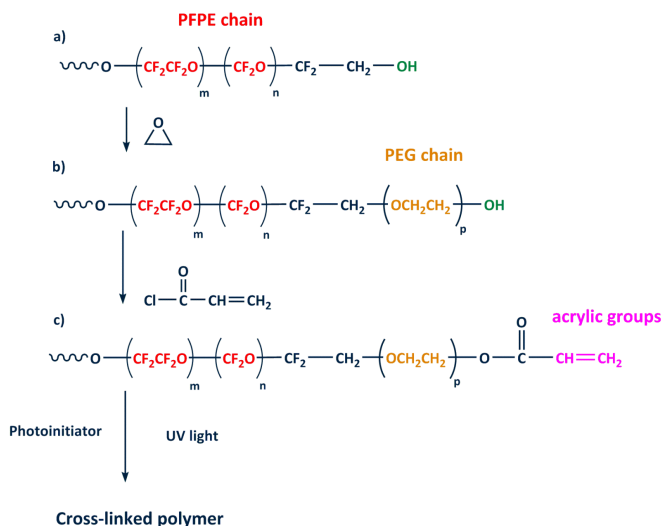


Figure 6. Perfluoropolyether poly(ethylene glycol) dyacrylates obtained from a perfluoropolyether diol (a) by the sequential addition of a polyethylene glycol chain (b) and finally of acrylic end chain groups (c)

### 6.3.2 Surface characterization: contact angle

The water and diiodomethane static contact angles were measured to calculate the surface tension of the substrates. The results shown in Table 3 show that all PFPE-based surfaces are hydrophobic with water contact angle above 90°. Lower values were measured for PFPE-PEG-DA polymers due to the presence of a polar ethylene-oxide chain.

Table 3. Contact angle measurements using water.

	Average values [°]
PFPE-DMA 2000	110 ± 0.7
PFPE-DMA 4000	113 ± 0.7
PFPE-PEG4.6-DA	103 ± 1.2
PFPE-PEG8-DA	107 ± 0.9

Surface energies and its polar and dispersive components are reported in Table 4. Values were estimated by Wu's harmonic-mean method, enabling to discriminate between its components, using the following Equation of the interfacial tension  $\gamma_{sl}$ :

$$\gamma_{sl} = \gamma_{sv} + \gamma_{lv} - \frac{4 \gamma_{sv}^d \gamma_{lv}^d}{\gamma_{sv}^d + \gamma_{lv}^d} - \frac{4 \gamma_{sv}^p \gamma_{lv}^p}{\gamma_{sv}^p + \gamma_{lv}^p}$$

where the subscript *sv* and *lv* refer respectively to the solid and to the testing liquid and the subscripts *d* and *p* indicate the dispersive and polar components of surface tension and so  $\gamma_{sv} = \gamma_{sv}^d + \gamma_{sv}^p$ . It is worthwhile to notice that for PFPE-DMAs the dispersive component, associated to the fluorocarbon moiety, is predominant with respect to the polar one, which is related to the urethane groups. This is due to the fact that the fraction of urethane groups is much smaller than to the fluorocarbon chain. Conversely, PFPE-PEG-DAs show a higher surface tension with the predominance of the polar component associated to the hydrophilic poly(ethyleneglycol) chain in the molecular backbone.

Table 4. Surface tension and its components determined using Wu method calculation.

Material	SFT polar [mN/m]	SFT dispersive [mN/m]	SFT total [mN/m]
PFPE-DMA 2000	2.7	13.4	16.1
[%]	20.0	80.0	
PFPE-DMA 4000	2.8	13.2	16.0
[%]	22.0	78.0	
PFPE-PEG4.6-DA	13.6	6.2	19.8
[%]	69.0	31.0	
PFPE-PEG8-DA	13.6	4.8	18.4
[%]	74.0	26.0	

The dynamic advancing ( $\theta_a$ ) and receding ( $\theta_r$ ) contact angle measurements were also carried out to verify the presence of thermodynamic contact angle hysteresis  $\Delta\theta$ , defined as the difference between  $\theta_a$  and  $\theta_r$ , which is due to the chemical heterogeneity of the surfaces<sup>24</sup>. Particularly,  $\theta_a$  is mainly affected by low energy or hydrophobic domains, whereas  $\theta_r$  by polar and hydrophilic zones<sup>25</sup>. The results of dynamic measurements are summarized in Table 5 and show a clear hysteresis of all PFPE-based materials.

Table 5. Dynamic contact angles and contact angle hysteresis for PFPEs surfaces.

	PFPE-DMA 2000	PFPE-DMA 4000	PFPE-PEG4.6- DA	PFPE-PEG8- DA
	Contact angle $\pm$ SD [°]			
$\theta_a$	96 $\pm$ 0.5	95.1 $\pm$ 0.5	94.73 $\pm$ 0.8	87.4 $\pm$ 3.3
$\theta_r$	74.45 $\pm$ 0.6	74.73 $\pm$ 0.2	71.7 $\pm$ 1.5	55.8 $\pm$ 4.7
$\Delta\theta$	21.55 $\pm$ 0.4	20.38 $\pm$ 0.6	23.03 $\pm$ 2.3	31.6 $\pm$ 1.5

Graphs reported in Figure 7 illustrates the change of hysteresis value in time, the kinetic contact angle hysteresis, which indicates molecular rearrangements of functional groups at the solid-liquid interface<sup>26</sup>.  $\theta_a$  and  $\theta_r$  are quite constant overtime for PFPE-DMAs, revealing a pure thermodynamic behavior, and surface reorganization may be associated in this case to the polar urethane moieties. The slight decrease in  $\Delta\theta$  for PFPE-DMA 4000 with respect to the lower molecular weight PFPE-DMA 2000 is attributed to the decreased density of urethane groups. On the contrary, the kinetic behavior of PFPE-PEG-DAs was associated to the surface rearrangement of the polar PEG chains stimulated by the contact with

water.

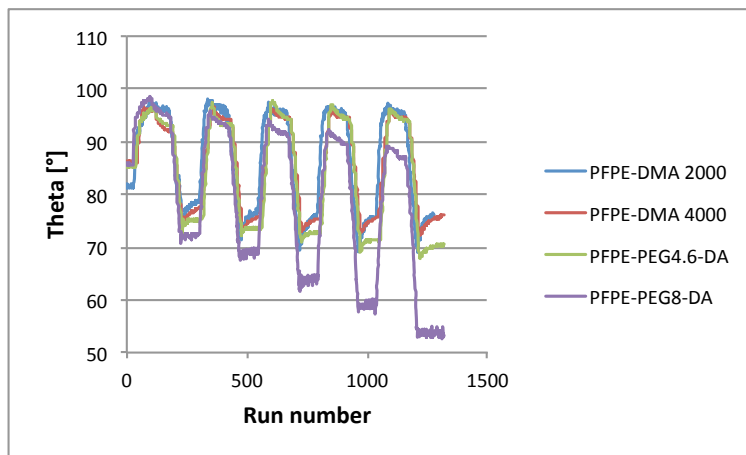


Figure 7. Dynamic contact angle measurements showing a thermodynamic hysteresis for all PFPEs-based materials and highlighting the kinetic hysteresis for PFPE-PEG8-DA substrates.

Comparing the trend of the two classes of PFPEs, a higher surface group rearrangement was observed for PFPE-PEG-DAs due to their higher polar contribution with respect to PFPE-DMAs. The higher molecular weight PFPE-PEG-DA shows the highest value of hysteresis likely due to the higher length of the PEG blocks and the lower density of cross-linking of the polymer network. Finally, experimental results suggest that the change in molecular weight of the lateral segments  $R_h$  has a stronger impact on surface properties than the molecular weight increase of the main perfluoropolyether chain.

### 6.3.3 Dynamic mechanical analysis

The conservative ( $G'$ ) and dissipative ( $G''$ ) components of the shear modulus of PFPEs studied were measured with DMA. DMA curves (Fig.8) were collected as a function of oscillation amplitude at constant frequency and temperature, which was kept at 65°C therefore well within the rubbery plateau of the material. In the rubbery state the  $G'$  value can be related to the cross-linking density of the polymer network, which could be estimated by applying the classical rubber elasticity theory<sup>27</sup>.

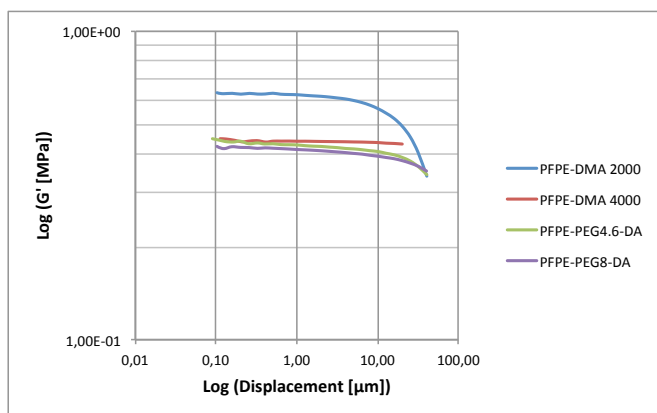


Figure 8. Dynamic shear moduli vs oscillation amplitude measured by Dynamic Mechanical Analysis performed at 70°C and 0.1 Hz.

Generally, PFPE-DMA's shear moduli resulted higher than PFPE-PEG-DAs values. Due to its shorter perfluoropolyether chain between methacrylic end chain groups, PFPE-DMA 2000 has a higher cross-link density with respect to PFPE-DMA 4000 thus a higher shear modulus. Similar considerations can be applied to explain the higher shear modulus of the PFPE-PEG4.6-DA with respect to the PFPE-PEG8-DA. Consequently, it is possible to assert that the molecular weight increase of the perfluoropolyether backbone mainly affect mechanical properties whereas changing the molecular weight of lateral segment has a stronger effect on surface properties (6.3.2).

### 6.3.4 Anti-fouling and fouling-release properties

#### 6.3.4.1 Protein adhesion resistance

Protein aspecific adsorption of fully cured PFPE-based materials was studied performing static and dynamic anti-fouling/fouling release experiments. Static anti-fouling properties and dynamic fouling release properties were evaluated by analyzing images of fluorescence intensities from both a qualitative (Fig.9 and Fig.11) and quantitative (Fig.10 and Fig.12) point of view.

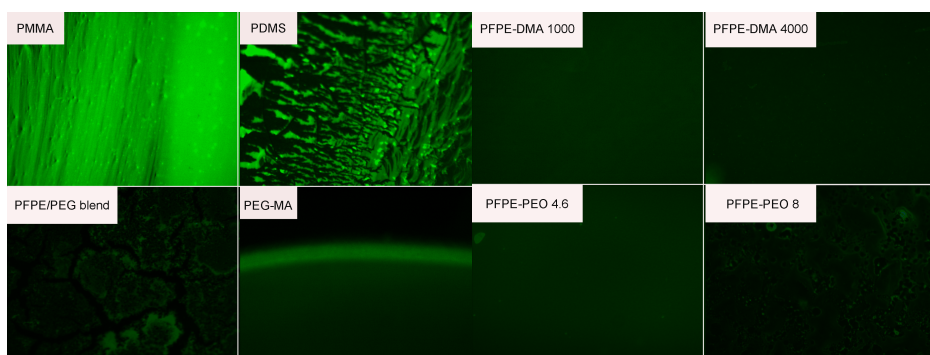


Figure 9. Images acquired by fluorescence microscopy after static tests.

Concerning static tests, the phenomenon of protein aspecific adsorption occurs clearly on PMMA and PDMS surfaces whose signal intensity is higher respect to other samples (Fig.9). On the contrary, fluorescence intensity on all PFPE-based polymers is comparable to the signal from PEG-MA, a well-established anti-fouling substrate. A quantitative comparative analysis allows for the rationalization of the results shown in Figure 10.

A quantification of total amount of adsorbed proteins was obtained comparing fluorescence intensity data. Particularly, image brightness is an indication of BSA-FITC adherence on the substrates and it was quantified as the mean tonal values of the images histograms (Fig.10), which were taken for all tested materials. The histograms represent the number of pixels for each tonal value on a scale having 255 tonalities. The results prove that a residual fluorescence is always present in all surfaces but all PFPE-based materials behave as PEG-MA with poor aspecific adhesion of BSA, phenomenon that instead is highly appreciable on PDMS and

PMMA.

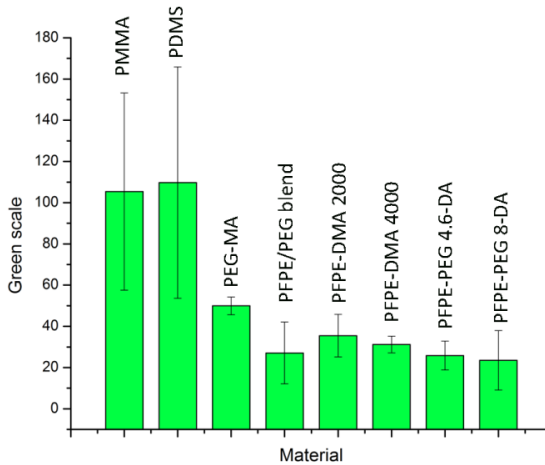


Figure 10. Mean tonal value obtained for each sample tested in static conditions allows for FITC-BSA specific adsorption quantification. PDMS and PMMA give the brightest images while PFPE-PEG 8-DA and PFPE/PEG blend the darkest

Moreover, PDMS and PMMA are both characterized by an appreciable standard deviation that reveals variability from sample to sample. The opposite behavior was observed for PFPEs materials.

Dynamic tests were even implemented to study the fouling release properties of the substrates. Consequent results (Fig.11 and Fig.12) show that at the end of the tests the residual fluorescence of all the substrates was significantly reduced with respect to static tests.

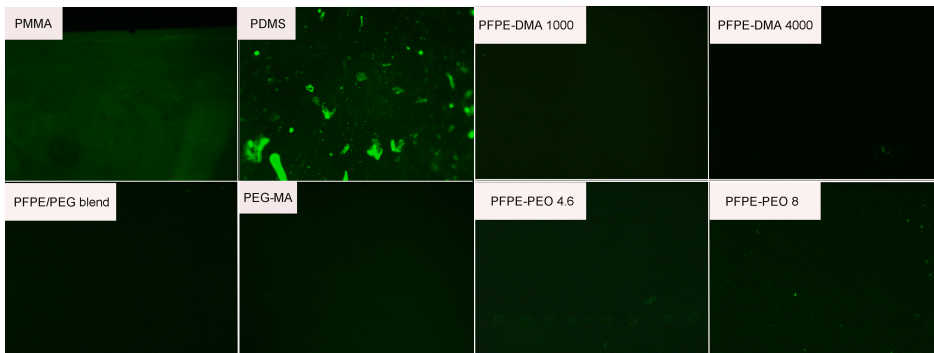


Figure 11. Fluorescence images acquired after dynamic tests.

BSA-FITC adhesion in dynamic conditions is better promoted onto PDMS and

PMMA substrates as for static conditions. All PFPE-based materials show similar brightness, comparable to PEG-MA. Among all, PFPE-DMA 4000 shows an important reduction in fluorescent signal thus meaning that hydrodynamic forces easily detached BSA-FITC from PFPE-DMA 4000, which results the best performing material for microfluidic applications. As for the static results, a quantitative analysis of protein aspecific adsorption was performed by calculating the mean tonal values from the image histograms.

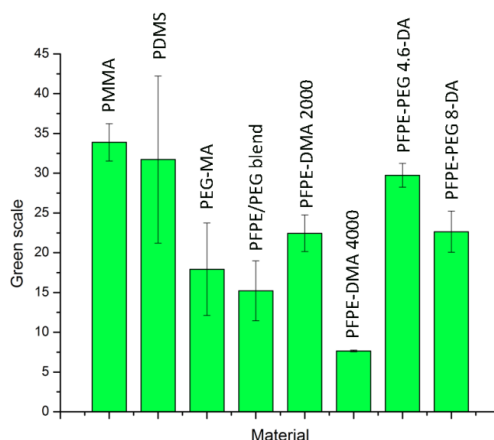


Figure 12. Mean tonal values deriving from dynamic conditions. Again, the brightest fluorescence was measured for PDMS and PMMA while PFPE-DMA 4000 resulted as the best candidate/best performing material for fluidic applications.

Results confirmed that PFPE-DMA 4000 could be classified as an efficient fouling-release substrate towards microorganism to be implemented for biomedical applications and not only in the marine context. Moreover, its very low standard deviation demonstrates its experimental reproducibility.

#### 6.3.4.2 Protein adhesion tests automatization

Protein adhesion tests were also performed exploiting a microcontact arrayer that presents some advantages including:

- Testing different proteins in close contact on the same substrate;
- Parallelization of test with different concentration of the same protein;

- Automatizing the printing, washing and drying steps thus reducing possible results variability derived from manual processes;
- Printing and incubating samples keeping constant conditions of humidity and temperature.

In the present work three different types of proteins at four different concentrations (0.002, 0.02, 0.2 and 2 mg/ml) were printed: Albumin from Bovine Serum (BSA), as in the previous case (6.3.4.1); Streptavidin (StreptAv), and Immunoglobuline G (IgG), which are proteins widely use in biomedical applications (e.g. molecular patterning, antibody recognition). Again, anti-fouling properties were evaluated by analyzing images of fluorescence intensities from both a qualitative and quantitative point of view and considering the image brightness as an indication of protein aspecific adhesion to the substrate. Figure 12, reported as a representative and meaningful example, shows that the phenomenon of protein aspecific adsorption occurs clearly on PMMA surfaces: in fact, image of fluorescent intensity after washing with water (Fig.13b) decreases only a little, compared with the image before washing (Fig.13a). On the contrary, fluorescence intensity after washing procedure is almost equal to zero on PFPE-DMA 4000 whose behavior was similar to all the other PFPE-based materials and comparable to PEG-MA substrate (images not shown).

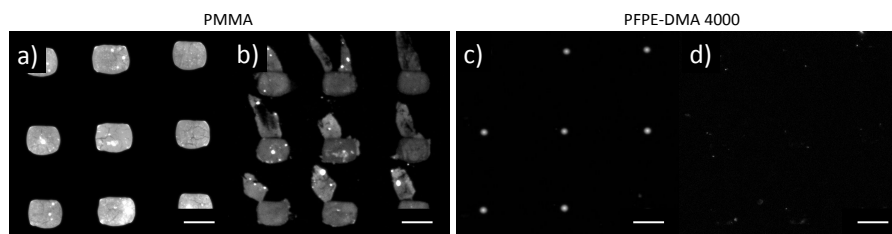


Figure 13. Examples of fluorescent arrays before washing (a and c) and after washing (b and d) obtained printing Streptavidin AF555 0.2 mg/ml onto PMMA and PFPE-DMA 4000 respectively. The scale bar is 100  $\mu\text{m}$ .

It is worthwhile noticing the appreciable difference in spot size obtained for the two substrates before washing (Fig.13b and 13c). While for PMMA, spot dimensions correspond to the 100- $\mu\text{m}$  nominal diameter of the layer sample spotted by the pin tip (6.2.5.2), for PFPE-DMA 4000 the spot is about tenfold reduced. Probably, the high hydrophobicity of the substrate prevents the total

deliver of the sample which proceeds by simple gentle surface contact without the use of a tapping force to expel. This trend was observed for all the protein solutions tested and consequently, following quantitative results will be presented just for the concentrations of 0.2 mg/ml which has been exploited most in the present work of thesis as explained later in the last chapter.

An estimate of total amount of adsorbed proteins was obtained comparing fluorescence intensity data acquired by the spots of the arrays deposited on the various substrates. The results for 0.2 mg/ml protein concentration, shown in Figure 14a, 14b, and 14c confirm that the phenomenon of aspecific adsorption is higher on PMMA substrates where as all PFPEs-based material show fluorescence brightness similar to PEGMA. In general, the highest values were obtained testing with IgG, whereas the poorest aspecific adhesion was observed for Streptavidin. This is crucial considering that the biotin-avidin system is one of the most used chemistry strategy for biomolecules selective immobilization onto surfaces. Finally, results confirmed PFPE-DMA 4000 and PFPE-DMA 2000 to be challenging material for the fabrication of anti-fouling and fouling release devices.

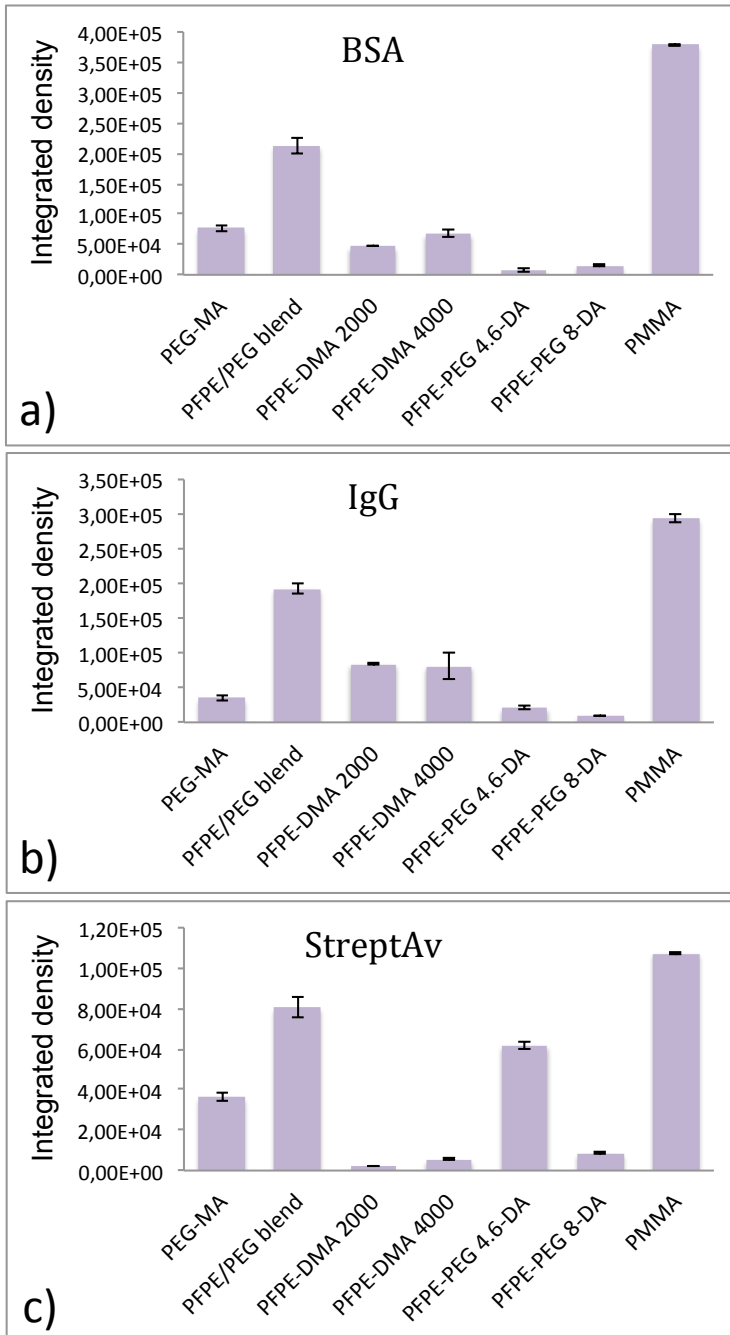


Figure 14. (a) BSA, (b) IgG, and (c) StreptAv Integrated density values measured for the printed arrayer after the washing and air-drying steps. Again, the brightest fluorescence was measured PMMA while PFPEs-based materials performed as PEG-MA, a well-known anti-fouling material.

### 6.3.4.3 Cell adhesion resistance

In order to verify the cells adhesion resistance of the PFPE-DMA 4000 surface, tests were performed seeding and incubating the substrates with human osteosarcoma cells. MG-63 adhesion was evaluated studying cells morphology through phase contrast and SEM images, acquired after two hours of incubation and after two days respectively. As shown in Figure 15, all cells presented a well-rounded morphology and not star-shaped with filaments and protrusions, which instead are typical of proliferating and well-adhered cells. Hence, the cells did not adhere on the substrate thus attesting the anti-fouling properties against cells of PFPE-DMA 4000.

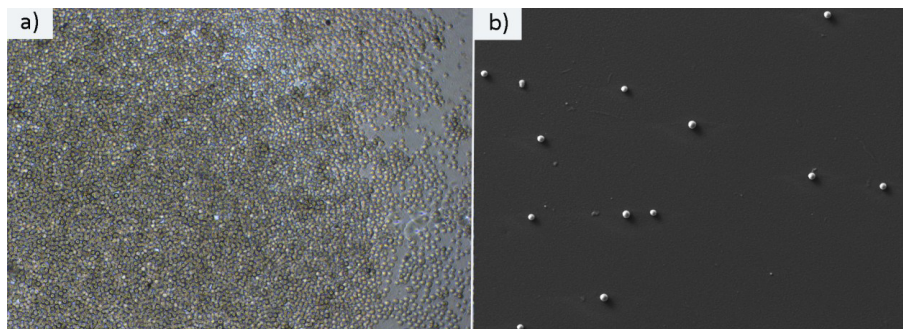


Figure 15. MG-63 cells seeded on a PFPE-DMA substrate and fixed with glutaraldehyde according to standard protocols. Phase contrast images acquired after two hours of cell culture (a) and SEM image acquired after two days (magnification 500x, I probe 50 pA, EHT 20 kV). All cells show a spherical morphology that is typical of not-adhering cells on the underlying substrate.

### 6.3.5 The role of surface and mechanical properties on fouling release properties

According to literature, fouling-release properties are correlated to both surface tension and elastic modulus, and particularly there could be a linear dependence of fouling release performance on  $(E\gamma)^{1/2}$ <sup>213,14</sup>. In order to verify the applicability of such relationship to the present study, PFPE fouling-release performance represented by the mean tonal value, was plotted against PFPE characterization results in terms of mechanical properties and surface energy. As shown in the graph reported in Figure 16a, it can be noticed that there is no a clear trend but some subgroups could be identified. Increasing  $(E\gamma)^{1/2}$  a worsening in the fouling-release performance can be noticed going from PFPE-DMA 4000 to PFPE/PEG blend and to PFPE-DMA 2000. The same behavior could be noticed for PFPE-PEG-DAs where PFPE-PEG8\_DA, having a lower  $(E\gamma)^{1/2}$ , was better performing with respect to PFPE-PEG4.6-DA. The deviation of PFPE-PEG-DAs from the first subgroup may be attributed to other phenomena such as the surface rearrangements revealed from dynamic contact angle measurements that may play a role favoring the hydrophilic groups on the surface. Thus the loss of the fluorine atoms sheath on the surface may lead to increased protein binding. Taking into account these rearrangement phenomena and the consequent effect of dynamic contact angle hysteresis, the contribution of polar and dispersive components was considered separately for elastomeric materials only. From the graph in Figure 16b, a general trend was observed just for PFPEs with lower value of  $(E_{\text{polar}})^{1/2}$  corresponding to better performances in terms of fouling-release properties. It is important to highlight that mechanical properties seem to give significant contribution to fouling-release properties at least within a well-defined class of polymeric materials. In fact, if we consider the two PFPE-DMAs, they have comparable surface energies, hence the most significant contribution for the difference in fouling release properties comes from differences in stiffness of the surface layer. A similar reasoning can be applied to PFPE-PEG-DAs. Since we have noticed that the PFPE backbone mainly influences mechanical properties, we can conclude that the molecular weight of the main PFPE chain

may significantly affect the fouling-release performances. However, if the same data fitting is applied to the whole set of experimental data including PMMA, PEG-MA and PDMS, the correlation is poor and no clear trend seems to exist (data not shown).

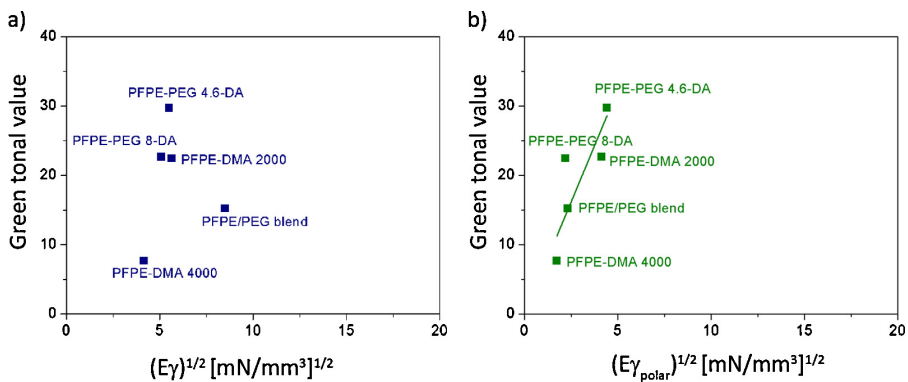


Figure 16. PFPEs fouling-release trend depending on both surface tension and mechanical properties (a) considering the total component of surface tension; (b) considering only the polar component of surface tension. In the second case a better correlation was found.

## 6.4 Conclusions and future perspectives

The development of new anti-fouling and fouling release materials has gained lots of attention in the biomedical field and is deeply encouraging the research on protein-resistant biomedical devices, on microfluidic devices applied to biochemistry and on biomolecular patterning. Indeed, the performance of the final substrates is mainly affected by their anti-fouling/fouling release characteristics towards proteins, cells and micro-organisms that are required to avoid non-specific binding phenomena on the substrate. In the present work, perfluoropolyethers (PFPEs) were chosen for their peculiar physico-chemical properties and were investigated as challenging materials for the biomedical applications mentioned. Particularly, photocurable PFPEs were obtained by modifying telechelic PFPE diols to create PFPE urethane methacrylic and PFPE-PEG acrylic polymers (PFPE-DMA and PFPE-PEG-DAs respectively). These were characterized in terms of surface and mechanical properties to study whether or not it is possible to establish a correlation between these properties and their final fouling-release performance. The study revealed that there is a linear dependence of such behavior on a parameter containing both surface energy and elastic modulus. The PFPE-DMA with high molecular weight was the best performing due to the low surface energy but, most important, to the low elastic modulus. However, low surface energy, high molecular weight of the PFPE chain between cross-link points and the absence of surface group rearrangement (kinetic hysteresis) seems to be important requirements for the design of anti-fouling/fouling release materials. Thus, all PFPEs could be considered suitable candidate and copolymerization of PFPEs with PEG to give linear segmented structures did not show any significant improvement suggesting that extremely low surface tension materials perform better than amphiphilics.

## 6.5 References

1. Chambers, L. D., Stokes, K. R., Walsh, F. C. & Wood, R. J. K. Modern approaches to marine antifouling coatings. *Surf. Coatings Technol.* **201**, 3642–3652 (2006).
2. Bajpai, A. K. Blood protein adsorption onto a polymeric biomaterial of polyethylene glycol and poly[(2-hydroxyethyl methacrylate)-co-acrylonitrile] and evaluation of in vitro blood compatibility. *Polym. Int.* **54**, 304–315 (2005).
3. Trombetta, T., Iengo, P. & Turri, S. Fluorinated segmented polyurethane anionomers for water–oil repellent surface treatments of cellulosic substrates. *J. Appl. Polym. Sci.* **98**, 1364–1372 (2005).
4. Turri, S., Radice, S., Canteri, R., Speranza, G. & Anderle, M. Surface study of perfluoropolyether–urethane cross-linked polymers. *Surf. Interface Anal.* **29**, 873–886 (2000).
5. Simeone, G., Turri, S., Scicchitano, M. & Tonelli, C. Fundamental properties of fluoropolyether-based resins and related coatings. *Die Angew. Makromol. Chemie* **236**, 111–127 (1996).
6. Hu, Z. *et al.* Photochemically Cross-Linked Perfluoropolyether-Based Elastomers: Synthesis, Physical Characterization, and Biofouling Evaluation. *Macromolecules* **42**, 6999–7007 (2009).
7. Yarbrough, J. C. *et al.* Contact Angle Analysis, Surface Dynamics, and Biofouling Characteristics of Cross-Linkable, Random Perfluoropolyether-Based Graft Terpolymers. *Macromolecules* **39**, 2521–2528 (2006).
8. Rolland, J. P., Van Dam, R. M., Schorzman, D. A., Quake, S. R. & DeSimone, J. M. Solvent-resistant photocurable liquid fluoropolymers for microfluidic device fabrication [corrected]. *J. Am. Chem. Soc.* **126**, 2322–3 (2004).
9. Wang, Y. *et al.* Photocurable Amphiphilic Perfluoropolyether/Poly(ethylene glycol) Networks for Fouling-Release Coatings. *Macromolecules* **44**, 878–885 (2011).
10. Kwon, S., Kim, H., Ha, J.-W. & Lee, S.-Y. Prevention of protein and polymeric nanoparticles adsorption using perfluoropolyether. *J. Ind. Eng. Chem.* **17**, 259–263 (2011).
11. Baier, R. E. The role of surface energy in thrombogenesis. *Bull. New York Acad. Med. J. Urban Heal.* **48**, 257–272 (1972).

12. Baier, R. E., Depalma, V. A., Goupil, D. W. & Cohen, E. Human platelet spreading on substrata of known surface chemistry. *J. Biomed. Mater. Res.* **19**, 1157–1167 (1985).
13. Magin, C. M., Cooper, S. P. & Brennan, A. B. Non-toxic antifouling strategies. *Mater. Today* **13**, 36–44 (2010).
14. Hu, Z. Novel Perfluoropolyethers as Fouling-Release Coatings. (University of North Carolina, 2009).
15. Brady, R. F. A fracture mechanical analysis of fouling release from nontoxic antifouling coatings. *Prog. Org. Coatings* **43**, 188–192 (2001).
16. Priola, A. *et al.* UV-curable systems containing perfluoropolyether structures: Synthesis and characterisation. *Macromol. Chem. Phys.* **198**, 1893–1907 (1997).
17. Kim, P. *et al.* Fabrication of nanostructures of polyethylene glycol for applications to protein adsorption and cell adhesion. *Nanotechnology* **16**, 2420 (2005).
18. Kendall, K. The adhesion and surface energy of elastic solids. *J. Phys. D. Appl. Phys.* **4**, 1186–1195 (1971).
19. Wu, S. Polar and Nonpolar Interactions in Adhesion. *J. Adhes.* **5**, 39–55 (1973).
20. Chumbimuni-Torres, K. Y. *et al.* Adsorption of Proteins to Thin-Films of PDMS and Its Effect on the Adhesion of Human Endothelial Cells. *RSC Adv.* **1**, 706–714 (2011).
21. Sharma, S., Johnson, R. W. & Desai, T. A. XPS and AFM analysis of antifouling PEG interfaces for microfabricated silicon biosensors. *Biosens. Bioelectron.* **20**, 227–39 (2004).
22. Turri, S., Levi, M., Emilriti, E., Suriano, R. & Bongiovanni, R. Direct Photopolymerisation of PEG-Methacrylate Oligomers for an Easy Prototyping of Microfluidic Structures. *Macromol. Chem. Phys.* **211**, 879–887 (2010).
23. Bongiovanni, R., Medici, A., Zompatori, A., Garavaglia, S. & Tonelli, C. Perfluoropolyether polymers by UV curing: design, synthesis and characterization. *Polym. Int.* **61**, 65–73 (2012).
24. Extrand, C. W. Contact Angles and Hysteresis on Surfaces with Chemically Heterogeneous Islands. *Langmuir* **19**, 3793–3796 (2003).
25. Rupp, F., Scheideler, L. & Geis-Gerstorfer, J. Effect of Heterogenic Surfaces on Contact Angle Hysteresis: Dynamic Contact Angle Analysis in Material Sciences. *Chem. Eng. Technol.* **25**, 877–882 (2002).

26. Chan, C.-M. Polymer surface modification and characterization. (1993).
27. Gedde, U. in *Polymer Physics SE - 3* 39–53 (Springer Netherlands, 1999).  
doi:10.1007/978-94-011-0543-9\_3

